Characterization of jets in Heavy Ion collisions using photons at the LHC with the CMS detector

by

Richard Alexander Barbieri

Submitted to the Department of Physics
in partial fulfillment of the requirements for the degree of

Doctor of Philosophy in Physics

at the

MASSACHUSETTS INSTITUTE OF TECHNOLOGY

February 2017

Author .....
Department of Physics
November 21, 2016

Certified by .....
Bolesław Wysłouch
Professor
Thesis Supervisor

Accepted by .....
Nergis Mavalvala
Associate Department Head of Physics

Characterization of jets in Heavy Ion collisions using photons at the LHC with the CMS detector

by

Richard Alexander Barbieri

Submitted to the Department of Physics
on November 21, 2016, in partial fulfillment of the
requirements for the degree of
Doctor of Philosophy in Physics

Abstract

Using the CMS detector at the LHC, a quantitative study of jet energy loss and angular deflection inside the high energy-density medium formed in PbPb collisions is made. Photons are used to measure the initial state of a color-charged probe while jet reconstruction is used to measure the final state. Significant loss of energy to the medium as a function of initial parton momentum is observed, while no significant angular deflection is found.

Thesis Supervisor: Bolesław Wysłouch
Title: Professor

Acknowledgments

This thesis is dedicated to my fellow graduate students:

- Ian Chen
- William Koch
- Hai Chen
- Wei Sun
- Matthew Krafczyk
- Dragos Velicanu
- Doga Gulhan
- Siarhei Vaurynovich
- Yetkin Yilmaz
- Frank Ma
- Yongsun Kim
- Andre Yoon
- Mukund Madhav Varma
- Aleksey Strelnikov
- Ta-Wei Wang
- Jing Wang
- Chris McGinn
- Austin Baty
- Kaya Tatar
- Bi Ran

These are a group of people that I consider myself extremely fortunate to have worked, lived, and grown up with. Graduate school is a very strange institution, a mixture of a first job and final formal education. The people you share that experience with have the potential to make it excruciating or fantastic, and I was lucky enough to have the latter. Long hours spent in the lab, night shifts gathering data, tiny apartments crammed with 5 people, fixing insane programming bugs, attempting to perform analyses, and those rare fleeting moments of catharsis discussing physics were

all made enjoyable by the people I could share them with.

I sincerely hope that I can find another group as driven, empathetic, and brilliant as the one which I found at MIT.

Preface

This thesis is based on data: recorded by the CMS detector which was built by thousands of engineers, reconstructed using software written by thousands of developers, analyzed using techniques developed in consultation with thousands of scientists, and reviewed by hundreds of publication committee members. While this analysis would not have been completed at this time without my involvement, neither would it have been completed without the work of countless others.

The material of this thesis is based in majority on CMS Public Analysis Summary (PAS) HIN-16-002 [1] for which I was the primary analyzer and contact person within the collaboration. Chapter 2 is based on public information about the CMS detector contained in Reference [2, 3]. Chapters 3, 4, and 5 are prepared directly from the analysis materials attached to HIN-16-002, unpublished but available for CMS members in Reference [4]. Chapter 6 is taken verbatim from the PAS.

I am especially proud of my involvement with the L1 triggering system (Section 2.2.1), the noise reduction (Section 5.1.1), the purity determination (Section 5.1.4), and the design of the analysis software itself, all of which I feel particularly responsible for.

Please keep in mind the enormous amount of collective labor that went into this thesis (and all CMS theses) as you review it.

Contents

Chapter 1

Introduction

Quantum Chromo-Dynamics (QCD) [5, 6, 7] is the theoretical description of the strong nuclear force. This force governs the interactions of quarks and gluons, the building blocks of the nucleus of atoms. The strong force binds quarks and gluons together within protons and neutrons and also holds those protons and neutrons together in the nucleus. In the first microsecond after the big bang, the energy density was high enough that quarks and gluons did not form these baryonic bound states, instead existing as a soup of "free" color charges governed entirely by strong interactions. The strong force was responsible for any structure formation in this stage of the universe's development.

We would like to be able to predict the behavior of these systems in order to understand both the primordial and modern universe. QCD is a complete description of the strong force, but compared to Quantum Electro-Dynamics (QED) [8, 9], where observables are calculable with perturbation methods to near-infinite precision, there are QCD regimes where perturbative methods break down as the QCD coupling constant α_s is large. The effective strong coupling α_s 'runs' with the interaction energy. In simplified terms, at long distances or low energies the energy required to separate two color charges becomes infinite, so new particles are pulled from the vacuum in order to screen any bare color charges, a phenomenon referred to as Confinement [5]. At short distances or high energies α_s is small, allowing perturbation theory solutions as expansions of α_s. This is referred to as Asymptotic Freedom [6, 7].

Even with a well defined Lagrangian, the emergent behavior of systems governed by QCD is difficult to predict. While lattice QCD calculations have been very successful for systems at low baryon chemical potential (for example, calculating the hadron mass spectrum), systems at high baryon chemical potential become numerically intractable [10]. For real-time phenomena, such as the jet quenching studied in this thesis, it is not possible to formulate dynamical processes on the lattice [11]. Therefore there is significant value in investigating these difficult to predict and intractable regimes experimentally and creating phenomenological models to describe their behavior.

One system where we have control over the initial conditions and are able to measure the system after strong interactions is heavy ion collisions. Two nuclei are collided at high energy and some interaction governed by the strong force occurs. Detectors placed around the collision site capture the outgoing products of the interaction and we are able to infer details about the interaction from them. The beam energy, nuclei species, impact parameter, and species and momentum of collision products can all be varied independently to study the interactions.

1.1 Heavy Ion Physics: The Quark Gluon Plasma

Initial expectations for heavy ion collisions were that the energy densities were well within the Asymptotic Freedom regime, with α_s small enough that the free quarks and gluons were essentially non-interacting and a kinetic gas state, termed the Quark-Gluon Plasma (QGP), would be formed. However, the first experiments at the Relativistic Heavy Ion Collider (RHIC) showed significant evidence of hydrodynamic flow[12], which suggested that the state of matter is strongly interacting and possibly equilibrated. The nature of these strong interactions is the primary focus of research in the field currently.

Several techniques were developed to study the QGP. One uses a direct probe of the QGP, similar to Rutherford's seminal experiment. Is the probe deflected, indicating hard-core scattering centers? Does the probe lose energy in the interaction,

and how much? Unfortunately the QGP only lasts $\sim 10^{-23}$ s, not long enough to fire external probes through it, but nature has provided a convenient alternative – high energy particles created by hard parton-parton interactions within the collisions themselves travel through and interact with the medium. These high energy particles are formed before the medium, allowing us to measure their energy and direction after the interaction with the medium.

It is important to measure both the "before" and "after" pictures of any interaction, so in addition to the probe there must be some measurement of the initial conditions. Because the QGP is made up of color charges it interacts strongly with quarks, gluons, or any other color-charged matter. Leptons, photons, or Zs do not have any color charge, so they pass through the medium without interacting strongly. (The mean free path of electromagnetic interactions is much longer than the size of the medium, so no electromagnetic interactions are likely to occur.) This means that hard scattering processes which produce balanced pairs of a colorless particle with color-charged probe offer an ideal opportunity to study the medium. In particular, photons paired with a quark or gluon can be produced (see Fig. 1-1).

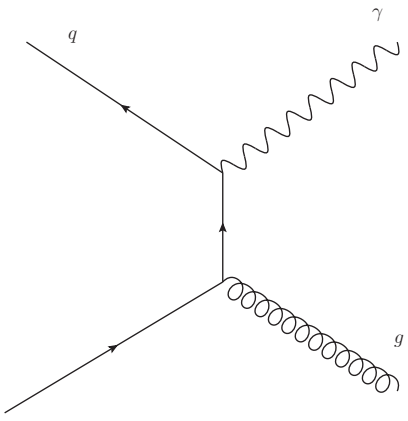

Figure 1-1: (Left to Right) A Photon-gluon pair produced from quark annihilation. (Bottom to Top) A Photon-quark pair produced by quark-gluon scattering.

1.2 Analysis Definitions

In order to perform an analysis using electroweak probes, a definition of the probe which is sensible both theoretically and experimentally must be constructed. From a theoretical point of view, it would be ideal if the experimentalist could use only prompt photons, known to come directly from a parton-parton hard scattering, and pair those directly with the colored parton. However, for both cases of the photon and colored parton these objects are experimentally identifiable.

In the case of the colored parton, color-charged objects cannot freely propagate and must instead form colorless bound states. The process of a hard parton transitioning to a colorless state by pulling particles out of the vacuum is called fragmentation, and results in the formation of correlated spray of particles called a jet. Just as with the photon, the definition of a jet must be sensible to both experimentalists and theorists. For this analysis and most others, the anti-k_T algorithm [13], which clusters high energy objects first and results in jets with a generally conic shape is used. For specific details on the jet definition see Section 3.3.

In the case of the photon, there are high p_{T} photons present from many sources, the most important of which are prompt production, fragmentation of jets, and neutral meson decay. Since it is not possible to determine the source of the photons experimentally, we use the requirement that the detected photon must be **isolated**, meaning that there is not a significant amount of energy surrounding the photon. This requirement increases the probability that the detected photon comes from prompt production, rather than fragmentation or decay. Care must be taken to make sure that the definition of isolation is at least well-correlated between the experimentally reconstructed value and the theoretically calculated one. The specifics of the isolation definition used for this analysis is in Section 3.1.4.

1.3 Status of Experiment

1.3.1 RHIC

The first results from RHIC immediately showed that the matter produced in heavy ion collisions had unexpected qualities. STAR showed that there was significant asymmetry in events that could be attributable to pressure-driven hydrodynamic flow [14]. PHOBOS showed that the number of particles produced in the collisions was lower than expected [15], an unexpected result eventually attributed to gluon saturation [16]. Continued measurements at RHIC over its lifetime have supported the hypothesis of hydrodynamic evolution in heavy ion collisions.

Measurements at RHIC of partons are usually done with hard hadron spectra. Leading hadrons in the event are measured as proxies of the initial parton. Significant energy loss of hadrons opposing a hard probe was observed [12], again suggesting the formation of a strongly interacting new phase of matter which could cause energy loss. The PHENIX collaboration measured photon-hadron azimuthal correlations and integrated yields [17], similar levels of suppression in photon-triggered events as inclusive hadron measurements (See Fig. 1-2.

Several attempts at fully reconstructing jets at RHIC have been undertaken at STAR, but the lack of a hadronic calorimeter makes triggering very difficult. The triggering method used relies on a single high p_{T} track which biases the reconstructed jets to have a harder fragmentation pattern. Nevertheless, this intentionally biased sample is useful for studying the QGP [18, 19]. Their latest results show that no energy loss of (biased) jets occurs for wide-enough jet radii.

The physics program of RHIC now concentrates on searching for signs of a phase transition to the Quark Gluon Plasma using a Beam Energy Scan [20], although no "smoking gun" results have yet been found. Tentative hints in the results have motivated a second Beam Energy Scan with upgraded detectors. The planned sPHENIX detector [21], which includes hermetic hadronic and electromagnetic calorimeter coverage for jet reconstruction, will also allow the physics program at RHIC to include full jet reconstruction.

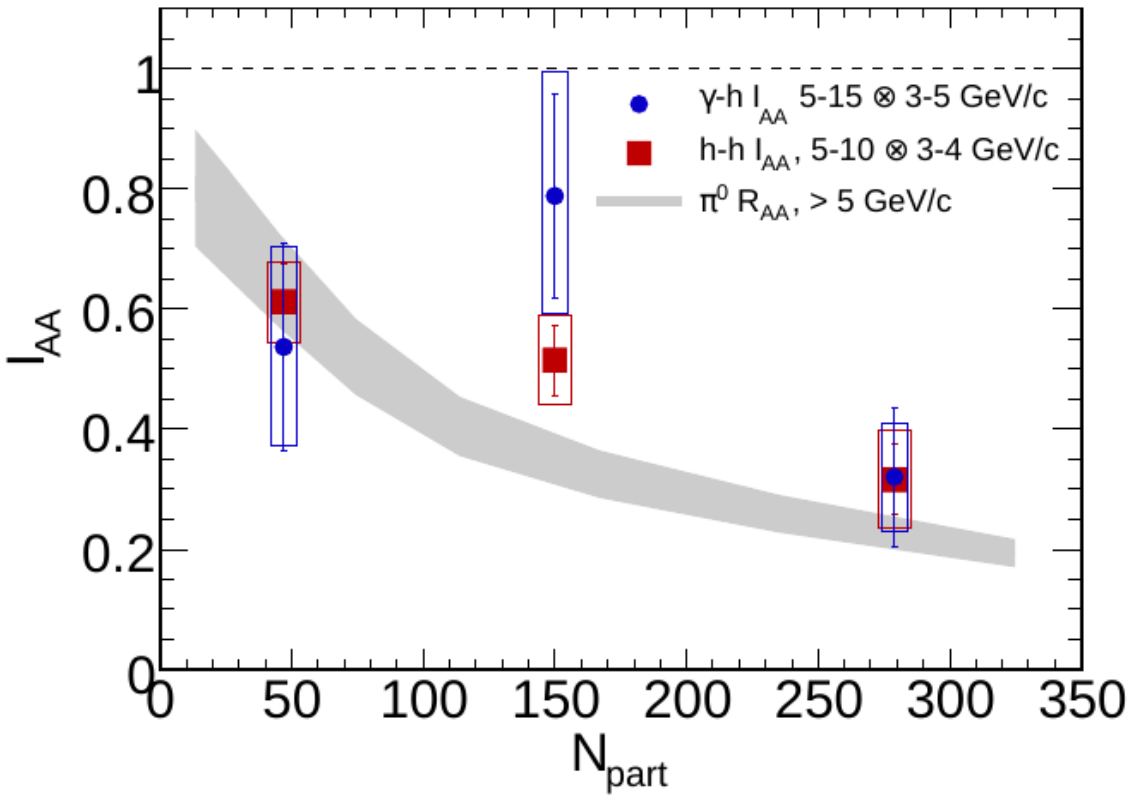

Figure 1-2: The ratio of yields in Au+Au to p+p collisions as measured with PHENIX, showing that the yields of away-side hadrons in photon-triggered events show a similar level of suppression as inclusive hadron measurements.

1.3.2 LHC

From the hadron measurements at RHIC, there were some expectations that the energy lost from away-side hadrons would be completely recovered within a reasonably-sized jet cone. It is difficult to conserve the transverse momentum of events if there is a high p_{T} parton on one side while the leading hadrons on the away-side have all lost energy without that energy remaining inside the cone. However, the first result of the LHC Heavy Ions program, from ATLAS and very soon corroborated by CMS, was that fully reconstructed jets really did show significant loss of jet energy, through dijet asymmetry measurements [22, 23].

These results meant that the energy of partons must be transferred from the hard parton to large angles, far away from the initial parton direction in order to escape the jet cone. However, without an unbiased probe the initial direction of both partons was not known and it could be conceivable that both were strongly affected. Even ignoring possible energy loss, the underlying event of heavy ion collisions could also bias the measurement by fluctuations [24]. Despite the reduced statistics, an electroweak probe and jet measurement would be necessary to confirm the dijet results.

As a first measurement, to guarantee that the electroweak probes are truly unbiased and there is no unexpected physics interacting with photons, an inclusive measurement of the isolated photon spectra was done [25]. This study found that the nuclear modification factor (the ratio of the spectra in PbPb collisions to the spectra in pp reference) was indeed consistent with 1, as expected if no modification of the electroweak probes occur.

Knowing that some form of jet quenching occurs in dijet systems and that isolated photons are an unbiased probe, an initial measurement of the energy loss of jets on the away-side of high p_{T} isolated photons was done using the data collected by CMS in 2011 [26]. This study showed that jets lose energy without significant angular deflection from the photon when compared to a Monte-Carlo reference, and a followup study with better pp statistics showed that the conclusions held when compared to pp and pPb datasets [27].

Results from pPb collisions can be used as a reference to PbPb collisions which is not expected to include QGP effects but will include so-called cold nuclear matter effects related to interactions with the nucleons themselves. CMS results showed that there is no energy loss observed for jets [28] and no energy loss observed for charged particles [29] in pPb collisions. These results show that any cold nuclear matter effects are not the cause of the strong energy loss observed in PbPb collisions.

The PbPb collisions recorded in November and December of 2015 had about a factor of 5 more high p_{T} isolated photons compared to the 2011 dataset (due to increased recorded luminosity and higher production cross section at the higher energy collisions). This higher statistics dataset is the basis of this thesis, and opened up the possibility of more differential measurements as a function of impact parameter and photon p_{T}.

Chapter 2

The Compact Muon Solenoid at the Large Hadron Collider

The Compact Muon Solenoid (CMS) is located at Point 5 on the ring of the Large Hadron Collider (LHC) near Geneva, Switzerland. The LHC ring straddles the border of France and Switzerland and is a part of the European Organization for Nuclear Research (CERN). The LHC inhabits the same tunnel as the Large Electron-Positron Collider (LEP), which operated from 1989 until 2000. The LHC began stable operation in 2009.

CMS is one of two general-purpose detectors located at the LHC, the other being ATLAS. In addition, there are 2 special-purpose detectors, LHCb for B-physics, and ALICE for Heavy Ion physics. The LHC collides protons with protons for the majority of the running time, but roughly one month of every year is devoted to heavy ion collisions. The CMS Heavy Ion collaboration builds on the strong foundation of the general purpose detector and reconstruction algorithms used for pp and adapts them for use in pPb and PbPb collisions.

2.1 Detector Components

The CMS detector is composed of several sub-detectors. Starting at the interaction point and moving outward, there are the tracker, the Electro-Magnetic Calorimeter

(ECAL), the Hadronic Calorimeter (HCAL), the superconducting magnet providing a field of 3.8 Tesla, and the Muon Chambers.

2.1.1 Tracker

The inner track is divided into pixel detectors close to the beamline and strip detectors slightly further from the beamline. In total, the tracker covers $|\eta| < 2.4$. The pixel tracker is composed of three layers of silicon in the barrel located at 4, 7, and 11 cm from the beamline, and 2 layers in the endcaps. The pixel size is 100×150 μm. The pixel detector has a position resolution of 10 μm in the r and ϕ coordinates and 20 μm in the z coordinate.

The silicon strip detector has different widths and lengths to attempt to keep the occupancy at roughly 1% at low pile-up. In general the position resolution of the strip detectors is better than 50 μm in all three coordinates. In total there are 15400 strip modules which are read out.

The speed of the readout of the inner tracker is slow compared to the rest of the detector due to the huge number of individual pixels and strips, not to mention the time required to run an actual tracking algorithm. Therefore, the tracker is not available for L1 triggering.

The tracker is used in this analysis to identify electrons in order to reject them from the photon sample, to calculate the tracking isolation around the photon candidates, and as a component of the jet reconstruction.

2.1.2 Electro-Magnetic Calorimeter

The CMS ECAL is a homogeneous, hermetic arrangement of Lead-Tungstate ($PbWO_4$) crystals. In the barrel section, $|\eta| < 1.479$, there are 61200 crystals arranged in a projective fashion, pointing toward the nominal interaction point. Each crystal has a coverage of 0.0174 in $\Delta\phi$ and $\Delta\eta$, and has a depth of 23 cm, nearly 26 radiation lengths.

In the endcaps, $1.479 < |\eta| < 3.0$, there are 7324 crystals on each side arranged

in an $x - y$ grid. Each crystal has a depth of 22 cm, or nearly 25 radiation lengths. There is a preshower device placed in front of the endcap sections which is roughly 2.5 radiation lengths of lead followed by silicon strip detectors.

In both the barrel and endcap, crystals are grouped together in 5x5 units, called "towers" in the triggering system. During photon and electron reconstruction, the width of the shower is found using the distribution of energy within these towers (see Section 3.1.3.

During triggering, the readout of the ECAL is fast enough to be used for L1 triggers.

This analysis uses the Electro-Magnetic calorimeter for photon and electron reconstruction, calculation of electro-magnetic isolation around the photon candidates, and as a component of jet reconstruction.

2.1.3 Hadronic Calorimeter

The HCAL is composed of the Hadron Barrel (HB) detector, the Hadron Outer (HO) detector, the Hadron Endcap (HE) detector, and Hadron Forward (HF) detector. The HB is composed of brass absorber material with interspersed plastic scintillator, covering $|\eta| < 1.4$. The scintillator readout is arranged in towers of $\Delta\eta \times \Delta\phi = 0.087 \times 0.087$, totalling 2304 towers.

The HO detector lies in the central region outside the magnet, increasing the effective thickness of the HCAL to 10 nuclear interaction lengths within its coverage of $|\eta| < 1.26$. The HE uses the same construction as the HB but has larger segmentation. 14 towers in η cover $1.3 < |\eta| < 3.0$. There are coincidentally 2304 total towers in the HE.

The HF detector is made of steel absorber with scintillating fibers. It covers $3.0 < |\eta| < 5.0$ and is physically located about 11.2 m from the nominal interaction point, far forward. The Heavy Ions physics program makes heavy use of the HF to determine the centrality (impact parameter) of events.

The readout of the HCAL is fast enough to be used for L1 triggers.

This analysis uses the Hadronic Calorimeters to calculate the hadronic isolation

around photon candidates and as a component of jet reconstruction.

2.1.4 Muon Chambers

Sitting outside the magnet and surrounding the magnet return yoke is the Muon system, composed of drift tubes in the barrel region ($\eta < 1.2$), cathode strip chambers (CSC) in the endcap region ($1 < \eta < 2.4$), and resistive plate chambers (RPC) acting as a complementary detector across a large η range ($\eta < 2.1$). Because of the speed of the readout of these detectors compared to the inner tracker, they can be used for Level-1 triggering.

2.2 Triggering

Triggering is the art of deciding which events are worth recording. In 2015, the LHC had an interaction rate of roughly 15kHz for PbPb collisions, meaning that each second CMS must decide to either write to disk or ignore 15,000 events. If interesting events are not chosen properly they are lost to analyzers permanently. If triggers are not strict enough then the data acquisition or data storage abilities of the experiment could be overwhelmed. The trigger system is tuned to maximize the amount of signal and minimize the amount of noise within the bandwidth constraints of the data acquisition and retention systems.

On average, CMS saves only a small fraction of the collisions occurring in the detector. This is achieved using a two-tiered triggering system. The first layer of trigger system (Level 1 or L1) uses coarse information from the calorimeters and muon chambers only, without waiting for the (relatively) long readout and tracking algorithm times of the tracker. If the event passes one of the defined L1 triggers, it is passed to the High Level Trigger (HLT) where full offline-like reconstruction is performed and complete detector information is available. If the event passes any of the HLT triggers it is saved to disk for future analysis. Otherwise, it is discarded forever.

For PbPb collisions, the underlying event (equivalent to 150 pileup from a single

vertex) adds additional complications to the triggering method. Triggering on simple energy sums will be directly affected by the centrality of the events, leading to a very non-flat centrality distribution of recorded events. Tracking algorithms also take significantly longer for more central events, approaching the limits of the HLT system and necessitating special tuning.

2.2.1 Level-1 Trigger (L1)

For the Heavy-ion related datasets recorded in 2015, the Stage-1 Level-1 trigger was used[30]. The Stage-1 Level-1 trigger was a partial replacement of the legacy Level-1 trigger used during Run 1 of the LHC at CMS, where the application-specific integrated circuit (ASIC) boards in the old Global Calorimeter Trigger (GCT) were replaced with a field-programmable gate array (FPGA) board called an MP7 and referred to as "Layer-2" of the L1. The other components of the L1 trigger (the Regional Calorimeter Trigger (RCT) and Global Trigger (GT)) remained the same as the legacy trigger system from run 1 except for the addition of optical readout boards. See Figure 2-1 for a schematic of the L1 hardware.

The older ASIC boards limited the flexibility of the triggering systems since the algorithm had to be set during the design of the actual hardware for the boards. Once the boards were in place, the algorithm could not be changed. Thus, the proton-proton collisions and Pb-Pb collisions during run 1 used the same algorithms for triggering. With the replacement of the ASIC boards with an FPGA, the firmware (defining the algorithms) could be changed on the boards quickly, in between LHC fills or CMS runs, allowing separately tuned algorithms for proton-proton and Pb-Pb collisions to be used.

The primary motivation for the Stage-1 upgrade of the Level-1 detector was the limited performance of the legacy system for jet identification in Pb-Pb collisions. See Figure 2-2 for a plot which shows that the rejection power of the trigger was heavily centrality dependent and rejected almost no events with centrality $< 50\%$. For the interaction rates predicted before the 2015 run, this would have meant that the majority of events passed to the HLT from the L1 would have been noise and the

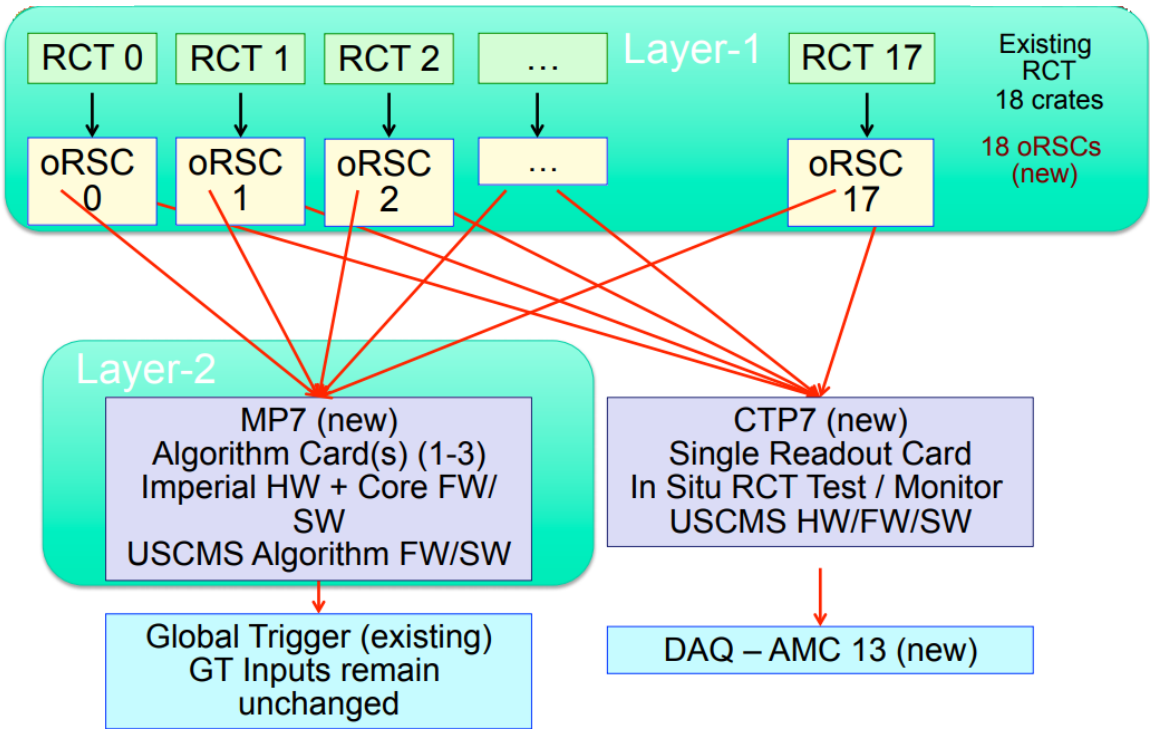

Figure 2-1: Schematic of the Stage-1 Level-1 trigger hardware. 18 RCT cards are piped through new oRSC readout electronics which split the signal between the MP7 FPGA, which handles the algorithm application, and the CTP7 FPGA, which handles extra readout. The MP7 FPGA runs the optimized L1 Calorimeter algorithms before passing the objects to the legacy GT which then makes the final L1 decision using the calorimeter and muon objects.

necessary threshold necessary to keep within the L1-HLT bandwidth limit (roughly 3kHz) would have resulted in a significant statistics reduction compared to a more performant L1, limiting several planned dijet analyses[30].

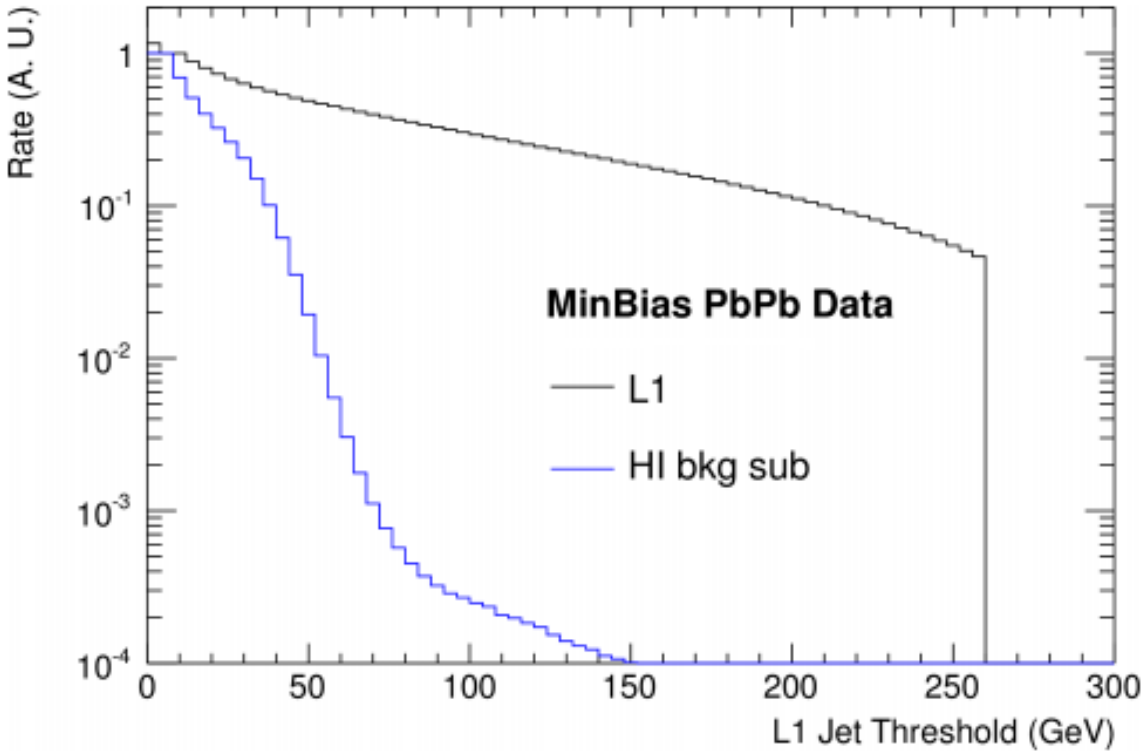

Figure 2-2: Comparison of the legacy (labeled "L1") and Stage-1 (labeled "HI bkg sub") algorithm performance. Using 2011 PbPb data, the rate of the legacy trigger is seen to not respond to changes in the trigger threshold. The Stage-1 algorithm uses background subtraction and is able to reduce the rate considerably at the same threshold value.

The Stage-1 L1 calorimeter trigger performs the following steps:

1. The ECAL and HCAL tower information is processed by the RCT.

    - The ECAL consists of 4032 towers in the barrel and endcap, 56 towers in η vs. 72 in ϕ. 18 "wheel" boards receive subsets of the detector 28 towers wide in η vs. 8 in ϕ.
    - The HCAL consists of the same 4032 towers with the addition of the HF on either side.

- Each wheel card computes the 4 most energetic 2x1 ECAL tower groupings which are "isolated" and the 4 which are "non-isolated". These are referred to as "EM-candidates".
- The wheel cards sum together the HCAL and ECAL towers in the barrel and endcap into 4x4 units called regions. Each wheel card produces 22 regions, for a total of 396 over the full calorimeter coverage.
- The EM-candidates and regions are sent to the Layer-2

2. Background subtraction is performed on the regions for Pb-Pb collisions, but not for proton-proton collisions.
   - The Layer-2 loops over each ϕ-ring (constant η value) set of 18 regions and finds the average energy value in that ring. This value is subtracted from each region in that ring.
3. The background-subtracted regions are grouped into jets.
   - Each local maxima region is a "jet seed".
   - For PbPb, the highest-energy 2x2 contiguous set of regions which contain each jet seed is a jet.
   - for pp, the 3x3 energy sum with each jet seed at the center is a jet.
   - For PbPb-collisions, the ϕ-rings corresponding to the last endcap region are excluded from the jets due to high amounts of noise. See Figure 2-3 for an explanation.
4. The 4 most energetic jets from the barrel+endcap and the 4 most energetic jets from the HF are sent to the Global Trigger.
5. The 8 most energetic EM-candidates are sent to the Global Trigger.
6. The GT makes a decision on the event using information from the Layer-2 and the Global Muon Trigger based on the Level-1 trigger menu in use. The menu

defines exactly 128 triggers which are combinations of EM-candidate, jet, tau, and muon information.

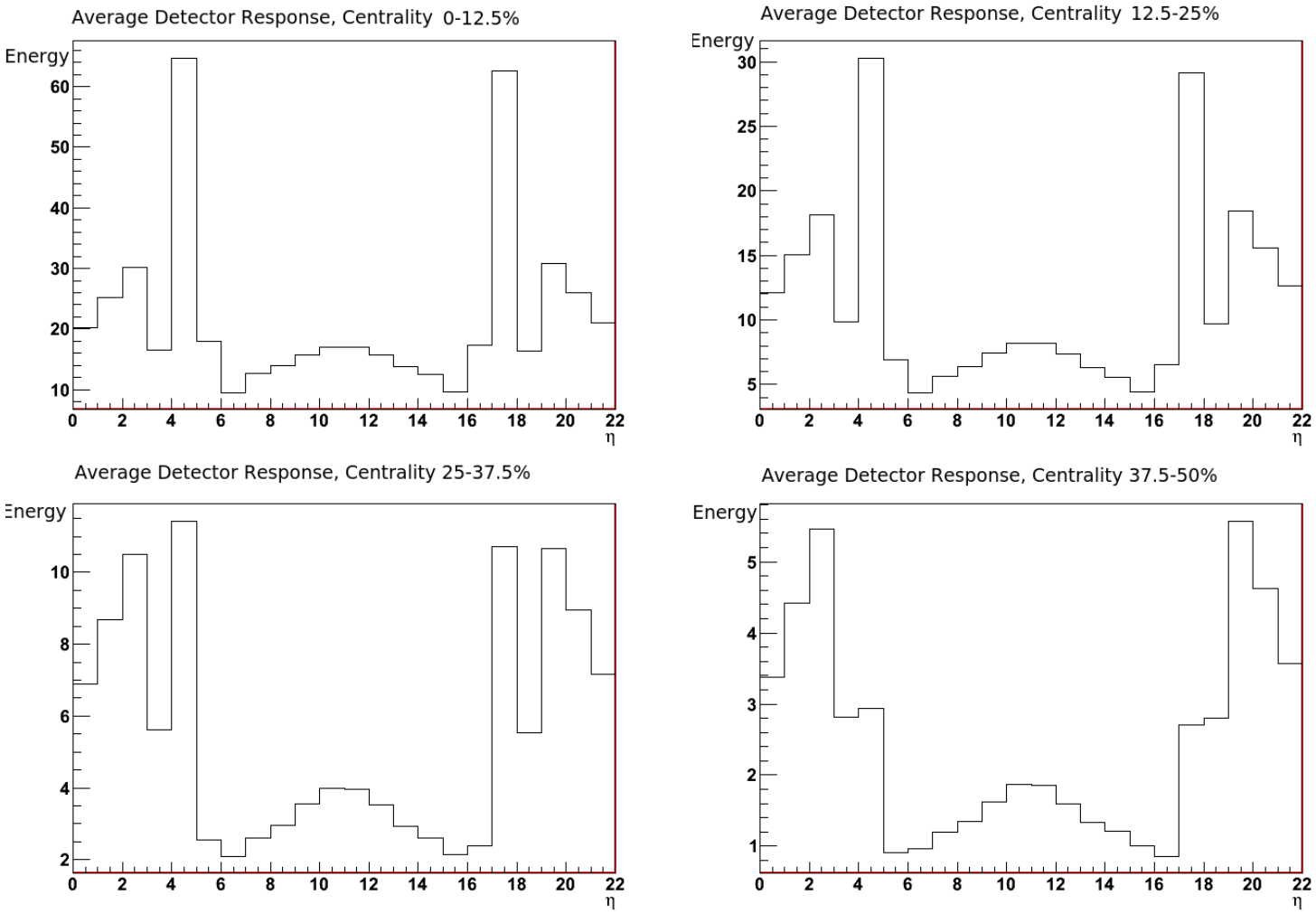

Figure 2-3: The x-axis of these plots is the hardware η value, running from 0 in the forward calorimeter on one side to 21 in the forward calorimeter on the other side. The y-axis is the average energy recorded in L1 regions at that position. In very central events, many soft particles which do not have the energy to reach the barrel tracker are swept by CMS's strong magnetic field into the endcaps. This causes a strong non-linear energy response in the final set of regions of the endcap ($\eta = 4$ and $\eta = 17$ in the figures). During the run, these regions were "masked" and not used for triggering.

The Stage-1 L1 Calorimeter firmware was first tested extensively in a Monte-Carlo simulation as part of the official CMSSW simulation and reconstruction software. Afterwards the algorithms were translated to VHDL and compiled to FGPA firmware, which was then tested on the board using fake inputs.

While the pp firmware was in active use during real collisions, the RCT information was duplicated and sent to a second MP7 board running PbPb firmware for further testing. The FPGA results were validated bitwise against the Monte-Carlo simulation over more than 10 million events, reaching perfect agreement before the PbPb data taking even began.

2.2.2 High-Level Trigger (HLT)

During the design of CMS (in the early '90s), there was a significant bet made on the advancement of consumer-grade computation. The HLT was designed not as a set of purpose-built chips to handle reconstruction and triggering, but rather as a general-purpose computation farm. The HLT is cluster of consumer-grade computing nodes all running identical reconstruction software.

In general, the HLT runs a version of the reconstruction software that is slightly optimized for speed, usually differing from the complete reconstruction only in small details like final calibrations and accuracy of the tracking algorithms. Once the reconstruction on the event has been run, arbitrarily complicated trigger decisions are made based on the collections of particles or energy sums identified in the event. For the particular analysis discussed in this thesis, a photon trigger requiring a reconstructed photon with momentum larger than 40 GeV/c was used. The efficiency of that trigger in the datasets used for this thesis can be found in Figure 2-4.

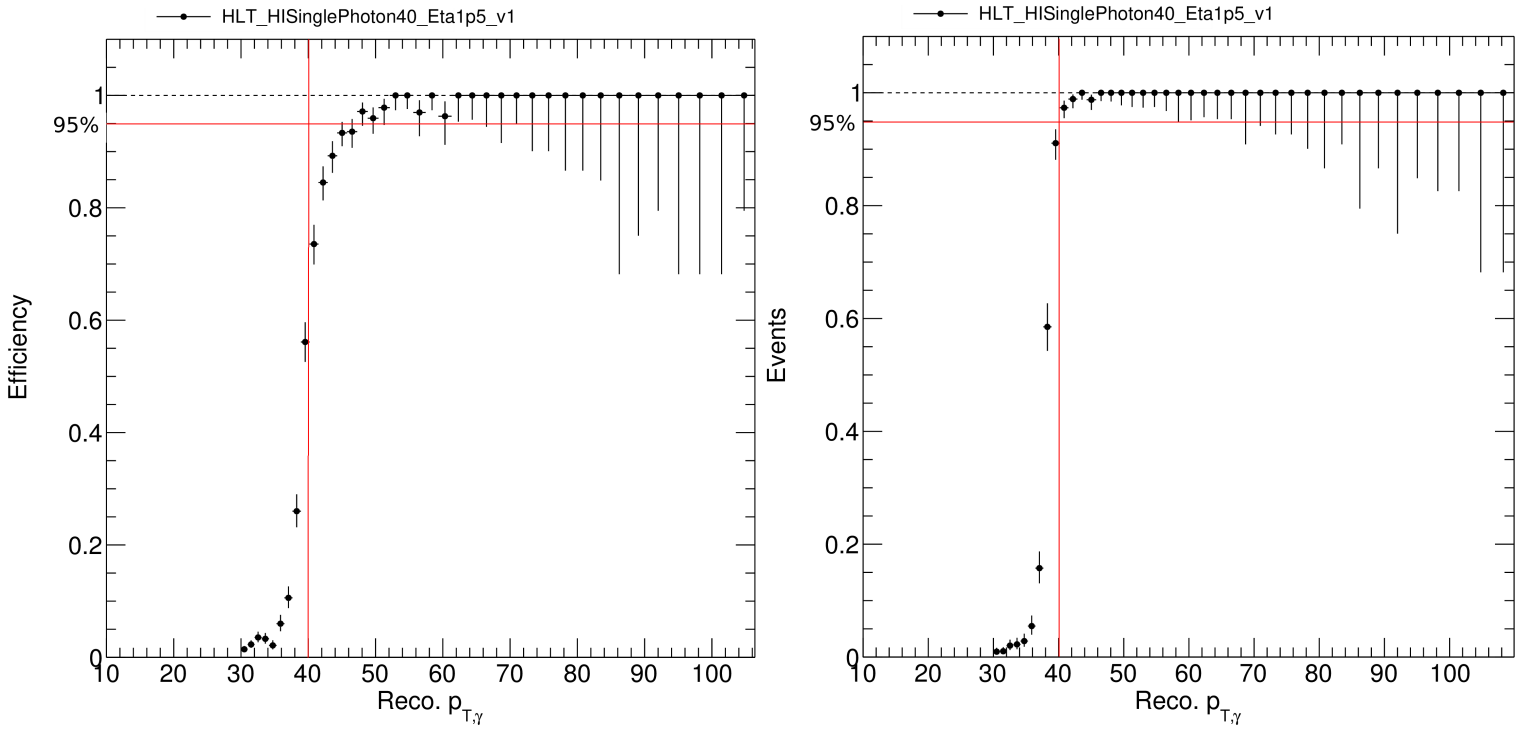

Figure 2-4: A plot of the photon trigger efficiency in pp data (left) and PbPb data (right) as a function of the reconstructed E_T, computed using a minimum bias data sample. It shows that for photons with an $p_T > 40$ GeV/c the trigger averaged greater than 95% efficiency in both cases.

Several different triggers were used for this analysis. The primary trigger was a requirement that there be one photon with transverse momentum larger than 40 GeV/c– this trigger formed the dataset used for the photon candidates. A minimum bias trigger was used to collect data that was used for event mixed background subtraction and numerous cross-checks. Triggers requiring jets above several energy thresholds created datasets used to derive jet energy corrections and calibrations. Di-muon and Di-electron triggers were used to create a Z-boson dataset which was used to further calibrate the jets and also provide energy corrections for photons.

Chapter 3

Reconstruction of Physics Observables

In order to translate the electrical signals the detector records into usable physics observables, there is a long chain of reconstruction software that is run. The most basic building blocks of the physics observables are ECAL towers, HCAL towers, tracker hits, and muon chamber hits. In turn, photons are constructed by carefully grouping ECAL towers, tracks are formed by carefully connecting tracker hits, muons (not used in this analysis) are formed from both tracker and muon chamber information, and Jets use a combination of all types of input.

3.1 Photons

Photons are reconstructed in the CMS detector using information from the ECAL.

3.1.1 Basic Clusters

One starts from reconstructed energy deposits ("hits") obtained with the barrel and endcap ECAL. Photon (and electron) showers deposit their incident energy in several crystals, with about 94% of the energy contained in 3×3, and about 97% in 5×5 crystals. Summing the energy in such fixed arrays gives the best performance for

photons which have not converted into e^+-e^- pairs before striking the calorimeter. However, the presence of material in front of the ECAL results in photon conversions. In this case, the energy reaching the calorimeter is spread in ϕ due to the presence of the magnetic field. To reconstruct the energy, one searches for local accumulations of hits, called "clusters" or "basic clusters", which are then grouped into "super clusters" that are composed of several ordinary clusters.

In the study of PbPb collisions, the Island algorithm is used for the clustering. The algorithm begins by searching for seeds, which are defined as crystals (reconstructed hits) with a transverse energy above a threshold ($E_T > 0.5$ GeV for barrel and $E_T > 0.18$ GeV for endcap). Starting from the seed position, adjacent crystals are examined, scanning first in the ϕ and then in the η direction. Crystals are added to the cluster until either a rise in energy or a crystal that has already been assigned to a different cluster (or that has not been hit) is encountered.

3.1.2 Super Clusters

Next, the basic Island clusters are clustered into super clusters. The procedure is seeded by searching for the most energetic cluster above a transverse energy threshold ($E_T > 1$ GeV) and then collecting all the other nearby clusters which have not yet been used in a narrow η-window ($\Delta\eta = 0.07$ for barrel and $\Delta\eta = 0.14$ for endcap), and a much wider ϕ-window (0.8 for barrel and 0.6 for endcap) due to the spread of the shower caused by the intense magnetic field. Details about the island algorithm can be found in Ref. [31].

In this analysis, the photon candidates in the barrel ECAL region ($|\eta| < 1.44$) and $p_{\mathrm{T}} > 40$ GeV are selected for further studies.

3.1.3 Shower Shape

In order to differentiate photons which come from the hard scattering event and those which come from neutral meson decay, the fine granularity of the CMS ECAL is leveraged. A modified 2nd moment of the electromagnetic shower energy distribution

in the η direction is measured for each photon, described in Eqs.3.1. Photons with a large $\sigma_{\eta\eta}$ are statistically more likely to be two close-by photons which originated from a boosted neutral meson decay, while those with narrow showers are more likely to be single photons that come from other processes. Note that the shower width in the ϕ direction is not as useful because the strong magnetic field inside the CMS ECAL spreads out the electromagnetic shower in the ϕ direction.

$$\sigma_{\eta\eta}^2 = \frac{\sum_i^{5\times5} w_i(\eta_i - \eta_{5\times5})^2}{\sum_i^{5\times5} w_i}, w_i = \max(0, c + \ln\frac{E_i}{E_{5\times5}}), \tag{3.1}$$

where E_i and η_i are the energy and pseudorapidity of the i^{th} crystal within the 5×5 electromagnetic cluster. $E_{5\times5}$ and $\eta_{5\times5}$ are the energy and averaged η of the 5×5 crystals. The value of c is a constant which is set to 4.7 and is effectively a cutoff on the crystal energy.

3.1.4 Isolation Energy

In order to increase the fraction of prompt photons (removing fragmentation and decay photons) in the sample, a requirement that the photon candidate be isolated is used. At generator level, the requirement is that the sum of transverse energy of all generated particles in a cone of R=0.4 around the photon ($GenIso$) must be less than 5 GeV. After reconstruction, a series of isolation variables are used to correlate to this generator-level isolation.

The first isolation variable is the ratio of hadronic to electromagnetic energy (H/E) in a cone of $\Delta R = 0.15$ around the photon candidate. The hadronic energy is measured as rechits in the HCAL, while the electromagnetic energy comes from ECAL clusters. Photon candidates with values of H/E above 0.1 are rejected since they likely are fragmentation photons from jets.

The next group of isolation variables are computed as subdetector energy sums in the area surrounding the photon candidate. For a given photon candidate, the energy deposits in the ECAL, HCAL, and Tracker in a cone of $\Delta R = 0.4$ are computed. $ISO_4^{UncorrECAL}$ refers to the ECAL energy sum while $ISO_4^{UncorrHCAL}$ refers to the

HCAL sum. Note that the ECAL sum explicitly excludes the energy of the photon candidate itself. The sum is computed over basic clusters in the ECAL and rechits in the HCAL. $ISO_i^{UncorrTrack}$ is a sum of all tracks inside the $\Delta R = 0.4$ which have $p_T > 2\,\mathrm{GeV}/c$.

The underlying event of the PbPb collision modifies the isolation energy of the photon candidates relative to pp collisions. This underlying event is subtracted separately from each subdetector energy sum by finding the mean energy in an η strip of $\Delta\eta = 0.8$ total width centered on the photon candidate and using the full ϕ coverage. After normalizing to the area of the cone, this mean value is subtracted from the uncorrected subdetector energy sums to form the corrected energy sums,

$$ISO_4^{ECAL} = ISO_4^{UncorrECAL} - \langle ECALE_{Ti}^{background} \rangle \tag{3.2}$$

for ECAL clusters and

$$ISO_4^{HCAL} = ISO_4^{UncorrHCAL} - \langle HCALE_{Ti}^{background} \rangle \tag{3.3}$$

for HCAL hits, and

$$ISO_4^{Track} = ISO_4^{UncorrTrack} - \langle TrackE_{Ti}^{background} \rangle \tag{3.4}$$

for reconstructed tracks. Fig. 3-1 shows this underlying event correction schematically.

The sum of the 3 subdetector isolation energy sums is used as the cut variable when separating isolated from non-isolated photon candidates:

$$SumIso = ISO_4^{ECAL} + ISO_4^{HCAL} + ISO_4^{Track} \tag{3.5}$$

The $SumIso$ is further corrected so that it is flat as a function of the ϕ distance between the photon and the v2 event plane. Photon candidates which sit on top of the v2 event plane are more likely to have more soft particles in their isolation cones than those which sit at 90 degrees from the event plane. The $SumIso$ is corrected

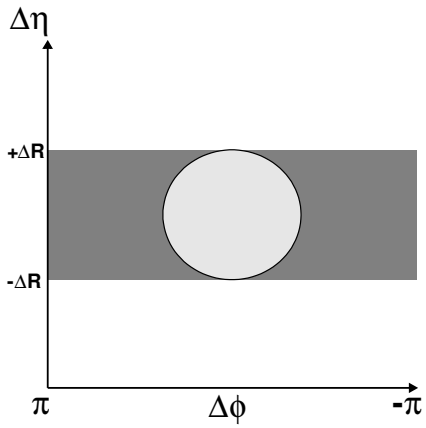

Figure 3-1: Schematic of the underlying event correction of the subdetector isolation energies.

as a function of the angle to the event plane such that the mean in each correction bin is equal to the mean $SumIso$ of the entire sample. This has negligible effect on any of the physics observables, but allows us to state that we have no event plane dependence.

3.1.5 Photon Energy Correction

In this analysis, a photon energy correction due to the underlying event contribution is obtained from PYTHIA+HYDJET. In order to validate this correction, a study with $Z^0 \rightarrow e^+e^-$ simulations is performed. Events which have two photon candidates with $p_{\mathrm{T}} > 40$ GeV/c in the ECAL barrel are selected [31]. Photon candidates are requires to have $\sigma_{\eta\eta} < 0.011$ which is slightly looser than the photon selection. The photon candidates are required to match with a reconstructed electron candidate (anti-selection of electron rejection described in Section. 5.1.2) and pass an isolation criteria of $ISO_i^{ECAL} + ISO_i^{HCAL} < 5$ GeV (track isolation ISO_i^{Track} is not used in order to keep all electron candidates). The p_{T} and direction of the photon candidates are used to calculate the Z^0 mass.

The photon energy correction factors are obtained from the ratio of the reconstructed photon energy to the gen-level photon energy, and applied as a function of centrality and reconstructed photon energy. The size of the correction is at the 0–2%

level for events with 30–100% centrality, and increases to around 5% for the lower energy (around 40–50 GeV) photon candidates in collisions with 0–10% centrality.

The residual difference after correction between the Monte-Carlo and Data samples are used to quantify the systematic uncertainty of the photon energy scale. See Section 5.6.1 for more.

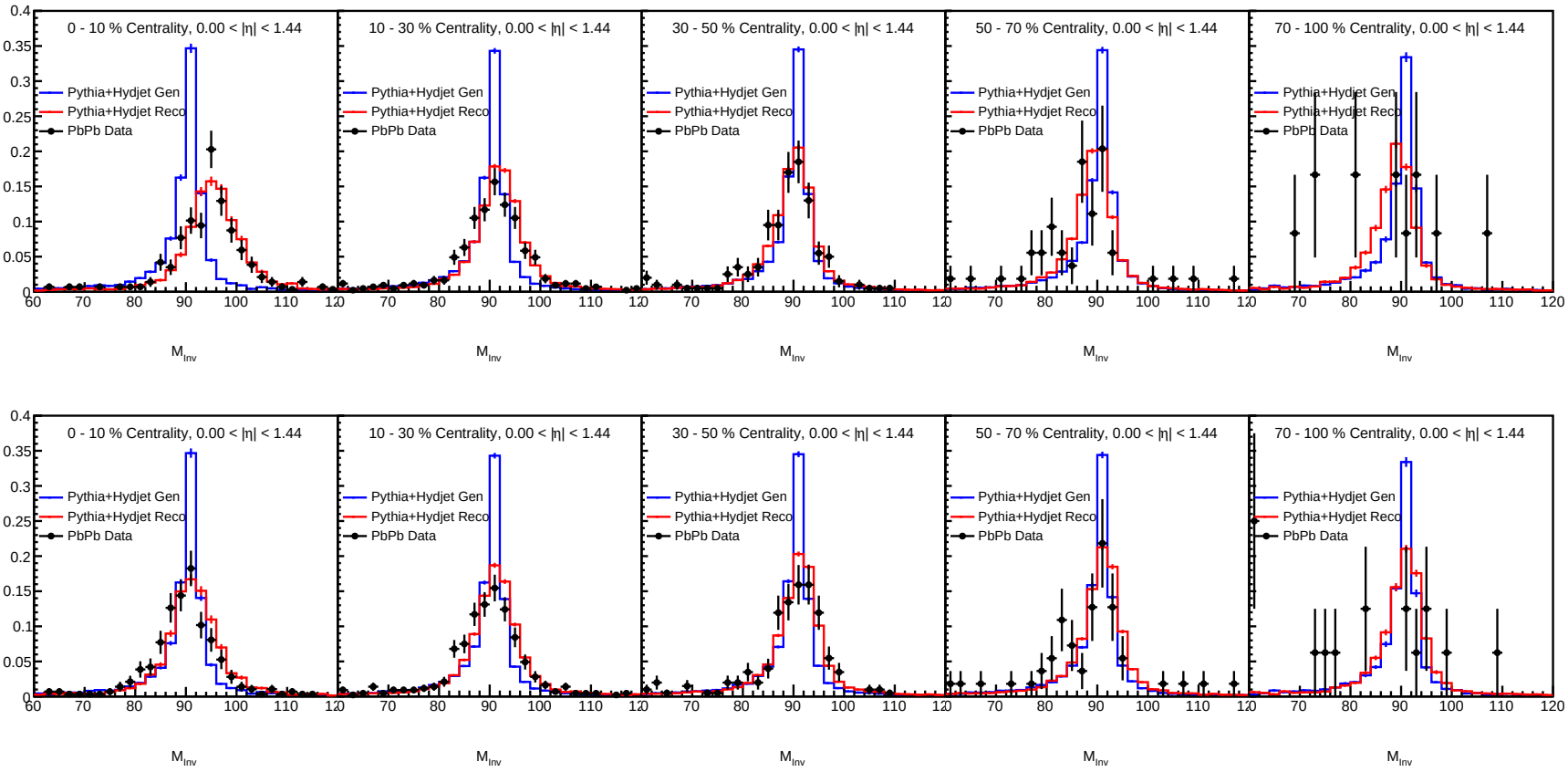

Figure 3-2: (Top) The uncorrected Z invariant mass spectrum for electron-matched photon candidates, for different centrality bins and (Bottom) after correction.

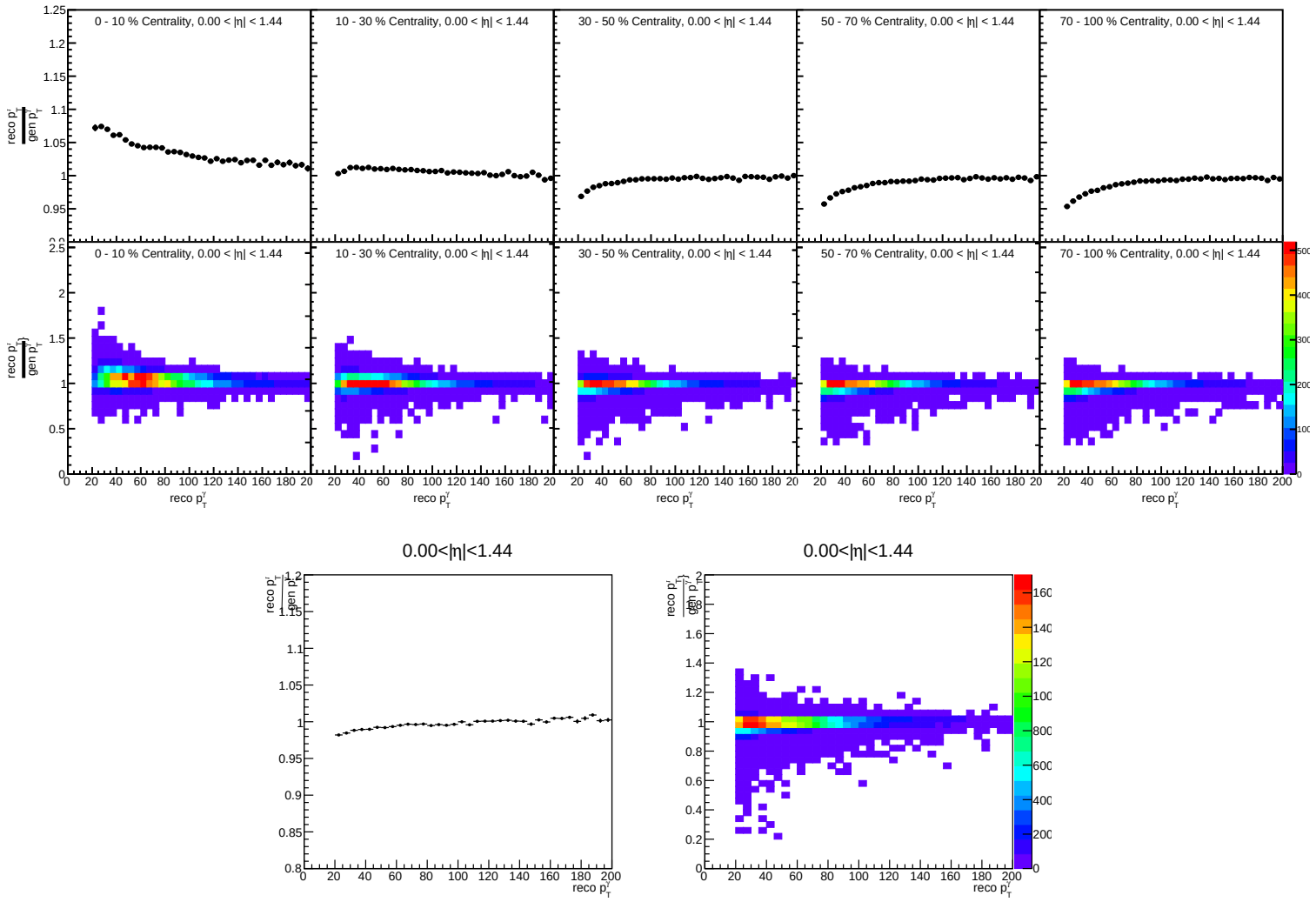

Figure 3-3: The mean and scatter plot of the ratio of the reconstructed photon p_{T} to the generator level photon p_{T} for electron-matched photons, as a function of the reconstructed photon p_{T}, (Top) for different centrality bins in PbPb and (Bottom) for pp.

3.2 Tracks

Tracking in Heavy Ion collisions is a difficult task due to the very high multiplicity and single nominal vertex. The tracking algorithm used in CMS for Heavy Ion collisions is a modified form of that used for pp tracking, with stricter cuts and extra iterations to try to reduce run time while keeping efficiency high.

The algorithm is detailed below. After each step, the associated hits for the tracks found in that iteration are removed from the collection to reduce the combinatorial complexity for future iterations. At the end, tracks from each iteration are merged together into the single final collection.

1. First the vertex is found by scanning along the z direction and finding the number of pixel triplet seeds that are compatible with that vertex position. The vertex is the location with the maximum number of compatible seeds.

2. Next, tracks are made from pixel triplet seeds, allowing tracks down to 0.9 GeV/c.

3. Next, the requirements for compatibility with the vertex are reduced, allowing further displacement from vertex.

4. Next, pixel triplets with p_{T} down to 0.4 GeV/c are allowed to form tracks.

5. Next, pixel pairs with p_{T} above 4 GeV/c are allowed to form tracks.

6. Last, an additional iteration inside calorimeter jets above 100 GeV/c is run to allow better tracking efficiency near jets at high track p_{T} above 10 GeV/c.

After the tracking collection is performed, a selection called "high purity" is applied, which is a multivariate cut based on track error variables. An iterative efficiency correction is applied to the high purity track collection, iterating over p_{T}, η and ϕ position, event centrality, and distance to a jet (a proxy for local track density).

3.3 Jets

Jet reconstruction in heavy-ion collisions in CMS is performed with the anti-k_T jet algorithm that is encoded in the FastJet framework [13]. Although the default algorithm for pp collisions is anti-k_T with a resolution parameter of $R = 0.4$, a smaller resolution parameter of $R = 0.3$ is used to minimize the effects of heavy ion background fluctuations in this analysis. While it is possible to subtract the heavy-ion background with the FastJet framework using a definition of an active 4-vector area (A_{jet}), for this analysis an algorithm that is a variant of an iterative "noise/pedestal subtraction" technique is used to estimate the heavy ion background event-by-event [32, 33], with details described in Section 3.3.1 The anti-k_T jet algorithm is run over the Particle Flow (PF) objects that are reconstructed by matching tracks from the Tracker to the ECAL and HCAL [34, 35].

The PbPb particle flow algorithm uses heavy-ion tracking which has different efficiency than pp tracking. η and p_{T} dependent energy correction factors for the jets are derived from the analysis of PYTHIA sample at 5.02 TeV, similar to those used in pp [36, 37]. In analyses of pp data or PYTHIA, i.e. without heavy ion background, the pileup subtraction is not applied and the standard pp L2L3 corrections are used. Jet p_{T} shown in this document have the energy correction applied unless otherwise marked.

3.3.1 Subtraction of Underlying Event

One of the major challenges in jet reconstruction is understanding the uncorrelated background within the selected jet cone due to the large multiplicity in heavy-ion collisions. This uncorrelated background may worsen the jet energy resolution. Additionally, the high multiplicity background makes accurate detector simulation very hard as non-linear effects may come in to play; this may cause worse resolution in data compared to Monte-Carlo. This background is studied as a function of centrality, p_{T}, and η, the last of which is necessary given reconstruction differences in the Barrel and Endcap regions of the CMS detector.

The algorithm to estimate and subtract the background energy for each jet event-by-event is a variant of an iterative "noise/pedestal subtraction" technique[33], which is designed for discrete quantification of the energy in η and ϕ and ideal for a calorimetric measurement. To use the same subtraction code to candidates reconstructed with particle flow, which have a continuous distribution in momentum space, a calorimeter tower geometry is imposed on the PF objects. This is performed by summing up the p_{T} of the PF candidates that point to a fixed $\eta \times \phi$ bin that corresponds to the HCAL cell granularity, although evaluated with respect to the momentum values of candidates at the vertex, not the calorimeter surface. After this projection, the mean value and dispersion of the energies recorded in the calorimeter cells are calculated for all rings of cells at constant pseudorapidity, η.

The value of this pedestal function, $\mathrm{P}(\eta)$, containing the information on the mean and dispersion, is then subtracted from all cells. If a cell energy comes out negative, it is set to zero. The algorithm subtracts $\langle E_{\mathrm{cell}} \rangle + \sigma(E_{\mathrm{cell}})$ from each cell in order to compensate for the bias caused by this elimination of negative energy. Jets are then reconstructed, using the standard anti-k_T algorithm, from the remaining non-zero particle flow objects. In a second iteration, the pedestal function is recalculated using only calorimeter cells outside the area covered by reconstructed high p_T jets ($p_T > 15$ GeV/c). The threshold of 15 GeV/c was chosen to optimize the final extracted jet energy resolution. The cell energies are updated with the new pedestal function (again subtracting mean plus dispersion) and the jets are reconstructed once more using the updated calorimeter cells. The performance of this algorithm in documented in Ref. [33].

3.3.2 Jet Energy Smearing

The energy and angular resolution of jets is worse in PbPb collisions than in pp collisions. Several of the studied observables are very sensitive to this, since on a steeply falling spectrum degraded energy resolution can significantly impact the number of jets found at a given energy. There are two options for avoiding this issue. The first is to "unfold" the jet spectrum, a procedure which conceptually involves inverting a the

convolution matrix describing the detector resolution. This procedure is difficult because it is easy to introduce biases and numerical instabilities, and therefore a proper treatment could potentially take a lot of person-time. The second option is to smear the pp energy to match the resolution in PbPb collisions. Due to time and manpower contraints, this was the method we chose to use.

The Gaussian standard deviation σ of p_T^{Reco}/p_T^{Gen} can be parameterised using the expression

$$\sigma(\frac{p_T^{Reco}}{p_T^{Gen}}) = \sqrt{C^2 + \frac{S^2}{p_T^{Gen}} + \frac{N^2}{(p_T^{Gen})^2}}, \tag{3.6}$$

where the quantities C, S, and N are fitted parameters. Loosely, C describes the intrinsic detector resolution, S describes the resolution of the jet algorithm, and N describes the effect of the Heavy Ion background. By using these parameters generator-level jet energy can be smeared to match with detector-level jet energy.

For this analysis, the detector-level jet energy of pp collisions is smeared to match the PbPb resolution through relative resolution which is defined by the expression

$$\sigma_{rel} = \sqrt{(C_{PbPb}^2 - C_{pp}^2) + \frac{(S_{PbPb}^2 - S_{pp}^2)}{p_T^{Gen}} + \frac{(N_{PbPb}^2 - N_{pp}^2)}{(p_T^{Gen})^2}}, \tag{3.7}$$

where the quantities C, S, and N are from Table 3.1.

The detector-level jet angular resolution of pp collision can be smeared using a similar approach. The same functional form as in eq. 3.6 is used to parametrize standard deviation of $|\phi^{Reco} - \phi^{Gen}|$.

$$\sigma(|\phi^{Reco} - \phi^{Gen}|) = \sqrt{C^2 + \frac{S^2}{p_T^{Gen}} + \frac{N^2}{(p_T^{Gen})^2}}, \tag{3.8}$$

Using eq. 3.7 the detector-level jet angular deviation in pp collisions is smeared to match the PbPb resolution. The quantities for jet angular resolution are given in Table 3.2.

Centrality	C	S	N
0-30%	0.06	1.23	7.38
30-100%	0.06	1.23	2.10
0-10%	0.06	1.23	8.38
10-30%	0.06	1.23	5.88
30-50%	0.06	1.23	3.24
50-100%	0.06	1.23	0
pp	0.06	0.91	0

Table 3.1: Jet energy resolution CSN fitting parameters for different centrality bins, computed on PYTHIA and PYTHIA+HYDJET samples.

Centrality	C	S	N
0-30%	0	0.1651	1.864
30-100%	0	0.1646	1.04
0-10%	0	0.125911	2.23898
10-30%	0	0.179847	1.56128
30-50%	0	0.121572	1.21751
50-100%	0	0.168879	0.798885
pp	0	0.1222	0.5818

Table 3.2: Angular resolution CSN ϕ fitting parameters for different centrality bins, computed on PYTHIA and PYTHIA+HYDJET samples.

Chapter 4

Monte-Carlo

The use of simulated data to validate both detector performance and analysis expectations is a critically important part of modern high energy physics experiments. Simulated data produced by Monte-Carlo generators in CMS is used during detector commissioning to validate the performance of detector components, for testing the performance of reconstruction algorithms, for validating changes to reconstruction software, to provide a baseline prediction of standard model physics, and to plan for conditions during real data taking. Monte-Carlo gives analyzers a way of validating analysis methods and generating corrections in some cases.

Simulated data requires two things: a Monte-Carlo generator and a detailed simulation of the detector. General Monte-Carlo generators include many tunable parameters in order to reproduce a large array of physics measurements in different collision conditions. Niche Monte-Carlo generators concentrate on implementing fixed order perturbative calculations or specific phenomenology in order to test for specific results. The generator produces a list of "final state" particles which are then processed by a detector simulation to account for the affects of material interactions and electronic readout. The simulation is then reconstructed using the same process as real data. By comparing the input list of particles (referred to as "gen" particles) to the reconstructed output ("reco" particles) the performance of the detector can be evaluated.

Before a detector has collected real data, the reliability of simulated data may

not be particularly strong, but after real data is collected the detector simulation can be improved to match the results from real data. The detector simulation is constantly improved, and for this analysis was in a very mature state. Additionally, the generator itself is constantly re-tuned to match observables as collision conditions change.

In this analysis simulated data is used directly as the signal template in determining the purity of the isolated photon sample (Section 5.1.4) as well as for cross checks at every step of the analysis procedure. It was particularly helpful in developing and building trust in the mixed event method of background subtraction for combinatorial jets (Section 5.4).

4.1 PYTHIA

This analysis makes heavy use of the PYTHIA general purpose high-energy event generator, version 8.1 [38]. PYTHIA is not a fixed order event generator, but instead a coherent set of physics models that covers hard scattering particle production, initial and final state parton showers, and decays. PYTHIA version 8.1 is a re-write in C++ of PYTHIA version 6.4 which was a FORTRAN based program with a long and venerable history. PYTHIA is a heavily-tuned generator with many options. This analysis uses the CUETP8M1 tune, made specifically for CMS and derived from the default Monash tune [39].

PYTHIA is specific to lepton-lepton or single hadron-single hadron collisions, and thus does not implement any potential multi-hadron physics processes. For Heavy Ion collisions, it is used to study the high p_{T} hard scattering products and as a prediction of observables in the absence of nuclear matter effects. It must be supplemented by some generator which produces the low p_{T}, high multiplicity environment of Heavy Ion collisions in order to study detector response and low p_{T} observables.

4.2 HYDJET and Embedding

To simulate the soft high-multiplicity underlying event of Heavy Ion collisions the HYDJET version 1.9 event generator is used. HYDJET modifies the jet physics of PYTHIA and combines hard multijets from this modification with a soft hydrodynamic background to produce the underlying event. HYDJET alone is used as a simulation of minimum bias Heavy Ion events without significant contribution from hard-scattering.

In order to simulate photon+jet events for this analysis, which include both high p_{T} partons from a hard scattering and the soft underlying event, PYTHIA partons are embedded into HYDJET "background" before detector simulation. The end result is an embedded sample, with a hard component primarily generated by PYTHIA and soft components primarily generated by HYDJET. This combination allows us to study changes in resolution or isolation (Section 3.1.4) due to the presence of extra, soft particles not present in pp collisions or PYTHIA alone.

4.3 Samples

Two sets of Monte-Carlo were produced for this analysis. The first, called "AllQCDPhoton" or "signal", turns on all prompt photon and QCD processes in PYTHIA and filters it for the presence of a high p_{T} photon which is either directly from the hard scattering or fragmented from a jet. The second, called "EmEnrichedDijet" or "background", turns on only QCD process and filters for a high p_{T} neutral meson (π^0, η, η', or ω). The AllQCDPhoton samples are used directly in the analysis as for the signal template of the purity determination (Section 5.1.4), while both samples are used for validation of the analysis methods and detector performance.

Each type of sample was produced for several settings of the $\hat{p}_{\mathrm{T}}$ PYTHIA parameter, which controls the minimum momentum transfer of the hard scattering, effectively changing the p_{T} spectra of the produced particles. Changing this parameter allows us to produce high statistics at high photon p_{T}. Table 4.1 shows the statistics for the

PYTHIA samples used for studying pp collisions, while Table 4.2 shows the statistics for the embedded PYTHIA+HYDJET samples used to study PbPb collisions.

Table 4.1: Monte-Carlo samples for pp simulations.

Generator	Event Type	$\hat{p}_{\mathrm{T}}$	nEvents
PYTHIA	EmEnrichedDijet	30	201K
PYTHIA	EmEnrichedDijet	50	204K
PYTHIA	EmEnrichedDijet	80	200K
PYTHIA	EmEnrichedDijet	120	200K
PYTHIA	EmEnrichedDijet	170	199K
PYTHIA	AllQCDPhoton	15	172K
PYTHIA	AllQCDPhoton	30	197K
PYTHIA	AllQCDPhoton	50	200K
PYTHIA	AllQCDPhoton	80	203K
PYTHIA	AllQCDPhoton	120	199K

Table 4.2: Monte-Carlo samples for PbPb simulations.

Generator	Event Type	$\hat{p}_{\mathrm{T}}$	nEvents
PYTHIA+HYDJET	EmEnrichedDijet	30	194K
PYTHIA+HYDJET	EmEnrichedDijet	50	203K
PYTHIA+HYDJET	EmEnrichedDijet	80	200K
PYTHIA+HYDJET	EmEnrichedDijet	120	201K
PYTHIA+HYDJET	EmEnrichedDijet	170	202K
PYTHIA+HYDJET	AllQCDPhoton	15	400K
PYTHIA+HYDJET	AllQCDPhoton	30	400K
PYTHIA+HYDJET	AllQCDPhoton	50	400K
PYTHIA+HYDJET	AllQCDPhoton	80	400K
PYTHIA+HYDJET	AllQCDPhoton	120	400K
HYDJET	Minimum Bias		478K

4.4 Re-Weighting

The Monte-Carlo samples used were reweighted to match the event primary vertex and centrality distributions in data. Figure 4-3 shows the weights applied to PbPb and pp Monte-Carlo.

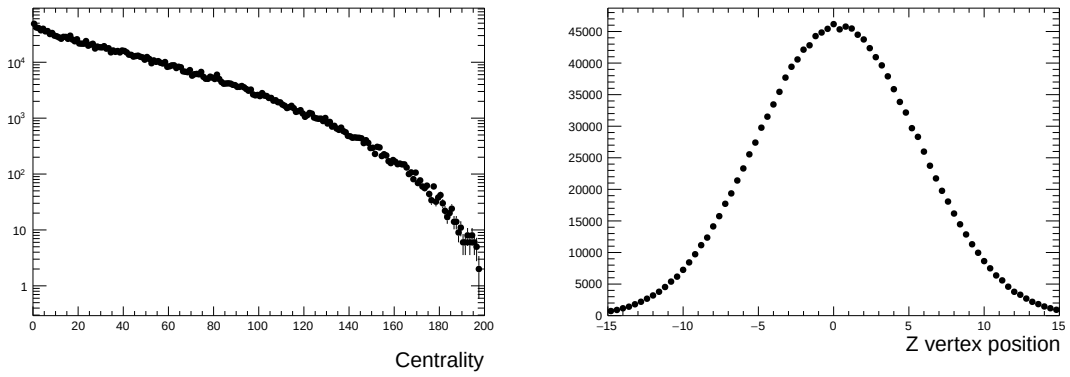

Figure 4-1: Left: The centrality distribution in PbPb data, which the Monte-Carlo is matched to. Right: The Z vertex distribution in PbPb data, which the Monte-Carlo samples are matched to.

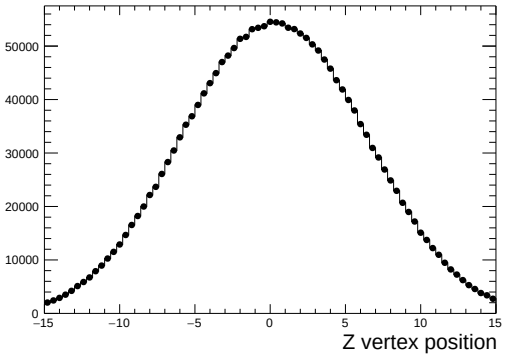

Figure 4-2: The Z vertex distribution in pp data, which the Monte-Carlo samples are matched to.

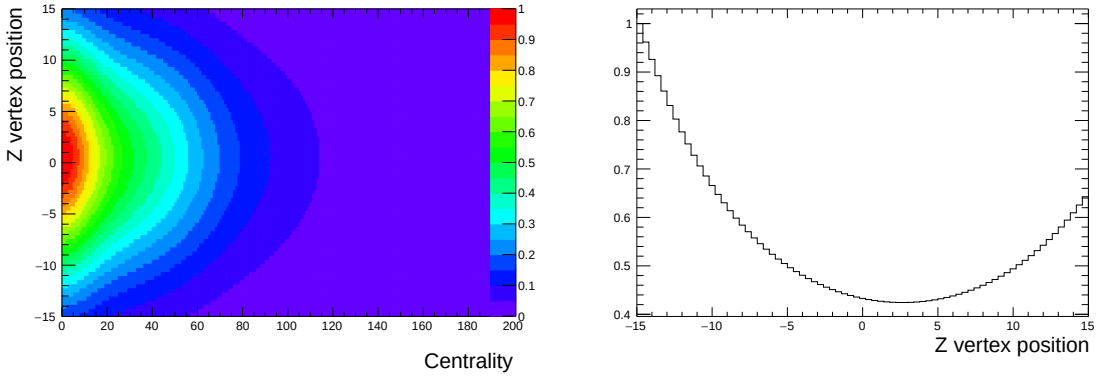

Figure 4-3: Left: The weights used to reweight PbPb Monte-Carlo to match the vertex and centrality distribution in data. Right: The weights used to reweight pp Monte-Carlo to match the event primary vertex distribution in data.

Chapter 5

Analysis

5.1 Photon Selection

After reconstruction, several cuts are applied to the photon candidates in order to remove electronics noise, reject possible electron contamination, and increase the relative purity of prompt photons.

5.1.1 Noise Reduction

Charged particles from the collision which directly hit the ECAL readout electronics cause false signals to be produced, these are referred to as "spikes", since they appear to be single crystals with very high p_{T} and no surrounding energy. ECAL spike rejection is done by requiring the *Swiss Cross Variable* $(1 - E_4/E_1) < 0.9$, where E_1 is the highest energy crystal in the cluster and E_4 is the total energy of the four crystals around the highest energy crystal, and timing of the hits $|t| < 3$ ns. The fraction of residual spikes with respect to real isolated photon signal are estimated to be smaller than 2% by a data-driven method [31].

For 2015 PbPb Data, an additional source of ECAL noise was found, stemming from 5x5 sets of ECAL crystals with erroneous energies all identical in the 5x5 square. These are the result of ECAL energies being erroneously reconstructed from L1 Trigger error messages. A simultaneous cut on three energy ratios E3x3/E5x5,

E1x5/E5x5, and E2x5/E5x5 was made to eliminate this noise source (which was not present in PbPb Monte-Carlo, pp Data, or pp Monte-Carlo). The total fraction of signal photons removed by the cut in PbPb Monte-Carlo was 0.4%, while the fraction of events removed from the photon-triggered PbPb data sample was 5.5%.

5.1.2 Electron Rejection

In order to suppress the contamination from electrons which come from the decay product of W and Z bosons as well as Drell-Yan processes and inclusive c- and b-jets, if a reconstructed photon candidate matches the supercluster reference of an electron candidate within $|\Delta\eta| < 0.03$ and $|\Delta\phi| < 0.03$, this photon candidate is removed. The procedure is identical to the procedure detailed in the PbPb isolated photon analysis [25] and photon-jet analysis [31]. Isolated photon candidates can be contaminated by remnant electrons after the rejection. The amount of contamination after the rejection is estimated by rejection efficiency from PYHIA Z to EE sample. Rejection efficiency is around 65 % and 35 % of electrons remains after the rejection.

5.1.3 Isolation

As discussed in Sec. 3.1.4, the amount of energy in a cone around each photon candidate, $SumIso$, is computed. Candidates with $SumIso < 1$ GeV are considered isolated for the purposes of this analysis. The cut of 1 GeV was chosen such that it matched previous publications while still giving good performance at 5.02 TeV collisions. A sideband of non-isolated candidates, $10\,\text{GeV} < SumIso < 20\,\text{GeV}$ is considered pure background and used to determine the purity, see Sec. 5.1.4.

5.1.4 Photon Purity Determination

The selection criteria described above yield a relatively pure sample of isolated photons. Yet, there are still non-prompt photons, such as those from an isolated π^0 carrying a large fraction of the parent fragmenting parton energy, which can pass the isolation cuts. Photons from π^0 decay will be nearly collinear, but will have a statis-

tically larger spatial extent which can be exploited. The fraction of those remaining backgrounds are statistically calculated using a two-component fit of the shape of the electromagnetic shower in ECAL ($\sigma_{\eta\eta}$), called the Template method.

A template is defined as the probability distribution function of $\sigma_{\eta\eta}$ of either pure photons (signal template) or pure background (e.g. π^0) (background template). The signal template was obtained from Monte-Carlo photon samples (PYTHIA+HYDJET for PbPb or PYTHIA for pp), and the background template was obtained from data in a SumIso sideband (10 GeV< SumIso < 20 GeV) where the background is enriched. The yield of signal photons is estimated with a binned maximum likelihood fit to the $\sigma_{\eta\eta}$ distribution of data with the signal and background templates. The purity is defined as the fraction of photons with $\sigma_{\eta\eta} < 0.01$ (chosen to maximize the purity value) which are accounted for by the signal template.

Tables 5.1 and 5.2 summarize the purity values obtained across all p_{T} and centrality bins for PbPb and pp data respectively. Figure 5-1 shows an example of the template fitting procedure for a subset of the bins used in the analysis.

	0-100%	0-30%	30-100%	0-10%	10-30%	30-50%	50-100%
$p_{\mathrm{T}}^{\gamma} > 40$	0.704	0.695	0.745	0.670	0.712	0.747	0.737
$p_{\mathrm{T}}^{\gamma} > 60$	0.725	0.708	0.785	0.681	0.730	0.775	0.825
$40 < p_{\mathrm{T}}^{\gamma} < 50$	0.692	0.684	0.730	0.654	0.700	0.733	0.714
$50 < p_{\mathrm{T}}^{\gamma} < 60$	0.707	0.699	0.748	0.672	0.722	0.754	0.726
$60 < p_{\mathrm{T}}^{\gamma} < 80$	0.719	0.702	0.785	0.676	0.721	0.770	0.835
$p_{\mathrm{T}}^{\gamma} > 80$	0.737	0.721	0.789	0.685	0.751	0.787	0.816
$80 < p_{\mathrm{T}}^{\gamma} < 100$	0.722	0.702	0.787	0.678	0.725	0.771	0.850
$p_{\mathrm{T}}^{\gamma} > 100$	0.758	0.749	0.799	0.700	0.792	0.821	0.797

Table 5.1: Summary of the photon purity in PbPb data for the various centrality and p_{T}^{γ} bins.

	Purity
$p_{\mathrm{T}}^{\gamma} > 40$	0.820
$p_{\mathrm{T}}^{\gamma} > 60$	0.841
$40 < p_{\mathrm{T}}^{\gamma} < 50$	0.819
$50 < p_{\mathrm{T}}^{\gamma} < 60$	0.827
$60 < p_{\mathrm{T}}^{\gamma} < 80$	0.841
$p_{\mathrm{T}}^{\gamma} > 80$	0.853
$80 < p_{\mathrm{T}}^{\gamma} < 100$	0.858
$p_{\mathrm{T}}^{\gamma} > 100$	0.851

Table 5.2: Summary of the photon purity for pp data for the various centrality and p_{T}^{γ} bins.

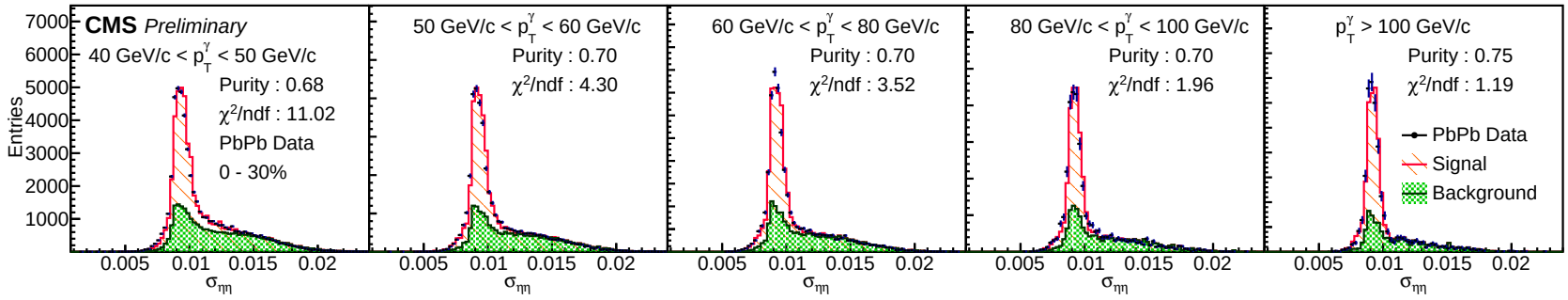

Figure 5-1: The shower shape variable ($\sigma_{\eta\eta}$) of photons from central (0-30%) PbPb collisions. The black points are PbPb data, the red histogram is the signal template from PYTHIA+HYDJET, and the green histogram is the background template from a non-isolated data sideband. The purity is defined as the fraction of isolated photons in the signal region $\sigma_{\eta\eta} < 0.01$ used in the isolated-photon+jet analysis.

5.2 Jet Selection

Jets with a corrected transverse momentum after background subtraction greater than 30 GeV/c and located inside $|\eta| < 1.6$ are used in this analysis.

5.3 Pairing Photons and Jets

For each event, the highest energy photon candidate which passes the noise rejection cuts inside $|\eta| < 1.44$ is selected. Every jet in the event which passes the above selection cuts is paired with the photon candidate, except those which are within $\Delta R = \sqrt{\Delta\eta^2 + \Delta\phi^2} < 0.8$ to avoid including jets that include the photon energy. For all observables which are not $\Delta\phi_{J\gamma}$, an additional cut of $\Delta\phi_{J\gamma} > \frac{7}{8}\pi$ is applied to the photon+jet pairs to increase the fraction of photon+jet pairs which come from the same hard scattering and reduce the number of 2-jet events.

Events are divided into 5 p_{T} bins of the leading photon – 40 GeV, 50 GeV, 60 GeV, 80 GeV, 100 GeV and higher – for all pp and PbPb collisions. For PbPb, the events are divided again into 2 centrality bins – 0%-30% and 30%-100%. Certain observables are inclusive of $p_{\mathrm{T}}^{\gamma} > 60$ GeV or $p_{\mathrm{T}}^{\gamma} > 80$ GeV and divided into 4 centrality bins, 0-10%, 10-30%, 30-50%, and 50-100%. The centrality bin was used to characterize the size of hot and dense systems made by the heavy ion collision. Photons are limited to be in the pseudo-rapidity range of $|\eta| < 1.44$, where the ECAL barrel is located. Jets are limited to the range $|\eta| < 1.6$ and $p_{\mathrm{T}} > 30$ GeV, which satisfies the energy scale is within 2% from unity so we can constrain the systematic uncertainty in the final results to be at the 10% level.

All the analyses – including the identification of direct photons and computation of photon+jet correlation results – are carried out by classifying the events in these centrality and photon p_{T} bins.

5.4 Background Subtraction

The photon and jet selections are implemented to suppress the background level. However the background rejection is not perfect and even after the full analysis selection, there still remain non-vanishing background photon+jet contributions from both fake photons and fake jets.

For the photons, the main background contribution comes from non-prompt neutral-meson decay photons as described in Section 5.1.4. For the jets, the background contribution comes from fake jets that are reconstructed from regional energy fluctuations in the high multiplicity heavy-ion underlying event, or from multiple interactions. This background contribution is important only for PbPb events and not pp samples. Background jets are by definition not correlated to the photon and therefore will appear equally at all ϕ. The background contaminations introduce a distortion of the final results. We correct for this by data-driven background subtraction techniques.

The data-driven background subtraction consists of three steps. First we estimate statistically the fraction of background photon+jet within the signal selection. Next we find from data sideband regions the shape of the background photon+jet in the physics observable of interest. Finally we scale the sideband shape according to the estimated contribution in the signal region and subtract it from the raw physics observable distribution in the signal region.

For the background photon+jet contribution arising from background photons, the photon purity is determined as in Section 5.1.4. We then create a background shape for each physics observable from a sideband region $0.011 < \sigma_{\eta\eta} < 0.017$ of nearly pure background. This region is dominated by background photons from neutral hadron decays. Finally we scale the background shape according to (1-Purity) and subtract it from the final spectra.

For the background photon+jet contribution arising from fake jets, we estimate the background contribution using a mixed event method in PbPb only. The method assumes that the fake jets are uncorrelated with the leading photon in the candidate photon+jet event. Thus we can reproduce the background by pairing the leading

photon from the candidate photon+jet event to reconstructed jets in a separate minbias event. Care is taken to ensure the the minbias event has similar characteristics as the photon+jet candidate event. In particular we choose a minbias event with the same centrality, primary vertex Z position, and 2nd-order event plane angle as the photon+jet candidate event. The 2nd-order event plane angle is the detector ϕ angle at which most energy from soft particles is observed; the modulation of energy as a function of ϕ is generally assumed to be due to the formation of the QGP which then undergoes pressure-driven expansion, turning an elliptically-shaped interaction region into an elliptically-shaped energy distribution. The 2nd-order event plane angle is roughly the same angle as the impact parameter between the two colliding nuclei.

There is an overlap region in the estimated background contributions where a background photon is paired with a background jet. The contribution from this background region would be subtracted twice if we performed the background photon and background jet subtractions. To prevent a doubling counting of the backgrounds, we first subtract the fake jet contribution from the fake photon+jet pairs.

The final formula of the background subtractions is:

$$N^{Corr} = N^{Raw} - N^{Bkg\ Jet} - (N^{Bkg\ \gamma} - N^{Bkg\ \gamma,Bkg\ Jet})\alpha, \tag{5.1}$$

where N^{Raw} is the raw spectrum in the signal selection region, $N^{Bkg\ Jet}$ is the spectrum shape in the mixed background events, $N^{Bkg\ \gamma}$ is the spectrum shape in the $\sigma_{\eta\eta}$ sideband region, and $N^{Bkg\ \gamma,Bkg\ Jet}$ is the spectrum shape in the photon sideband region in the mixed events. $\alpha = (1 - \text{Purity})$ is the scale factor to the estimated background photon contribution under the signal region. Lastly, N^{Corr} is the final corrected spectrum.

Figure 5-2 shows the effect of the background subtraction procedure in PbPb data and Monte-Carlo.

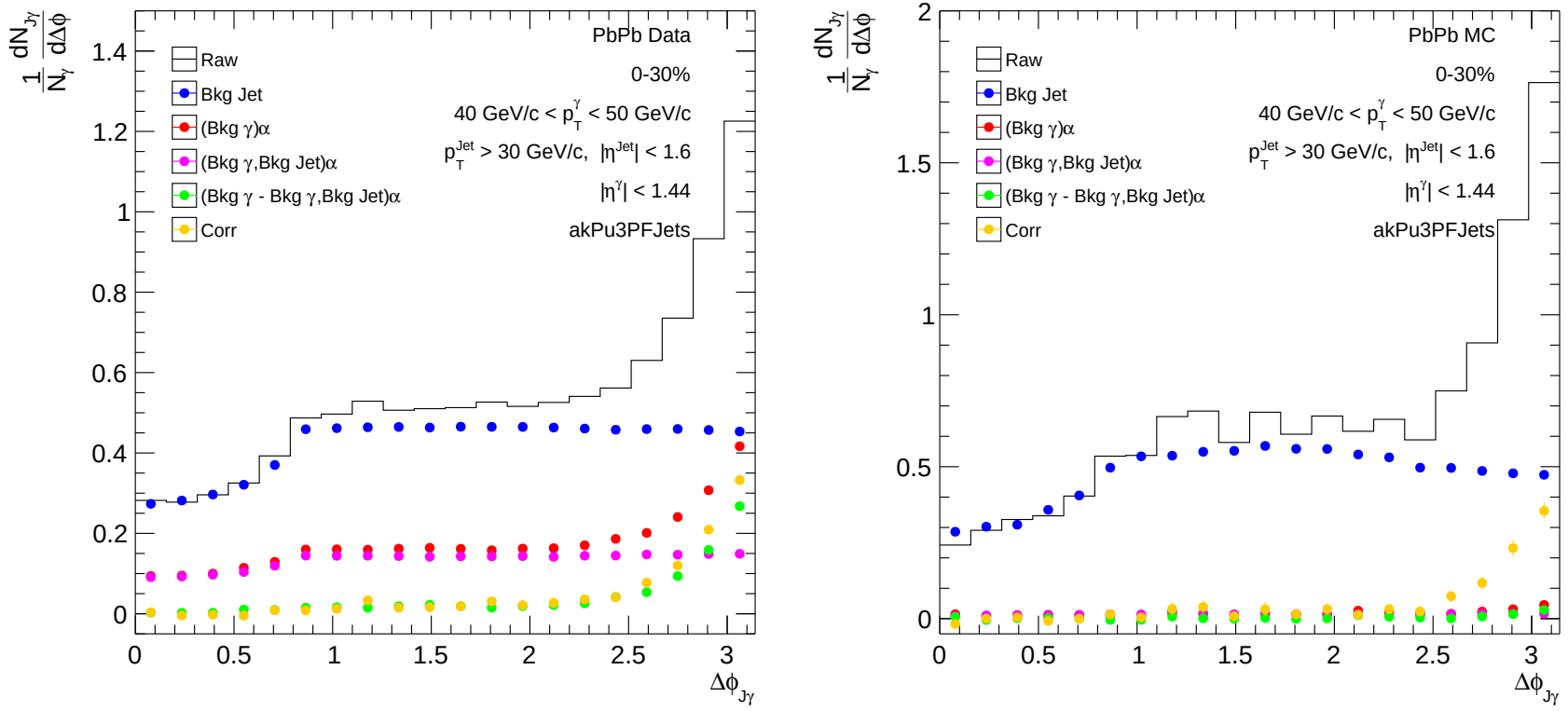

Figure 5-2: PbPb data (left) and Monte-Carlo (right): $\Delta\phi_{J\gamma}$ correlation before (black points/histogram) mixed-event jet background subtraction. It also shows the distribution of the photon+jet pairs from the mixed-events (blue points). The photon-related backgrounds are also shown, scaled by $\alpha = 1 - \text{Purity}$.

5.5 Observables

5.5.1 De-coplanarity, $\Delta\phi_{J\gamma}$

On traversal through the medium, the colored parton might be deflected by its interaction with the medium. $\Delta\phi_{J\gamma}$ defines the separation in ϕ between the photon and jet in the event. At tree level due to momentum conservation this should be a delta function at $\Delta\phi_{J\gamma} = \pi$, but the distribution is smeared out by initial state radiation (ISR), final state radiation (FSR), and other multi-loop processes in addition to the finite angular resolution of jets. See Figure 5-3 for a generator-level plot of $\Delta\phi_{J\gamma}$. If more photon+jet pairs are observed with small $\Delta\phi_{J\gamma}$ in PbPb collisisions compared to pp, this could be indicative of hard scattering centers in the medium. Similar distributions in PbPb and pp collisions would suggest that the energy of the probes is not high enough to resolve the expected scattering centers in the QGP. This observable is normalized to the number of photon+jet pairs.

5.5.2 Energy Ratio, $x_{J\gamma}$

$x_{J\gamma}$ is the ratio of jet energy to photon energy, $x_{J\gamma} = \frac{p_T^{Jet}}{p_T^{\gamma}}$. At tree level due to momentum conservation, this should be a delta function at $x_{J\gamma} = 1$, but the distribution is smeared out by ISR, FSR, and other multi-loop processes in addition to finite energy resolution of jets. Additionally, because of the kinematic cut on jets at 30 GeV/c, the distribution is deformed when $x_{J\gamma} < 30/min(p_T^{\gamma})$ in each p_{T}^{γ} bin. Below this threshold, photons which may have a jet with p_{T} below 30 GeV/c cannot be included in the distributions, and this changes the shape of the plotted distribution below this point. The bins with the highest p_{T}^{γ} are the least deformed by this cut. See Figure 5-4 for a generator-level plot of $x_{J\gamma}$. Energy loss of jets in the medium would cause a shift of the distribution of $x_{J\gamma}$ to lower values, potentially underneath the kinematic cut. This observable is normalized to the number of photons (not photon+jet pairs).

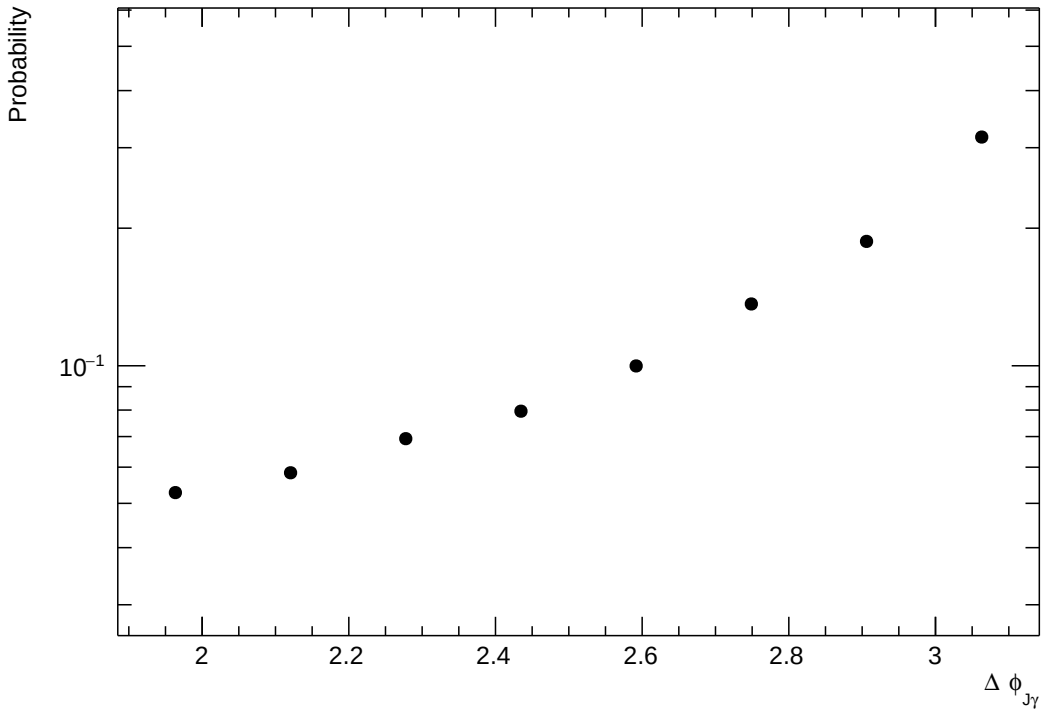

Figure 5-3: A PYTHIA generator-level plot of $\Delta\phi_{J\gamma}$, using cuts of $p_{\mathrm{T}}^{\gamma} > 40$ GeV/c and $p_{\mathrm{T}}^{\mathrm{Jet}} > 30$ GeV/c.

5.5.3 Count of Associated Jets, $R_{J\gamma}$

Because of the kinematic cut on $p_{\mathrm{T}}^{\mathrm{Jet}}$, an additional observable, the average number of jets per photon, $R_{J\gamma}$, is shown. This is equal to the integral of the $x_{J\gamma}$ distributions. If interactions with the medium cause the partons to lose enough energy that the resultant jets have p_{T} less than 30 GeV/c, we would expect to see $R_{J\gamma}$ in PbPb be less than in pp collisions.

5.5.4 Jet Spectra and their ratio, $\mathrm{I_{AA}}$

Looking directly the associated jet spectra can also teach us about the interaction. Because of the photon requirement in the event, the associated jet spectra is less steeply-falling than an inclusive spectra measurement, and a ratio between the associated spectra in PbPb and pp can be informative. This ratio is referred to as $\mathrm{I_{AA}}$,

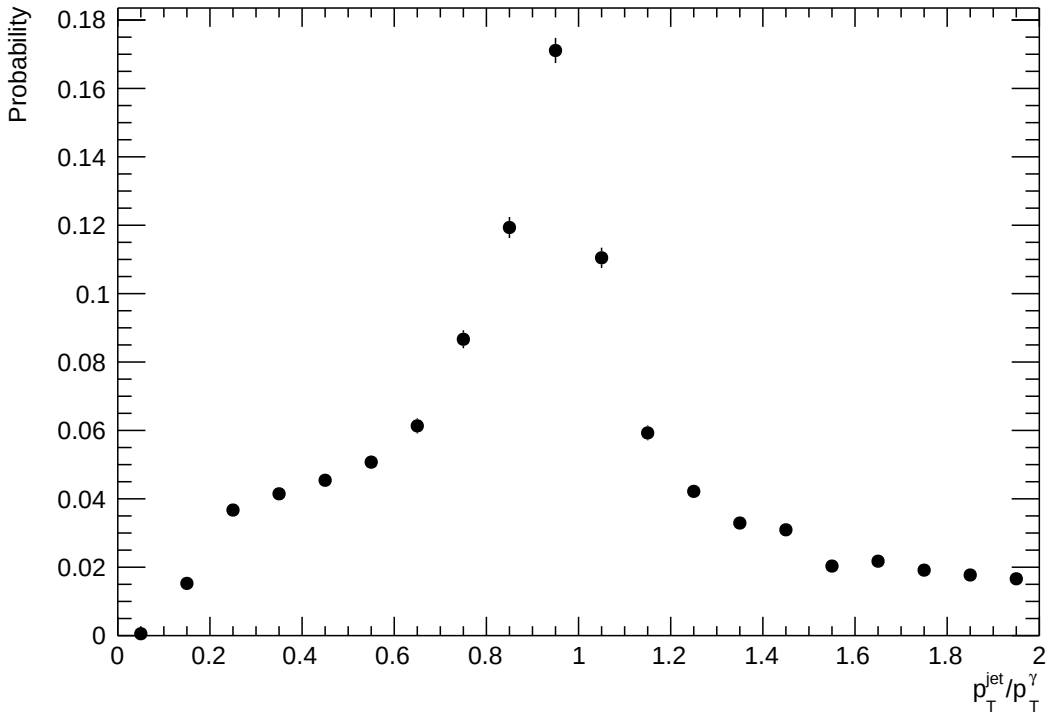

Figure 5-4: A PYTHIA generator-level plot of $x_{J\gamma}$, using cuts of $p_{\mathrm{T}}^{\gamma} > 40$ GeV/c and $p_{\mathrm{T}}^{\mathrm{Jet}} > 30$ GeV/c.

and energy loss should cause a suppression of $\mathrm{I_{AA}}$ at high $p_{\mathrm{T},jet}$ and potentially a matching enhancement at low $p_{\mathrm{T},jet}$ if the kinematic cuts are low enough.

5.6 Systematic Uncertainties

In addition to the statistical uncertainty present in the measurement, there are systematic sources of uncertainty based on our ability to faithfully reconstruct incident particles and categorize those reconstructed particles.

The systematic uncertainty can be divided into the following components

1. Photon systematic uncertainty
   (a) Photon purity
   (b) Photon isolation condition

(c) Photon energy scale

(d) Electron contamination

2. Jet systematic uncertainty

(a) Jet energy scale

(b) Jet energy resolution

For each observable, the general procedure to study systematic uncertainties is to take the difference between the observable with and without a systematic variation which is carefully chosen to represent our belief in the accuracy of our reconstruction. Calculating ratios is avoided in order not to suffer divergences that result from bins with very few entries. In particular, for a systematic variation sys_j the corresponding uncertainty will be calculated as

$$\sigma_j = N^{\text{Nominal}} - N_j^{\text{sys}}, \tag{5.2}$$

where N_j^{sys} is an observable after the systematic variation and $N^{Nominal}$ is the nominal observable. The total uncertainty is calculated by uncorrelated error propagation:

$$\sigma = \sqrt{\sum_j \sigma_j^2}. \tag{5.3}$$

To avoid conflating statistical uncertainties with those from systematic sources, a polynomial fit is made on the residual distribution defined in Eq. 5.2.

Each source of systematic uncertainty which was considered is detailed below.

5.6.1 Systematic Uncertainty from Photon Reconstruction and Purity

In this subsection, the systematic uncertainties due to photon reconstruction are discussed. We first estimate the uncertainty of each step in the photon analysis, such as the efficiency of isolated photon selection, the photon purity, the supercluster

energy correction, the isolation criteria, and the electron contamination. Then, the systematic uncertainties of the observables due to each item are discussed.

Systematic Uncertainty of purity measurement

The systematic uncertainty of the photon purity can be considered as uncertainty on the signal template from Monte-Carlo and uncertainty on the background template from data.

1. Signal template displacement

   By comparing the $\sigma_{\eta\eta}$ distributions of electrons in a Z→ee sample with Monte-Carlo the signal template mean and width is seen to match well between Data and Monte-Carlo. Therefore no significant uncertainty is assigned to the signal template for this analysis.

2. Background template uncertainties

   The choice of isolation sideband affects the extracted purity values. If the sideband is too close to the signal region ($sumIso < 1$ GeV) then the background template is not purely background. If the sideband is too far from the signal region the isolation has a correlation with the shower shape which means the shower shape is not representative of the background in the signal region. The choice of sideband cut was varied from 5-10 GeV ("tight" sideband), to 10-20 GeV (nominal sideband), to 20-30 GeV ("loose" sideband). The deviation from nominal purity value for each of the two variations was propagated through the analysis and the variation of the observables is quoted as the systematic uncertainty.

3. Purity fitting method test in Monte-Carlo

   Signal(AllQCDPhotons) and background(EmEnrichedDijet) Monte-Carlo are merged in a precise fraction and used as input to the purity calculation to confirm the purity fitting method. The fraction of signals in the merged Monte-

Carlo was compared to the purity from the fitting method and it matches within 6%. Figure 5-5 shows several bins where this cross-check was performed.

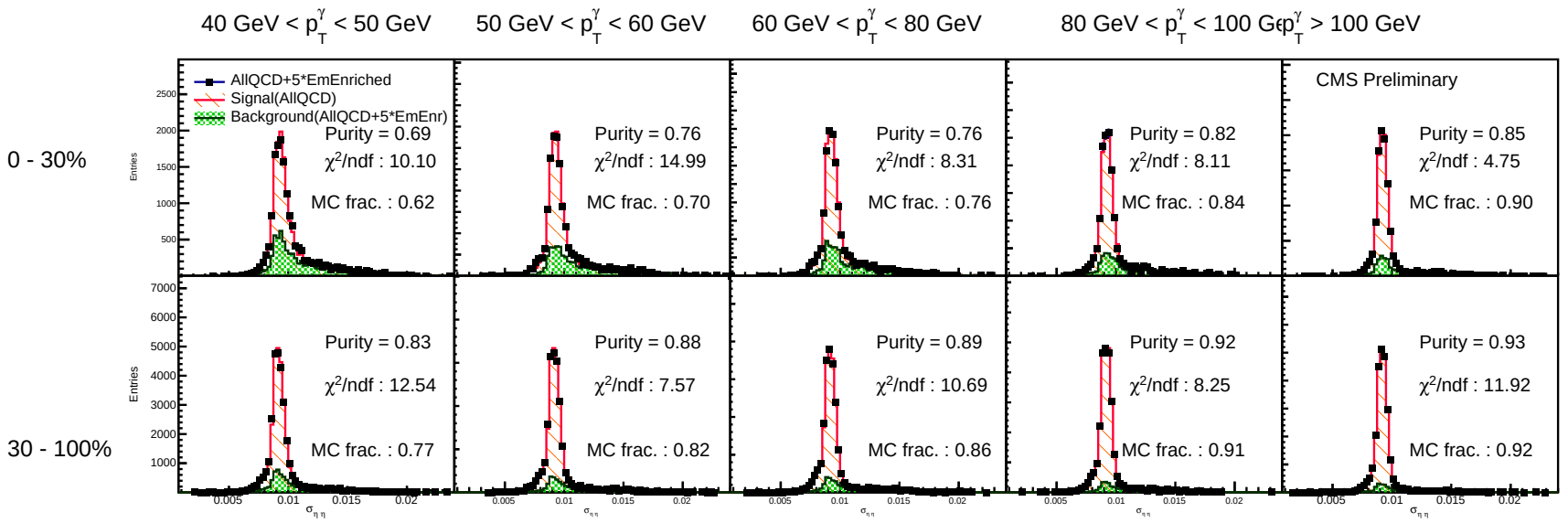

Figure 5-5: Comparison of the known fraction of signal in the merged Monte-Carlo sample with the purity calculated using the template fitting method for several Centrality and p_T^γ bins. The template fitting method matches the known purity within 6%.

Systematic Uncertainty from electron contamination

In spite of the rejection of electron candidates using the tracker (Section 5.1.2), some fraction of electrons are not rejected due to electron reconstruction inefficiency.

The investigation of systematic uncertainty made by electron contamination was carried out by turning off electron rejection and then comparing the final results. In Monte-Carlo, the electron rejection algorithm reduced the fraction of electrons in the signal sample from 5.79% to 2.1%. The variation between using the electron rejection algorithm and not in data, scaled by the remaining fraction left in Monte-Carlo, was quoted as the systematic uncertainty. As a cross check, the electron rejection algorithm rejected 3.76% of the signal sample, consistent with the fraction rejected in Monte-Carlo.

Systematic Uncertainty of the isolation requirement

It is important to have a consistent definition of isolated photons at both the reconstruction level and generator level in order to compare our results to theory. However, due to the resolution of the detector, the selection of isolated photons at reconstruction level is not identical to that at generator level.

In particular there are non-isolated photons at generator level (GenIso$>$ 5 GeV) which are included in the selection of isolated photons at reconstruction level (SumIso$<$ 1 GeV). According to Monte-Carlo simulation, the fraction of the non-isolated photons were estimated to be under 5% for PbPb events and less for pp.

We want to estimate the size of this effect on the final physical observable. Using PYTHIA and PYTHI+HYDJET Monte-Carlo samples, we checked how much the final results differ by choosing isolation criteria (1) at generator level and (2) at reconstruction level and quoted their deviations as the systematic uncertainty.

Systematic Uncertainty by photon energy scale

In this analysis, a photon energy correction due to the UE contribution is obtained from Z$\rightarrow$ee PYTHIA+HYDJET, see Section 3.1.5. After this correction is applied, a

residual difference between the Data and Monte-Carlo samples was observed, and this difference (quantified in Table. 5.3) was propagated to the observables. The variation between not applying and applying this additional correction is quoted as the systematic uncertainty of the photon energy scale.

	0-30%	30-100%
Monte-Carlo	90.946 GeV	90.949 GeV
Data	90.001 GeV	90.648 GeV

Table 5.3: The mean of the Z mass distribution after UE correction compared between Data and Monte-Carlo

5.6.2 Systematic Uncertainty from Jet Reconstruction

The systematic uncertainty from the jet reconstruction are divided into the jet energy scale and jet energy resolution.

Systematic Uncertainty from Jet Energy Scale

The absolute jet energy scale uncertainty of the CMS detector is not a flat function of the jet p_T, but instead exhibits a minimum for $30\,\mathrm{GeV}/c < p_\mathrm{T} < 200\,\mathrm{GeV}/c$. In this thesis, the kinematic range of jets is well within this region, as opposed to an inclusive $\sqrt{s} = 7\,\mathrm{TeV}$ measurement. The restriction to the barrel and end cap region further prevents us sampling the region with larger jet energy scale systematics. We study jet energy scale uncertainty by varying jet p_T by 2% and 4% in pp and PbPb collisions respectively.

Systematic Uncertainty from the Jet energy resolution

Energy resolution in p+p collisions in the CMS detector is a well studied concept, and it constitutes the baseline of understanding energy resolution in Pb+Pb collisions. It is assumed that any effect in p+p would be present in the Pb+Pb collisions. However, a greater contribution comes from the fluctuations of the underlying event. These fluctuations are studied by using two methods: random cone and embedding

procedures. These studies showed that $p_{\mathrm{T}}^{\mathrm{Jet}}$ resolution could be up to 15% worse in data samples than in Monte-Carlo. The uncertainty due to this effect was calculated by applying an additional 15% Gaussian smearing factor to $p_{\mathrm{T}}^{\mathrm{Jet}}$; each jet energy was multiplied by a random value sampled from a Guassian distribution centered at 1 with a width of 15%. The variation in observables after this procedure was quoted as the systematic uncertainty.

Total Systematic Uncertainty

The total systematic uncertainty was calculated by summing the quadratures of the uncertainties from each source: (a) photon purity (b) photon energy scale (c) electron contamination (d) photon isolation criteria (e) jet energy resolution (f) jet energy scale.

Systematic Uncertainty	$\langle x_{J\gamma} \rangle$ $p_{\mathrm{T}}^{\gamma} > 60$ GeV	$\langle x_{J\gamma} \rangle$ 0-30%	$\langle x_{J\gamma} \rangle$ 30-100%	$\sigma(\Delta\phi_{J\gamma})$ $p_{\mathrm{T}}^{\gamma} > 60$ GeV
Photon Purity	2.9%	3.3%	1.9%	1.6%
Photon Energy Scale	0.7%	0.6%	0.5%	2.4%
Electron Contamination	<0.5%	<0.5%	<0.5%	0.9%
Photon Isolation	0.9%	0.7%	0.6%	3.6%
Jet Energy Resolution	1.1%	1.6%	1.0%	2.1%
Jet Energy Scale	3.3%	3.2%	3.2%	2.5%

Systematic Uncertainty	$R_{J\gamma}$ $p_{\mathrm{T}}^{\gamma} > 60$ GeV	$R_{J\gamma}$ 0-30%	$R_{J\gamma}$ 30-100%
Photon Purity	1.3%	3.3%	2.5%
Photon Energy Scale	0.6%	<0.5%	0.8%
Electron Contamination	0.6%	<0.5%	0.6%
Photon Isolation	0.7%	1.7%	0.8%
Jet Energy Resolution	2.7%	4.0%	2.9%
Jet Energy Scale	5.3%	6.7%	5.6%

Table 5.4: Summary of the average systematic uncertainties. Columns which do not specify the p_{T}^{γ} cut have a cut of $p_{\mathrm{T}}^{\gamma} > 40$. Columns which do not specify the centrality bin are centrality-inclusive.

Chapter 6

Results

6.1 Experimental Comparison of pp and PbPb Collisions

6.1.1 Photon + jet azimuthal correlation

Possible medium modification of the back-to-back photon and recoiling jet aligment can be studied by comparing the relative azimuthal angle ($\Delta\phi_{J\gamma}$) distributions in pp and PbPb collisions. The shape of the $\Delta\phi_{J\gamma}$ distribution in PbPb collisions is studied in bins of leading photon p_{T} and two event centrality intervals, and it is shown in Fig. 6-1. Within the quoted statistical uncertainty, the results in pp and PbPb collisions are consistent with each other.

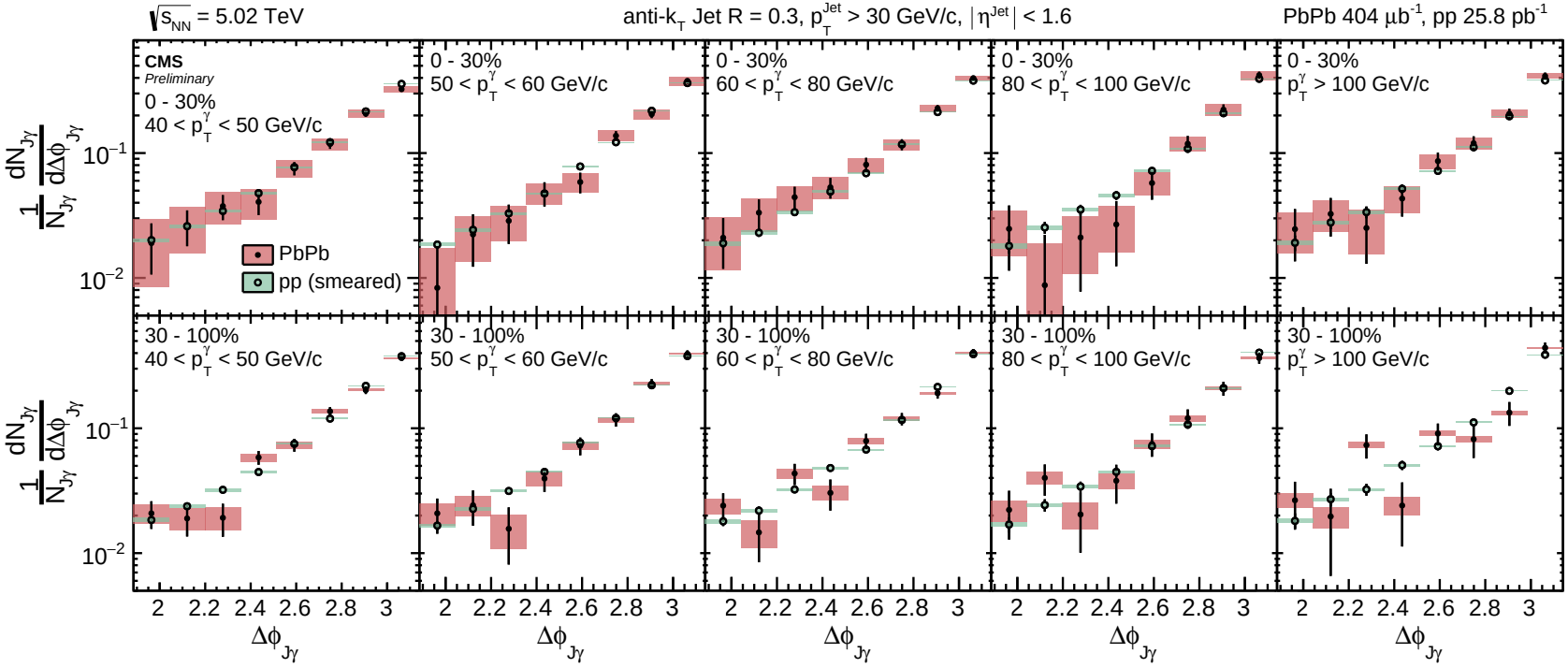

Figure 6-1: Azimuthal correlation of photons and jets in each p_{T}^{γ} bin (from left to right) for central PbPb (top) and peripheral PbPb (bottom) after mixed event background subtraction. The correlation is shown on a logarithmic scale and its range is restricted to $\Delta\phi_{J\gamma} > \frac{3\pi}{5}$. The PbPb data is compared to smeared pp data. The lines through the points represent the statistical uncertainty while the shaded boxes represent the systematic uncertainty.

6.1.2 Photon + jet transverse momentum imbalance

The asymmetry ratio $x_{J\gamma} = p_{\mathrm{T}}^{\mathrm{Jet}}/p_{\mathrm{T}}^{\gamma}$ is used to quantify the photon + jet transverse momentum imbalance. In addition to the photon and jet selections used in the $\Delta\phi_{J\gamma}$ study, a strict $\Delta\phi_{J\gamma} > \frac{7}{8}\pi$ selection is applied to suppress contribution from background jets as well as photon+2-jets events. Figure 6-2 shows the normalized $x_{J\gamma}$ distributions for different centrality and p_{T}^{γ} regions in pp and PbPb collisions. The pp data is smeared to account for the jet resolution difference in pp and PbPb collisions when compared with PbPb data. A significant modification with respect to the smeared pp reference is observed in 0–30% PbPb collisions. The mean of the $x_{J\gamma}$ as a function of photon p_{T} is shown in Fig. 6-3. In the region $p_{\mathrm{T}}^{\gamma} < 60$ GeV/c, the $\langle x_{J\gamma} \rangle$ in smeared pp and PbPb collisions are consistent within the quoted uncertainty.

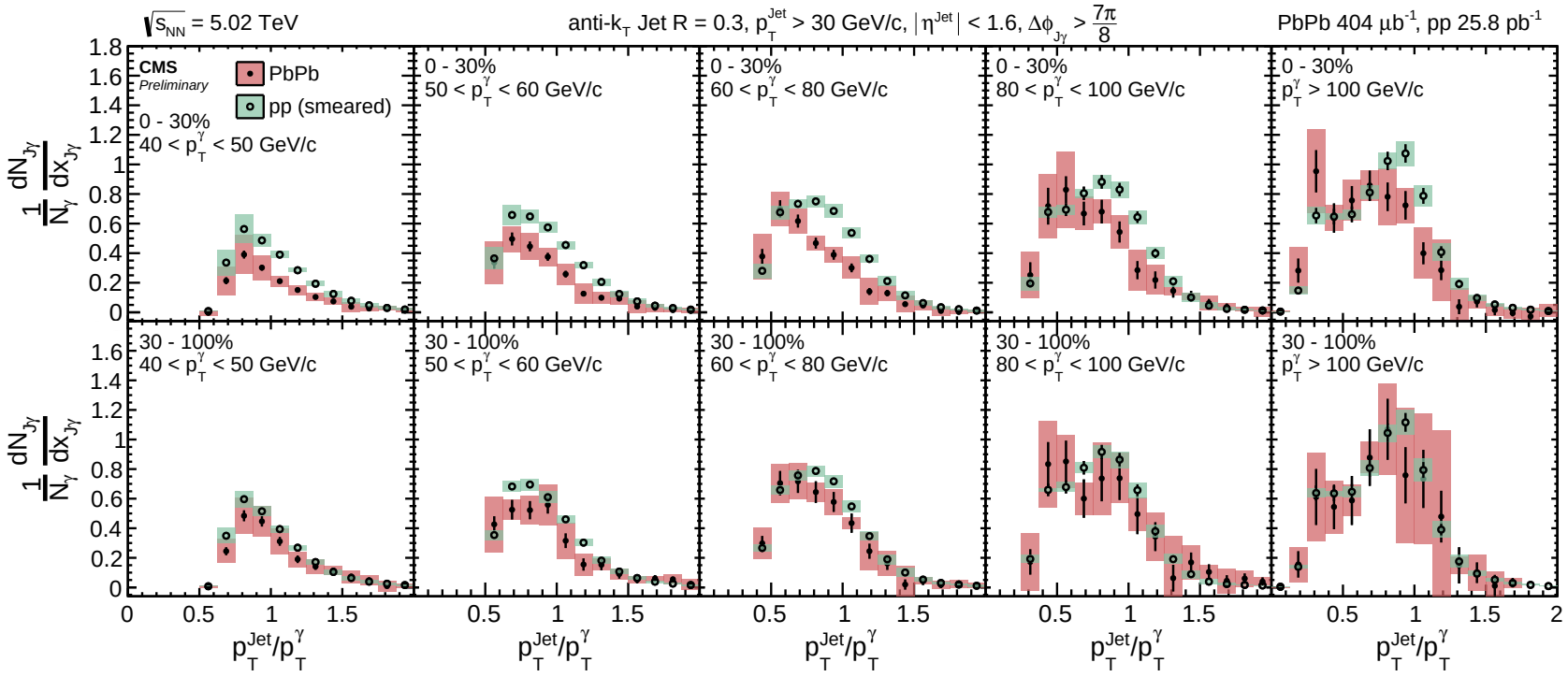

Figure 6-2: Distribution of $x_{J\gamma} = p_{\mathrm{T}}^{\mathrm{Jet}}/p_{\mathrm{T}}^{\gamma}$ in each p_{T}^{γ} bin (from left to right) for central PbPb (top) and peripheral PbPb (bottom). The PbPb data are compared to smeared pp data. The lines through the points represent the statistical uncertainty while the shaded boxes represent the systematic uncertainty.

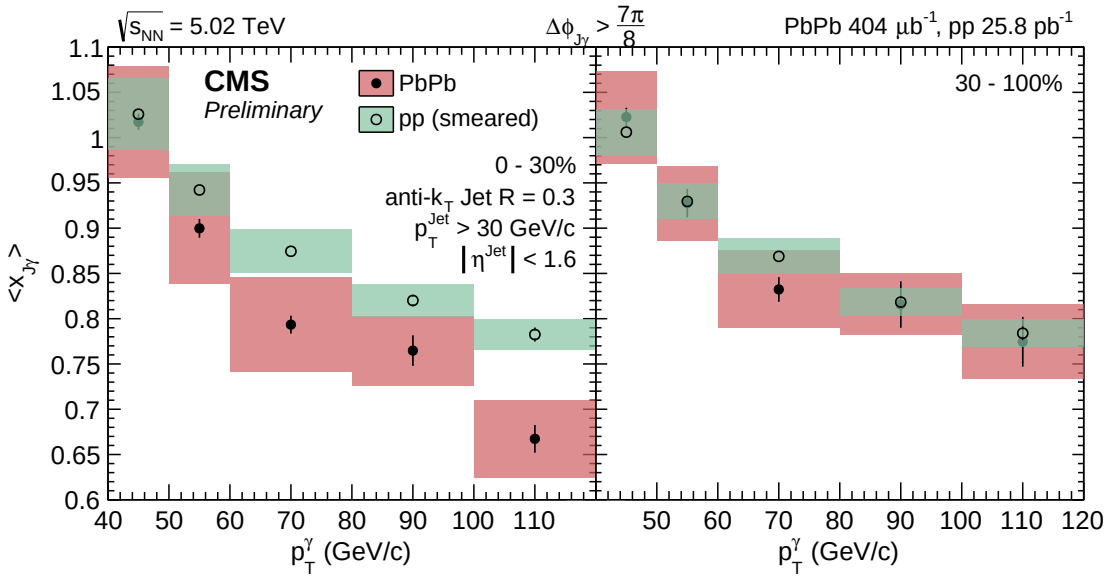

Figure 6-3: Average jet over photon transverse momentum ratio ($\langle x_{J\gamma} \rangle$) of the recoiled jets in (left) smeared pp and central PbPb, and (right) smeared pp and peripheral PbPb. The pp results are smeared by the relative jet energy resolution in order to account for the underlying event fluctuations when compared to PbPb data. The lines through the points represent the statistical uncertainty while the shaded boxes represent the systematic uncertainty.

6.1.3 Average Number of Associated Jets per Photon

With a jet p_{T} threshold of 30 GeV/c, the average energy imbalance of the selected photon + jet pairs does not constitute a full picture. There are photon + jet pairs that do not contribute to the $\langle x_{J\gamma} \rangle$ because the associated jets fall below this threshold. To quantify the effect, the average number of associated jets per photon passing the analysis selection ($R_{J\gamma}$) is shown in Fig. 6-4. In the 0–30% central PbPb collisions, the value of $R_{J\gamma}$ is found to be lower than the smeared pp data in all leading photon p_{T} bins.

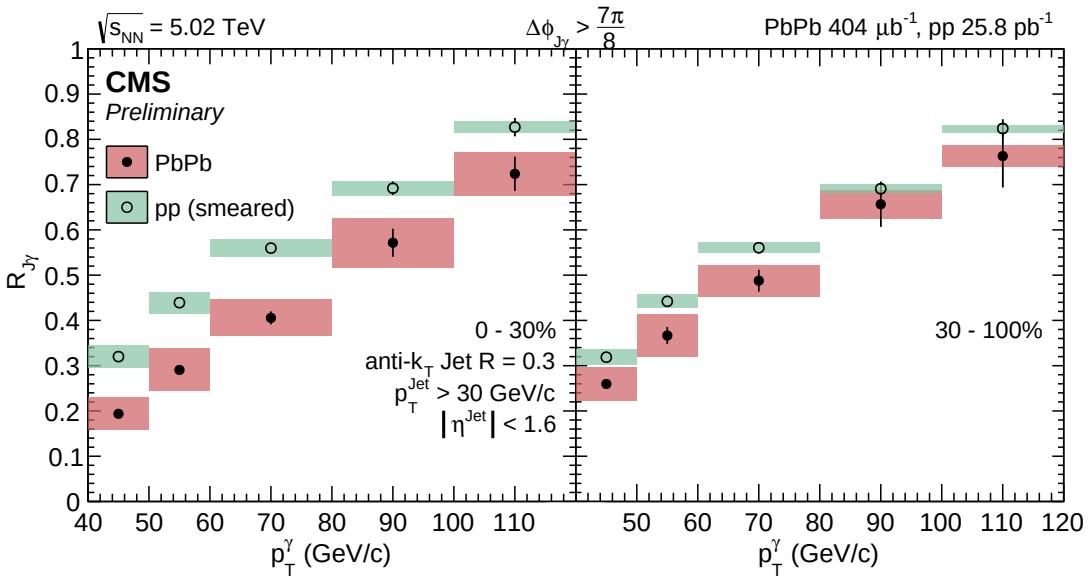

Figure 6-4: Average number of associated jets per photon ($R_{J\gamma}$) as a function of leading photon p_{T} in (left) smeared pp and central PbPb, and (right) smeared pp and peripheral PbPb. The jet energy in the pp data is smeared by the relative jet energy resolution in order to account for the underlying event fluctuations when compared to PbPb data. The lines through the points represent the statistical uncertainty while the shaded boxes represent the systematic uncertainty.

6.1.4 Jet yield ratio

In order to illustrate the medium modification of the associated jet p_{T} spectra, the ratio of the associated jet yields in PbPb and smeared pp events, $\mathrm{I_{AA}}$, is shown in Fig. 6-6. In central PbPb events, the associated yield is suppressed by a factor of two in low p_{T}^{γ} bins. As p_{T}^{γ} increases, an excess of jets appears at low $p_{\mathrm{T}}^{\mathrm{Jet}}$ in central PbPb as the increased phase space at high p_{T}^{γ} allows the quenched jets to remain above the kinematic cuts.

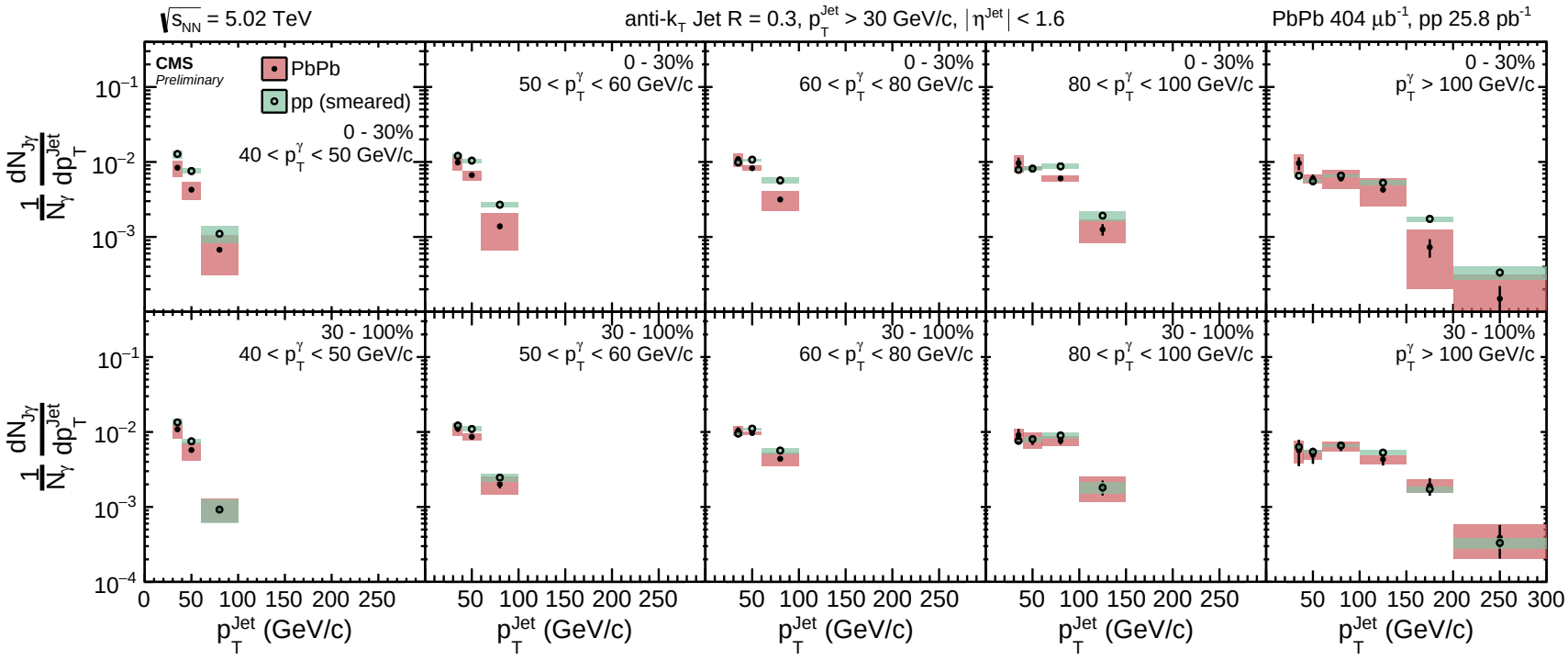

Figure 6-5: The $p_{\mathrm{T}}^{\mathrm{Jet}}$ spectra for PbPb and smeared pp data. The lines through the points represent the statistical uncertainty while the shaded boxes represent the systematic uncertainty.

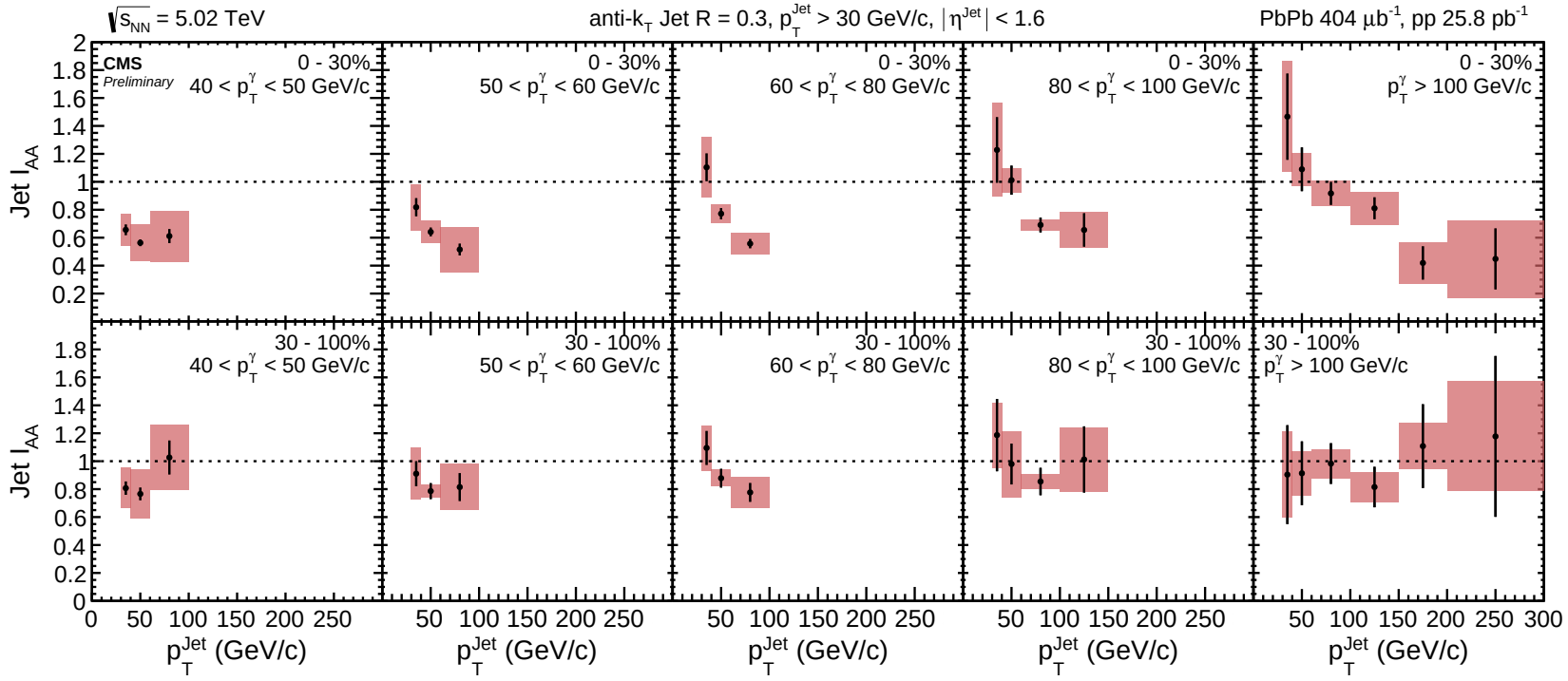

Figure 6-6: Ratio of jet yield in PbPb collisions to smeared pp. In the low p_{T}^{γ} events, the yields in central PbPb events are smaller than in pp for all $p_{\mathrm{T}}^{\mathrm{Jet}}$ bins. As p_{T}^{γ} increases, yields at low $p_{\mathrm{T}}^{\mathrm{Jet}}$ are greater in PbPb than smeared pp. The lines through the points represent the statistical uncertainty while the shaded boxes represent the systematic uncertainty.

6.1.5 Centrality Dependence

The centrality dependence of $x_{J\gamma}$ for PbPb collisions with $p_{\mathrm{T}}^{\gamma} > 60$ GeV/c is shown in Fig. 6-7. When compared to the smeared pp data, the PbPb collision data exhibit a change in shape, shifting the distribution towards lower $x_{J\gamma}$ as the collisions become more central.

The following figures are shown as a function of the average number of participants estimated from a Monte-Carlo Glauber model and weighted by the number of collisions to account for the hard scattering bias within each centrality bin.

To study the centrality evolution of the $\Delta\phi_{J\gamma}$ shape in PbPb collisions, the distributions are fitted to an exponential function:

$$\frac{1}{N_{J\gamma}}\frac{dN_{J\gamma}}{d\Delta\phi_{J\gamma}} = A + Be^{\frac{\Delta\phi-\pi}{\sigma}} \tag{6.1}$$

where A is constant pedestal and σ is the width of the distribution. The fit is restricted to the exponentially falling region $\Delta\phi > 2\pi/3$. The results obtained from PbPb collisions and smeared pp data are consistent with each other as shown in Fig. 6-8.

Figures 6-9 and 6-10 show the results $R_{J\gamma}$ and $\langle x_{J\gamma}\rangle$ in pp and PbPb collisions as a function of event centrality. In central collisions, a reduction in $R_{J\gamma}$ and $\langle x_{J\gamma}\rangle$ is observed in comparison to the pp reference, confirming the observation of away-side jet energy loss.

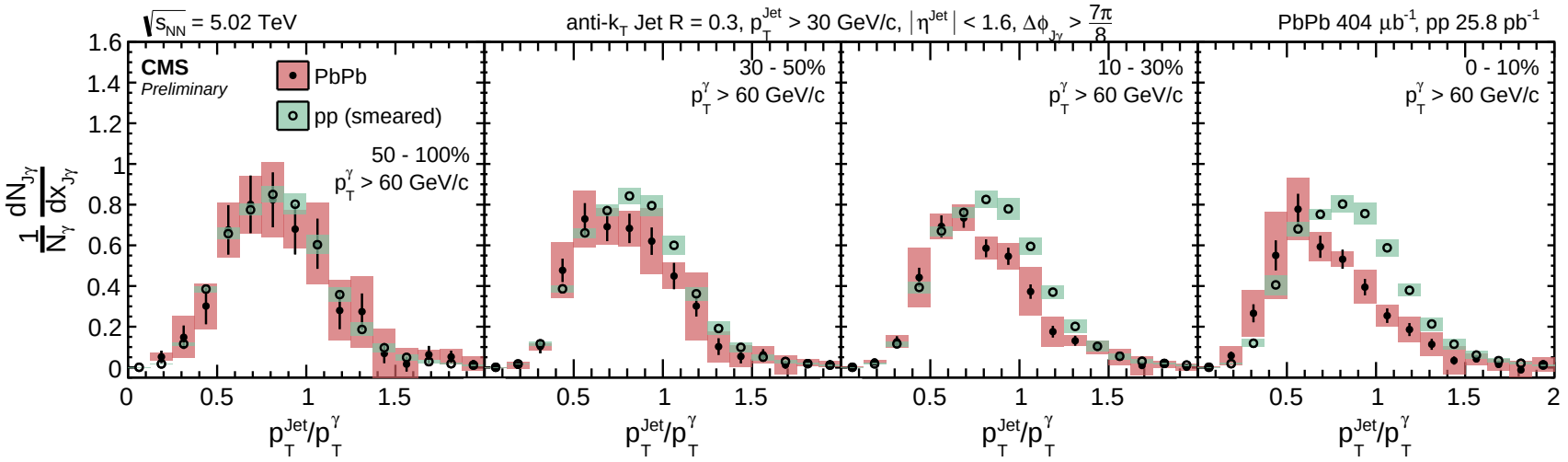

Figure 6-7: Distribution of $x_{J\gamma}$ of photon+jet pairs of pp and PbPb collisions normalized by the number of photon+jet pairs. The momenta of jets in pp are smeared by the relative jet energy resolution to be used as the reference of each centrality bin. The lines through the points represent the statistical uncertainty while the shaded boxes represent the systematic uncertainty.

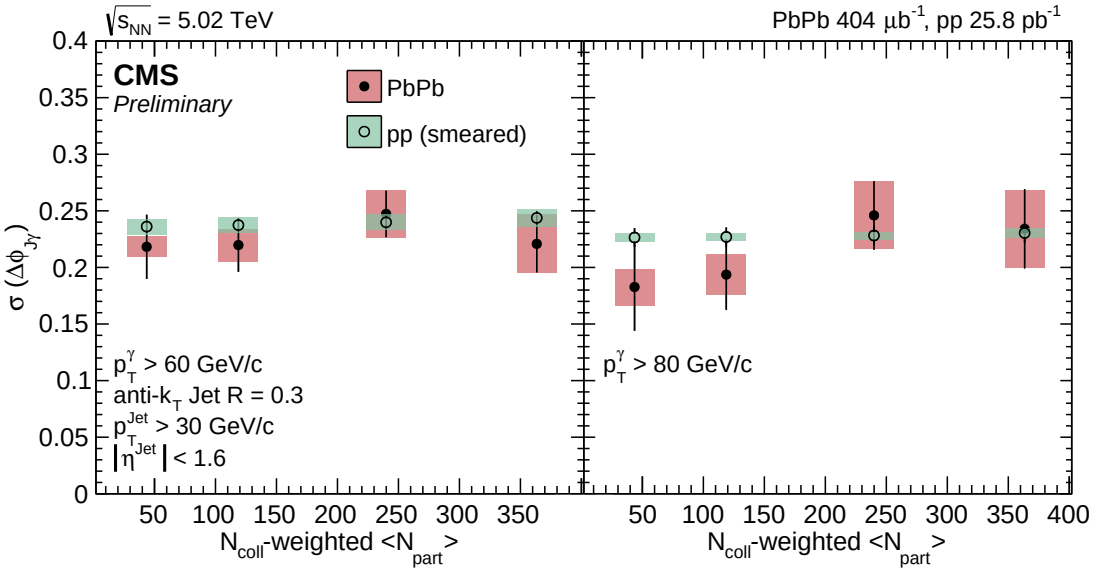

Figure 6-8: Comparison of $\Delta\phi_{J\gamma}$ width in pp and PbPb collisions shown for different $p_{\mathrm{T}}^{\mathrm{Jet}}$ bins as a function of the average number of participants weighted by the number of collisions. The momenta of jets in pp are smeared by the relative jet energy resolution to be used as the reference of each centrality bin. The lines through the points represent the statistical uncertainty while the shaded boxes represent the systematic uncertainty.

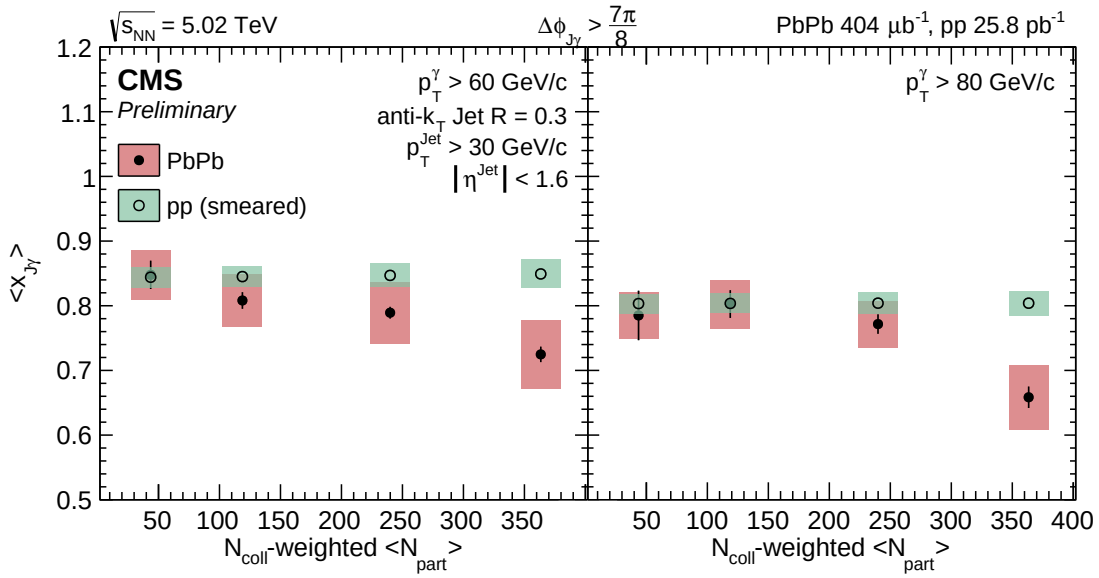

Figure 6-9: Comparison of $\langle x_{J\gamma} \rangle$ in pp and PbPb collisions as a function of the average number of participants weighted by the number of collisions. The momenta of jets in pp are smeared by the relative jet energy resolution to be used as the reference of each centrality bin. The lines through the points represent the statistical uncertainty while the shaded boxes represent the systematic uncertainty.

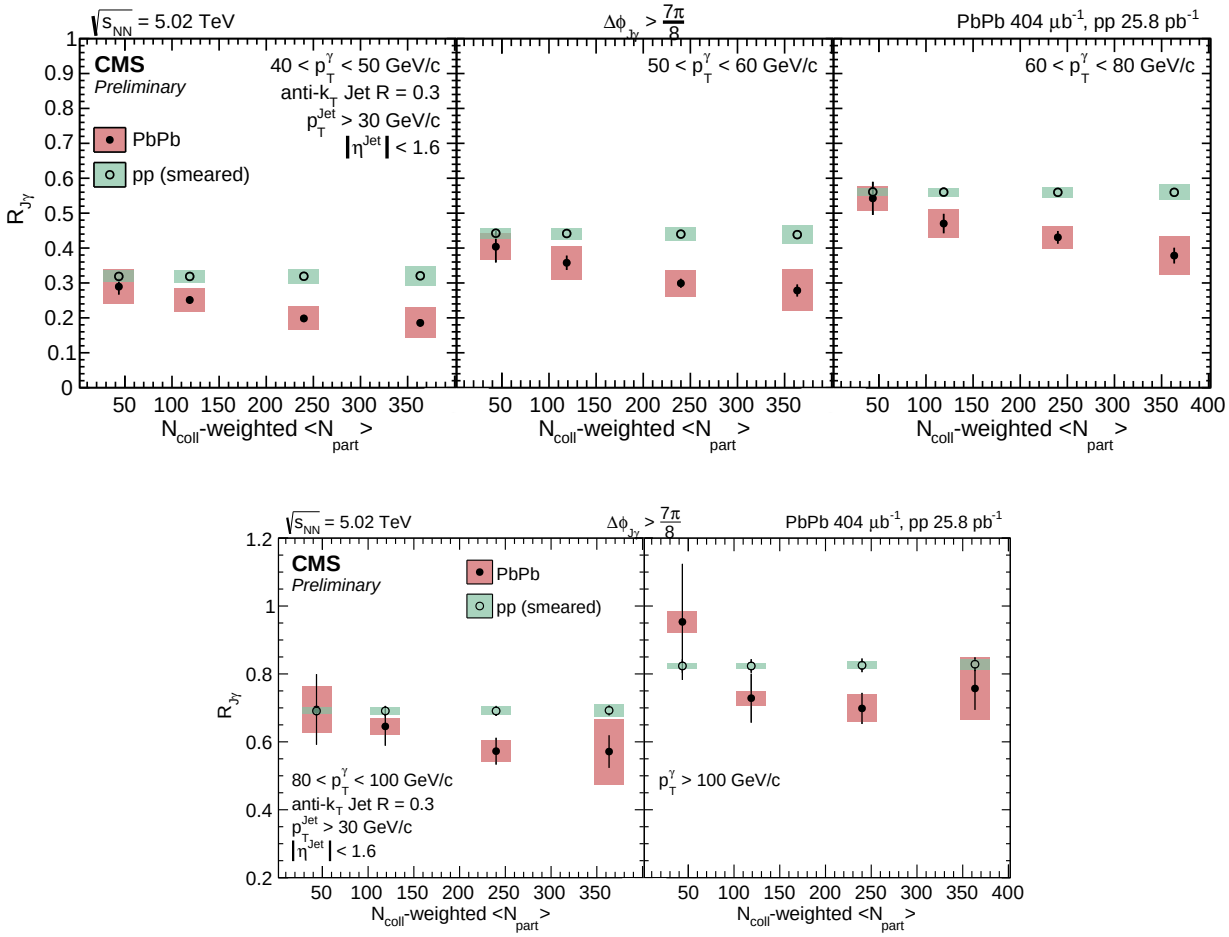

Figure 6-10: Comparison of $R_{J\gamma}$ in pp and PbPb collisions as a function of the average number of participants weighted by the number of collisions. The momenta of jets in pp are smeared by the relative jet energy resolution to be used as the reference of each centrality bin. The lines through the points represent the statistical uncertainty while the shaded boxes represent the systematic uncertainty.

6.2 Theoretical Comparisons of References

We solicited theoretical comparisons from several groups during the analysis and received 3 replies. Korinna Zapp and Raghav Kunnawalkam prepared results for us using their JEWEL Monte-Carlo[40, 41, 42]. Xin-Nian Wang and Tan Luo provided us with calculations using their Linearized Boltzmann Transport (LBT) model[43, 44]. Daniel Pablos provided us with calculations using the Hybrid Model[45, 46, 47, 48]. In all cases, the theorists were **not** presented with the data results before they produced their predictions.

For each comparison to theoretical models, it is important to make sure that the reference used in the experiment (the smeared pp, open circles with green bands in Section 6.1) matches that used by the theoretical groups. If the theoretical references do not agree with the experimental reference it means that there is an issue with how the theoretical groups are performing the analysis and the comparisons to the PbPb results will be meaningless. We show in Section 6.2.1 the comparison of the theoretical references (where available) to the experimental one. In Section 6.2.2 we then show the PbPb data (filled circle with red bands from Section 6.1) compared with the PbPb predictions from each of the groups, where available.

The theorists did not provide all experimental observables in all analysis bins to us, so there are panels which are missing certain comparisons. For example, the Hybrid model only provides comparisons in the 0%-30% bins, without showing the more peripheral bins.

6.2.1 Comparison of References

In general, the Hybrid model has remarkably good agreement with the experimental reference in the bins for which it is available, and all 3 models agree with the experimental reference at high p_{T}^{γ}. At low p_{T}^{γ}, the JEWEL and LBT models show small disagreements that might be attributable to low statistics.

$\Delta\phi_{J\gamma}$

As shown in Fig. 6-11, all theoretical references of $\Delta\phi_{J\gamma}$ agree well with the experimental one at high p_{T}^{γ}. The LBT and JEWEL models have a slightly narrower distribution than the experimental reference at low p_{T}^{γ}.

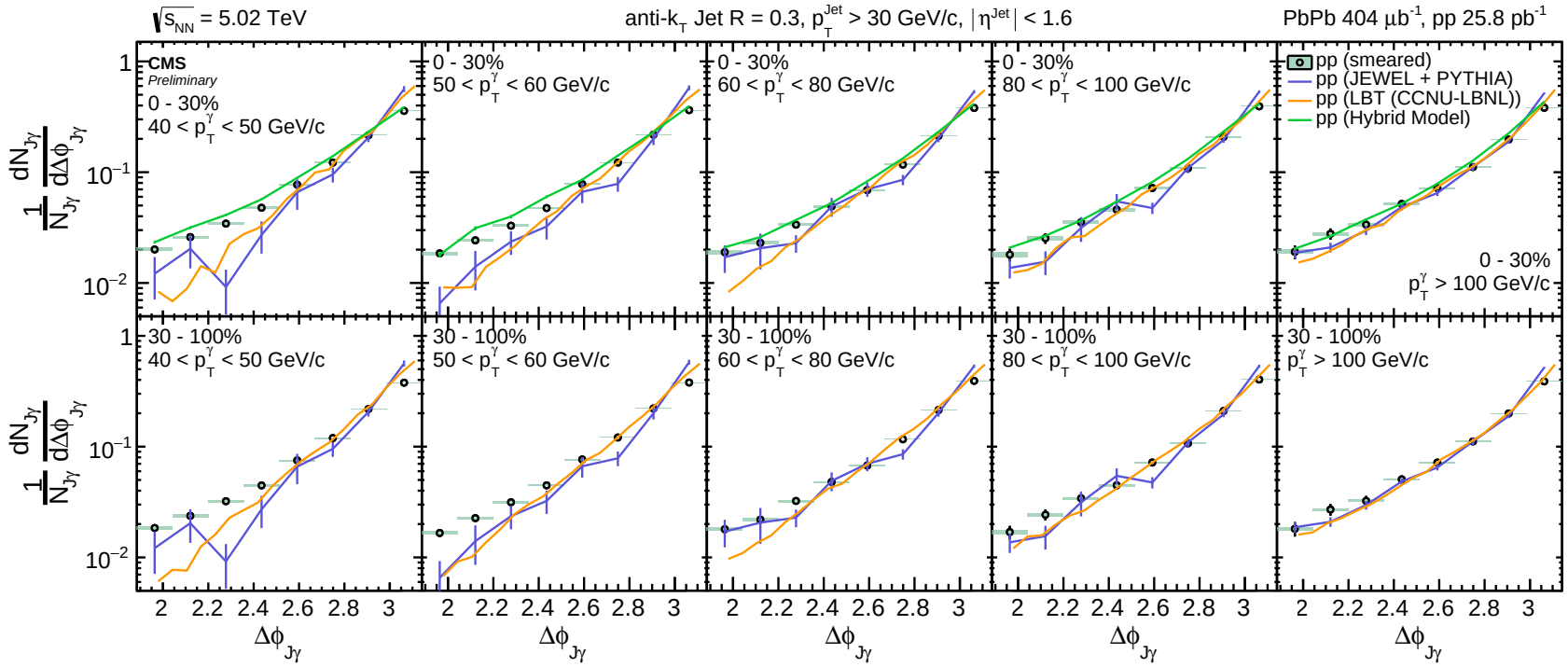

Figure 6-11: Azimuthal correlation of photons and jets in each $p_{\mathrm{T},\gamma}$ bin (from left to right) for pp smeared to match central resolution (top) and pp smeared to match peripheral resolution (bottom). The pp reference is compared to several theoretical predictions. The correlation is shown on a logarithmic scale with the range restricted to $\Delta\phi_{J\gamma} > \frac{3\pi}{5}$.

$x_{J\gamma}$

As shown in Fig. 6-12, all three models agree roughly with the experimental reference. However on close inspection, and also referencing Fig. 6-13, the JEWEL and LBT models under-predict the tail at large $x_{J\gamma}$ and therefore have a lower $\langle x_{J\gamma} \rangle$. The Hybrid model does not have this difference.

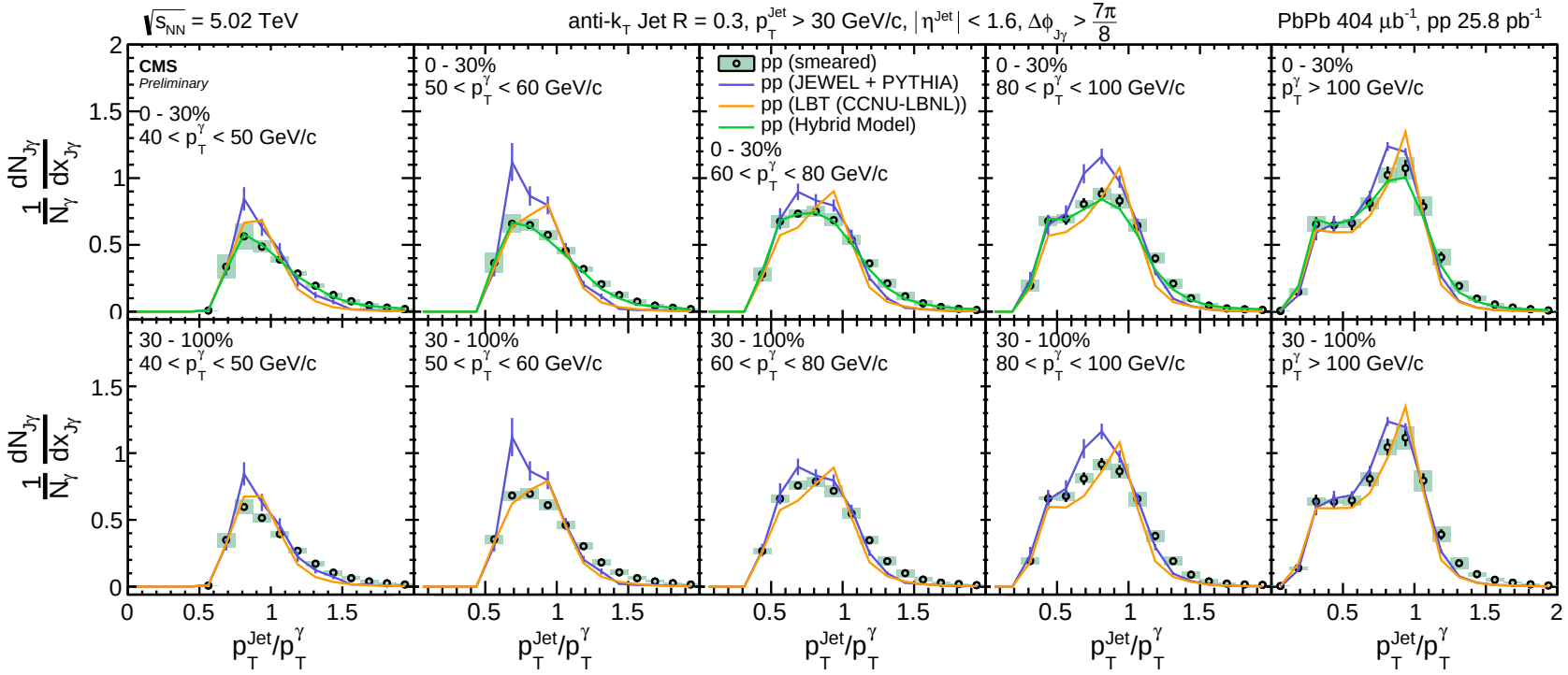

Figure 6-12: Distribution of $x_{J\gamma}$ in each $p_{T,\gamma}$ bin (from left to right) for pp smeared to match central resolution (top) and pp smeared to match peripheral resolution (bottom). The pp reference is compared to several theoretical predictions.

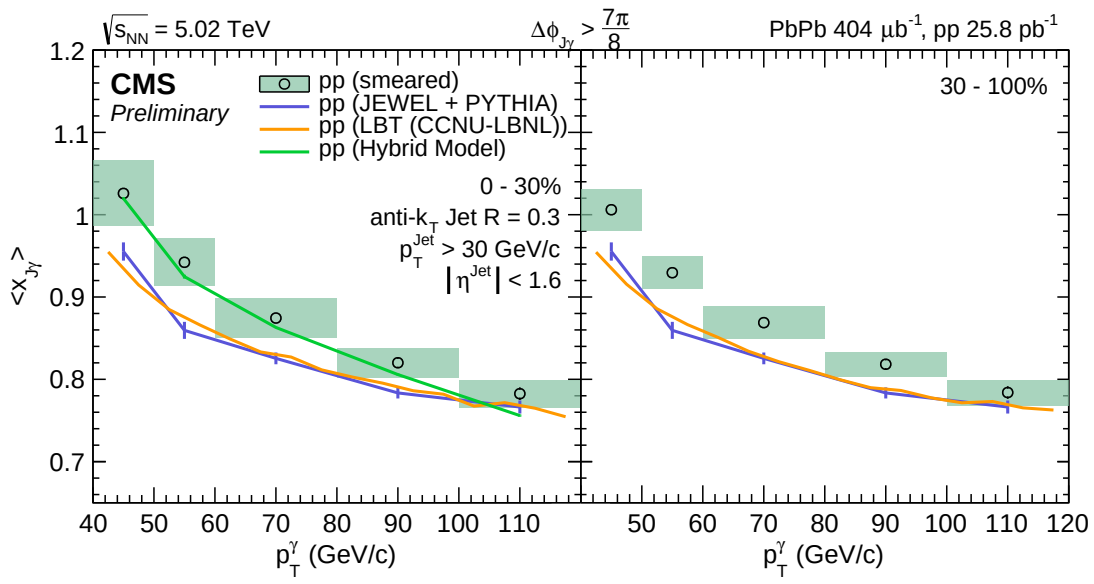

Figure 6-13: Average jet over photon transverse momentum ratio ($\langle x_{J\gamma} \rangle$) of the recoiled jets in (left) pp smeared to match central resolution, and (right) and pp smeared to match peripheral resolution. The pp reference is compared to several theoretical predictions.

$R_{J\gamma}$

In Fig. 6-14, all 3 models under-predict the experimental reference in the largest p_{T}^{γ} bin, but the overall shape and values at lower p_{T}^{γ} agree. The LBT reference underpredicts at all p_{T}^{γ} slightly.

Jet Spectra

The LBT reference matches the associated jet spectra very well, especially the "wobble" caused by the required presence of the high p_{T} photon. The JEWEL reference does a good job at high p_{T}.

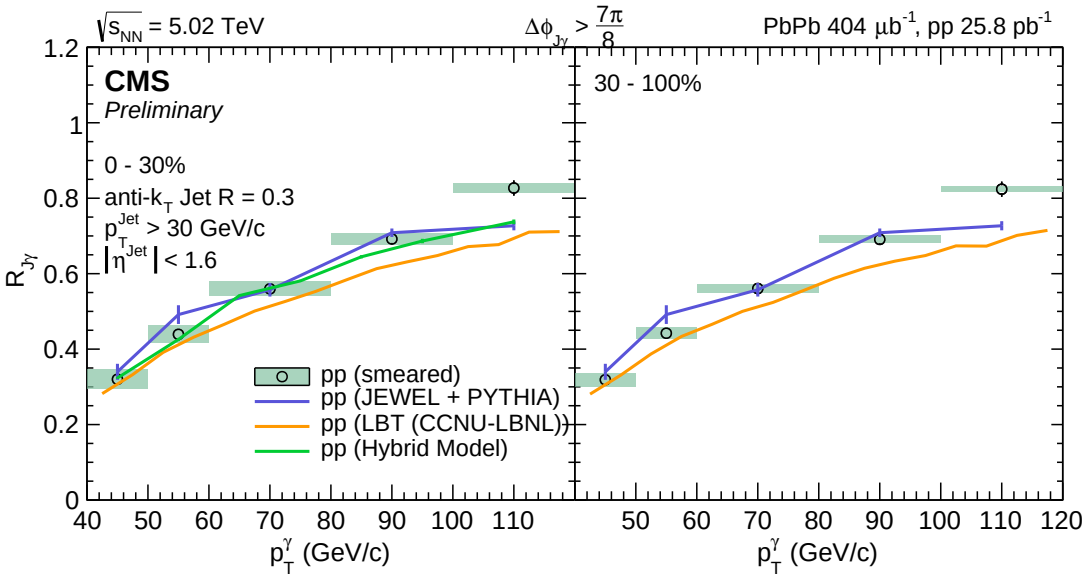

Figure 6-14: Average number of associated jets per photon ($R_{J\gamma}$) as a function of leading photon p_{T} in (left) pp smeared to match central resolution, and (right) and pp smeared to match peripheral resolution. The pp reference is compared to several theoretical predictions.

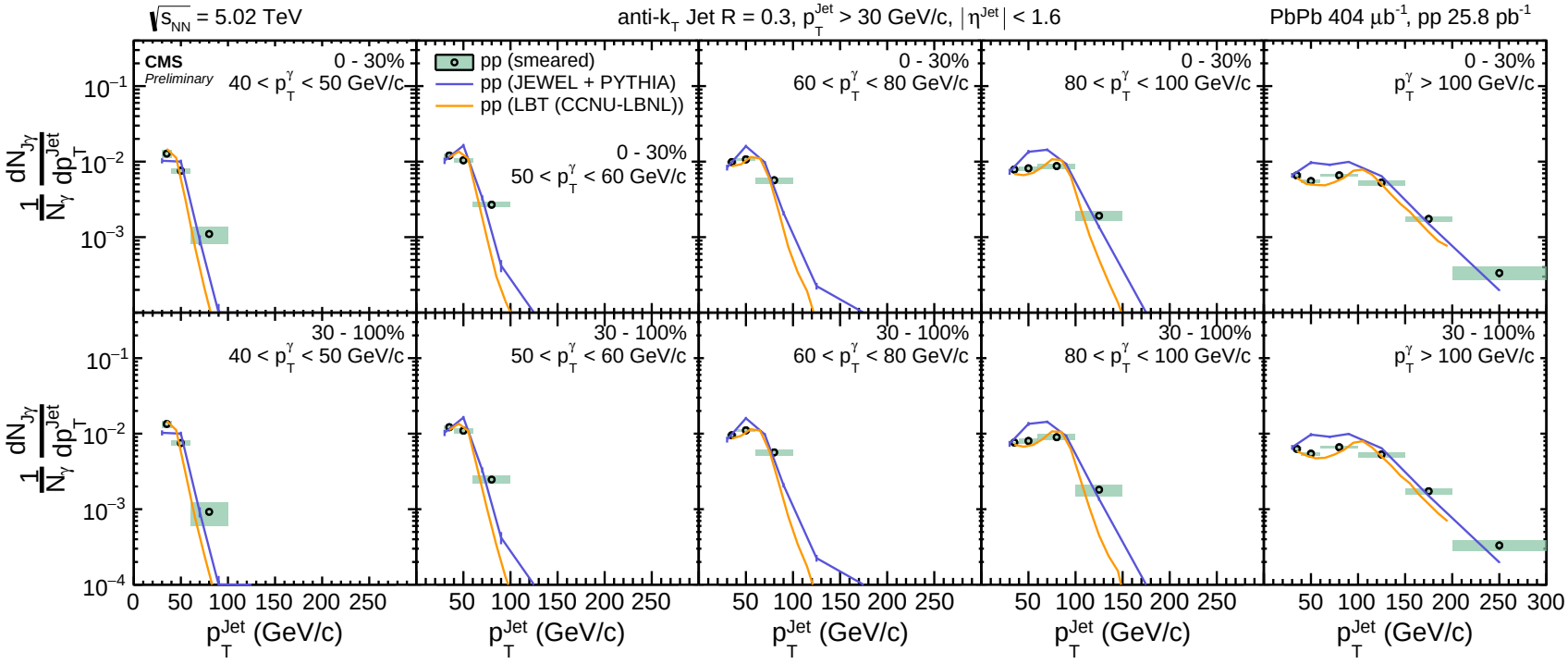

Figure 6-15: The $p_{\mathrm{T}}^{\mathrm{Jet}}$ spectra for pp reference. The pp reference is compared to several theoretical predictions.

Centrality Dependence

For Figs. 6-16 – 6-19, only the JEWEL group provided a comprehensive set of comparisons. The Hybrid model provided certain bins, while the LBT group is absent from these comparisons. $x_{J\gamma}$ in JEWEL is seen again to be under-predicted in the high $x_{J\gamma}$ tail and the mean, and the $\sigma(\Delta\phi_{J\gamma})$ is seen to be narrower than the experimental reference. $R_{J\gamma}$ is overpredicted at low p_{T}^{γ}, crosses over at middle p_{T}^{γ}, and then is under-predicted at high p_{T}^{γ}.

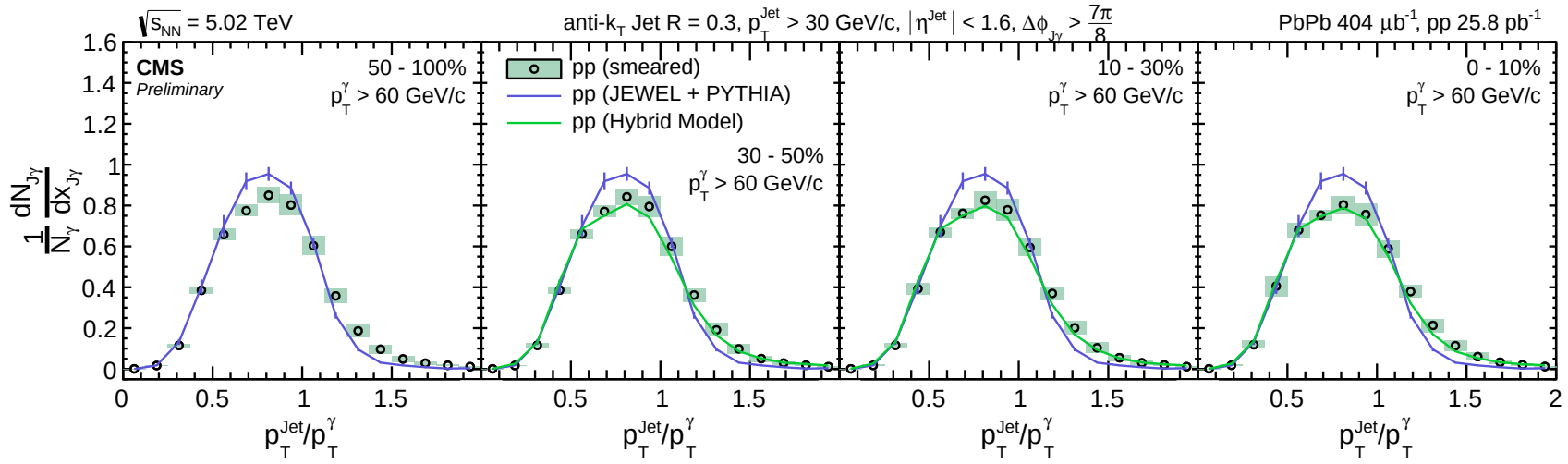

Figure 6-16: Distribution of $x_{J\gamma}$ of photon+jet pairs of pp collisions normalized by the number of photon+jet pairs. The pp reference is compared to several theoretical predictions.

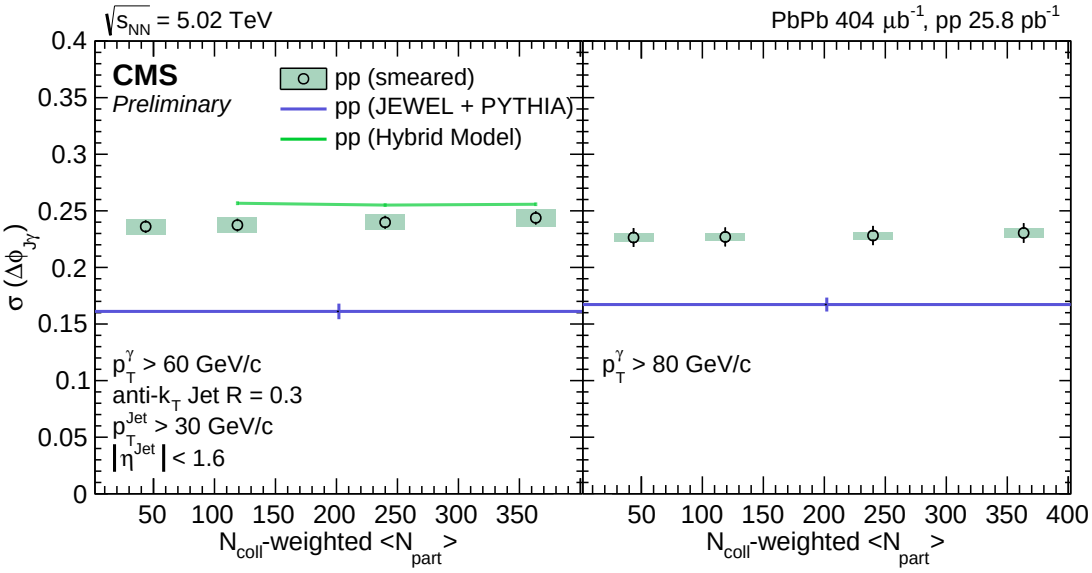

Figure 6-17: Comparison of $\Delta\phi_{J\gamma}$ width in pp collisions shown for different $p_{\mathrm{T}}^{\mathrm{Jet}}$ bins. The pp reference is compared to several theoretical predictions.

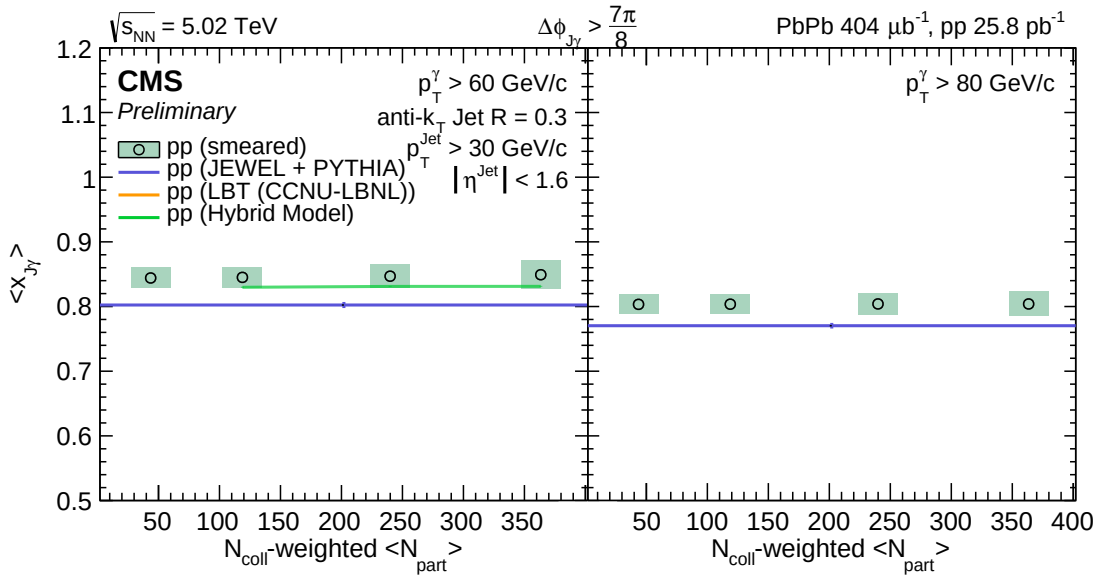

Figure 6-18: Comparison of $\langle x_{J\gamma} \rangle$ in pp collisions. The pp reference is compared to several theoretical predictions.

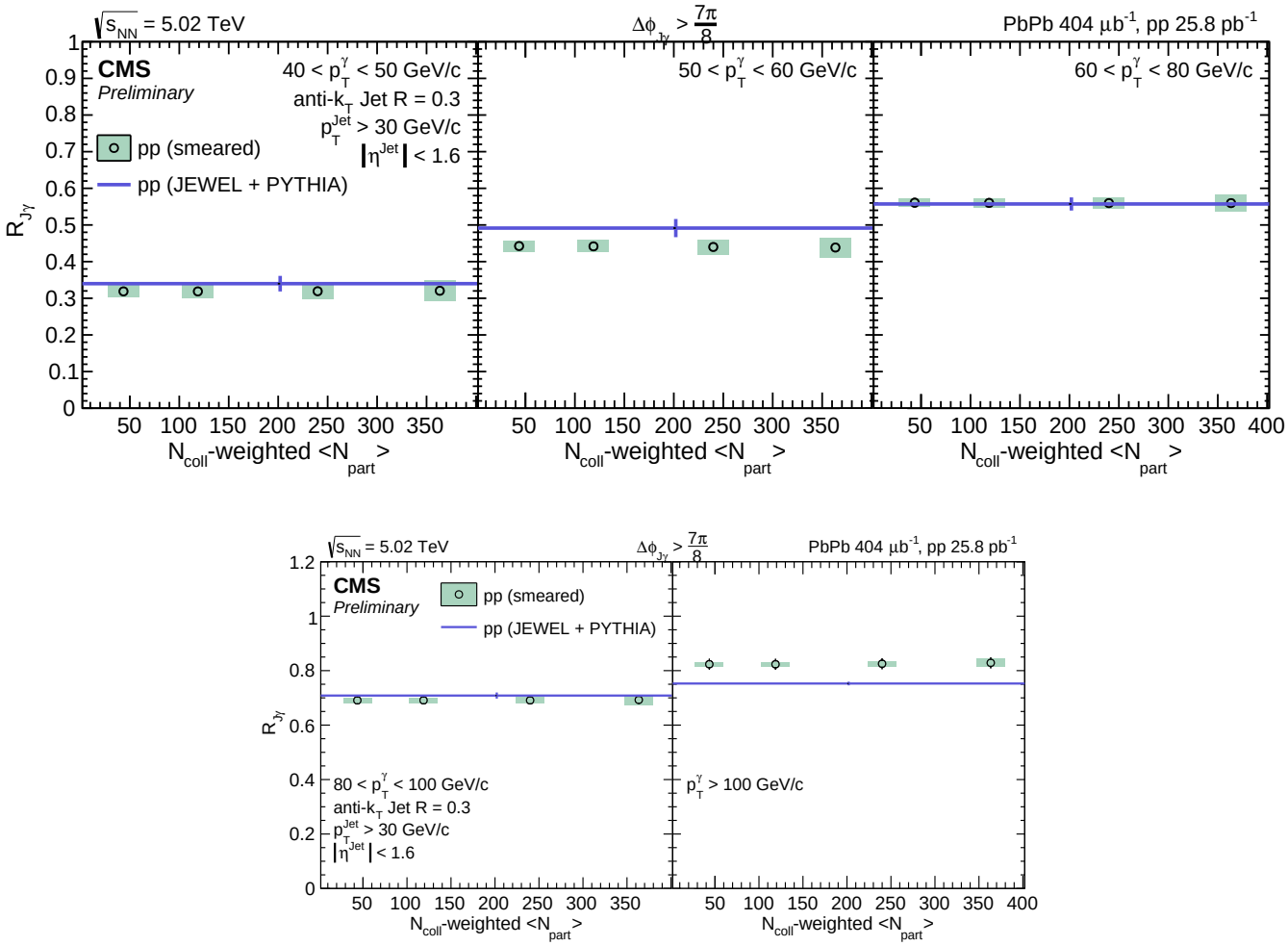

Figure 6-19: Comparison of $R_{J\gamma}$ in pp collisions. The pp reference is compared to several theoretical predictions.

6.2.2 Theoretical Comparisons of PbPb results

The theory predictions of the PbPb results show roughly the same differences as their references to the pp results. In general, the Hybrid model agrees remarkably well with the PbPb results in the bins for which it was provided, while the JEWEL and LBT models have some significant deviations.

$\Delta\phi_{J\gamma}$

Just as the experimental data showed no significant difference between pp and PbPb, none of the theoretical predictions show large deviations from the PbPb result. The Hybrid model performs best, especially at low p_{T}^{γ} where the LBT and JEWEL models show narrower distributions just like in their references.

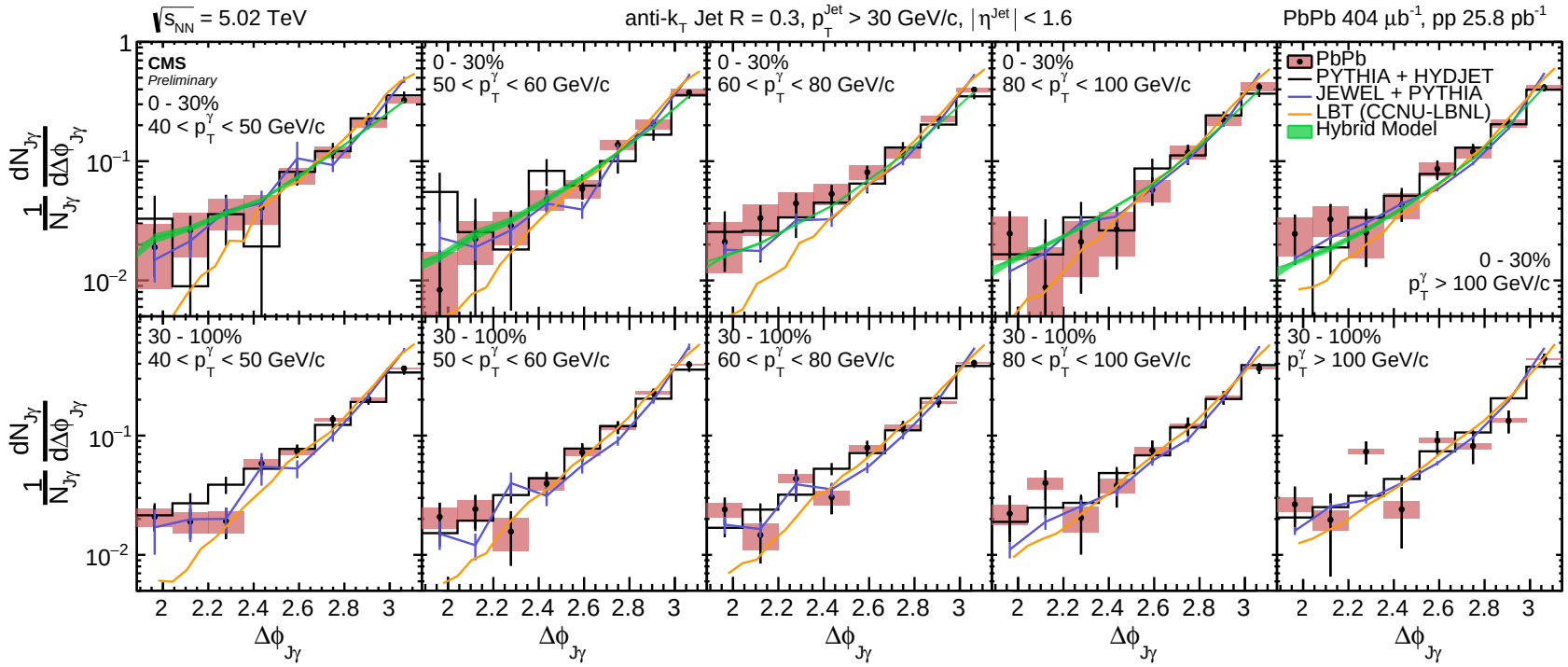

Figure 6-20: Azimuthal correlation of photons and jets in each $p_{\mathrm{T},\gamma}$ bin (from left to right) for central PbPb (top) and peripheral PbPb (bottom). The PbPb data is compared to several theoretical predictions. The correlation is shown on a logarithmic scale with the range restricted to $\Delta\phi_{J\gamma} > \frac{3\pi}{5}$

$x_{J\gamma}$

In the $x_{J\gamma}$ distributions, the Hybrid model shows exceptional agreement with the data including the trend as a function of p_{T}^{γ}. The LBT and JEWEL results lack the long tail in $x_{J\gamma}$ (just like their references) and are peaked below the data in all panels, but they both replicate the increase in integral and mean at high p_{T}^{γ}.

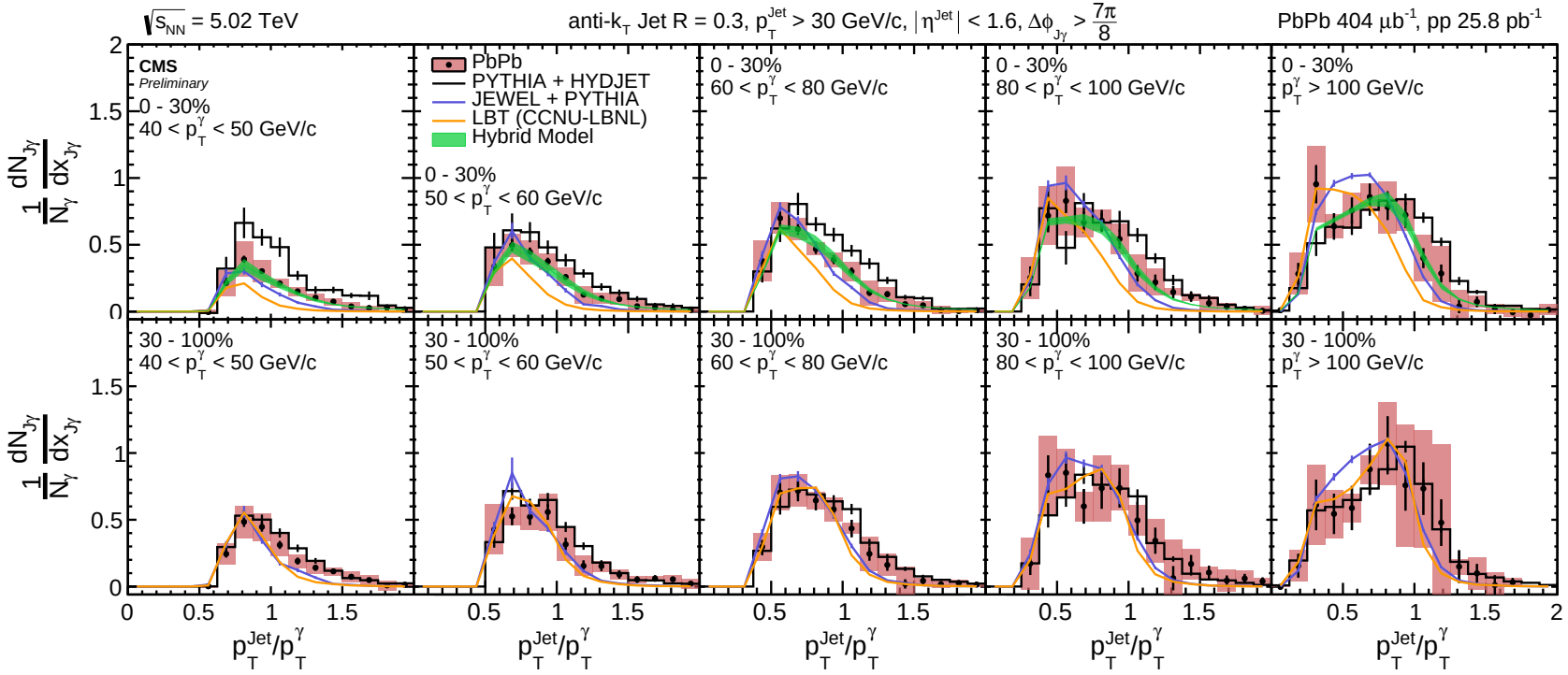

Figure 6-21: Distribution of $x_{J\gamma}$ in each $p_{\mathrm{T},\gamma}$ bin (from left to right) for central PbPb (top) and peripheral PbPb (bottom). The PbPb data is compared to several theoretical predictions.

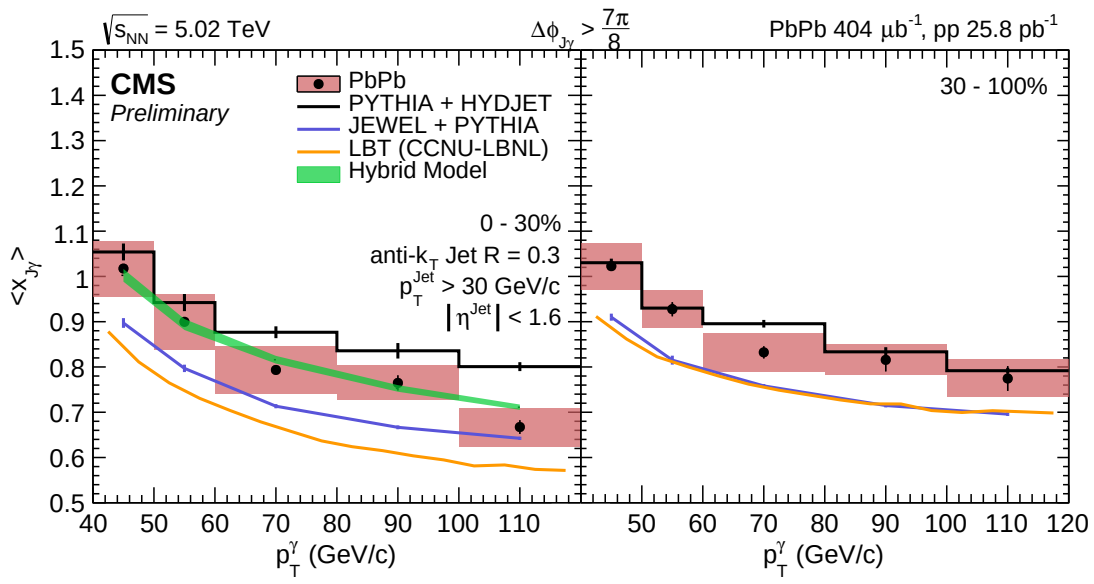

Figure 6-22: Average jet over photon transverse momentum ratio ($\langle x_{J\gamma} \rangle$) of the recoiled jets in (left) central PbPb, and (right) and peripheral PbPb. The PbPb data is compared to several theoretical predictions.

$R_{J\gamma}$

All 3 models show similar levels of agreement with the data as their references in Section 6.2.1: Hybrid and JEWEL models agree with the data at lower p_{T}^{γ}, but at the highest p_{T}^{γ} point (and all points for LBT) $R_{J\gamma}$ is under-predicted.

$\mathbf{I}_{\mathrm{AA}}$

The JEWEL and LBT results agree with the PbPb associated jet spectra about as well as their references match the pp results in Section 6.2.1. The LBT results reproduce the flattened spectra well while JEWEL resproduces the high $p_{\mathrm{T}}^{\mathrm{Jet}}$ spectra well.

In Fig. 6-25, the Hybrid model reproduces the suppression of low p_{T} jets well, while LBT and JEWEL predict more suppression, even in peripheral events. At high p_{T}^{γ}, all 3 models predict enhancement at low $p_{\mathrm{T}}^{\mathrm{Jet}}$ to varying degrees.

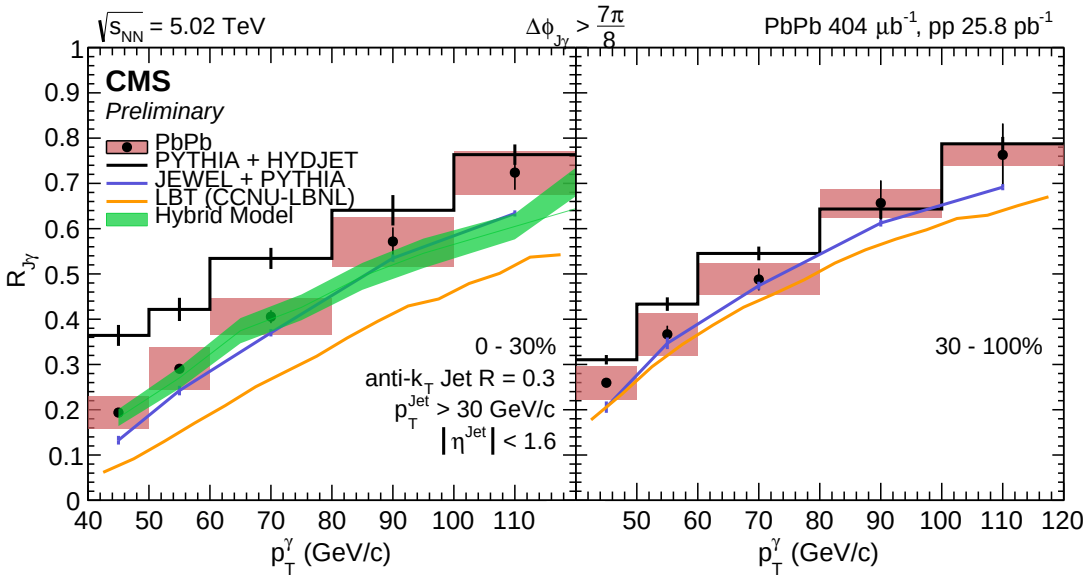

Figure 6-23: Average number of associated jets per photon ($R_{J\gamma}$) as a function of leading photon p_{T} in (left) central PbPb, and (right) and peripheral PbPb. The PbPb data is compared to several theoretical predictions.

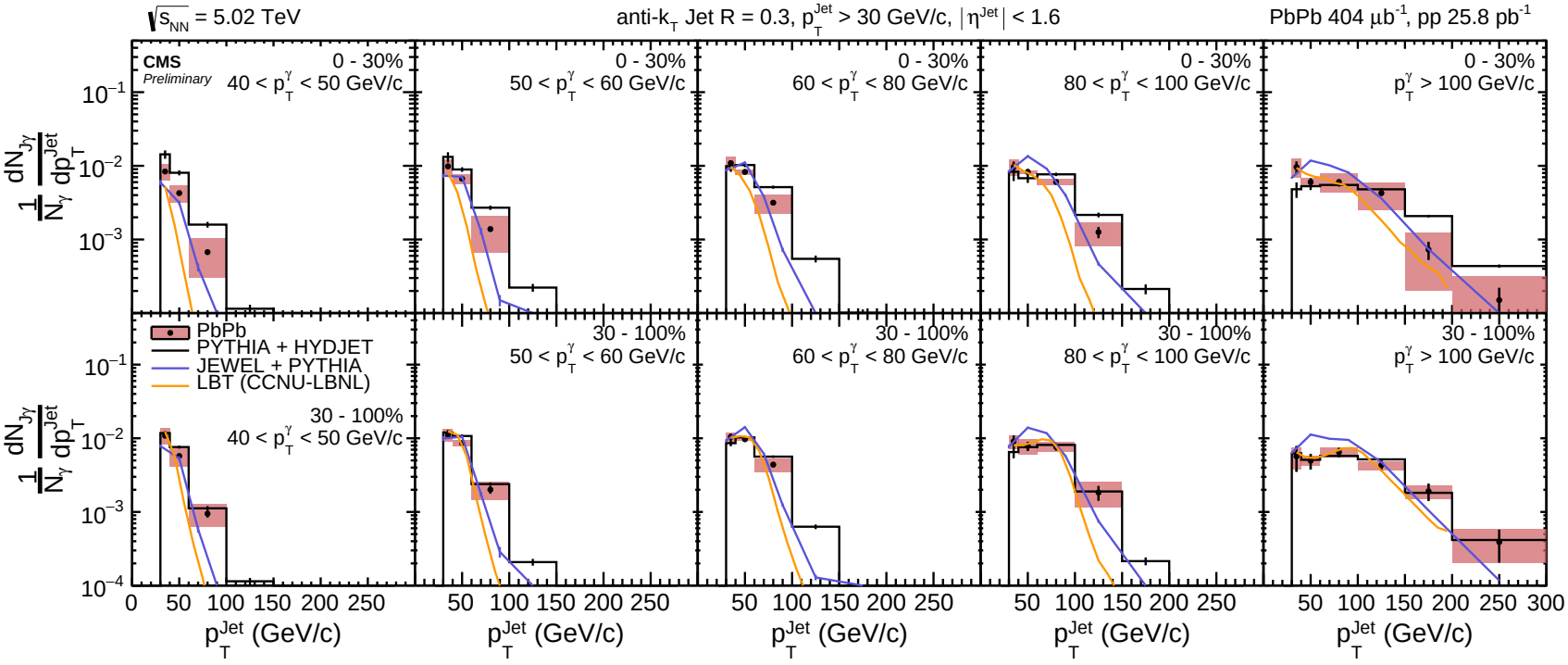

Figure 6-24: The $p_{\mathrm{T}}^{\mathrm{Jet}}$ spectra for PbPb data. The PbPb data is compared to several theoretical predictions.

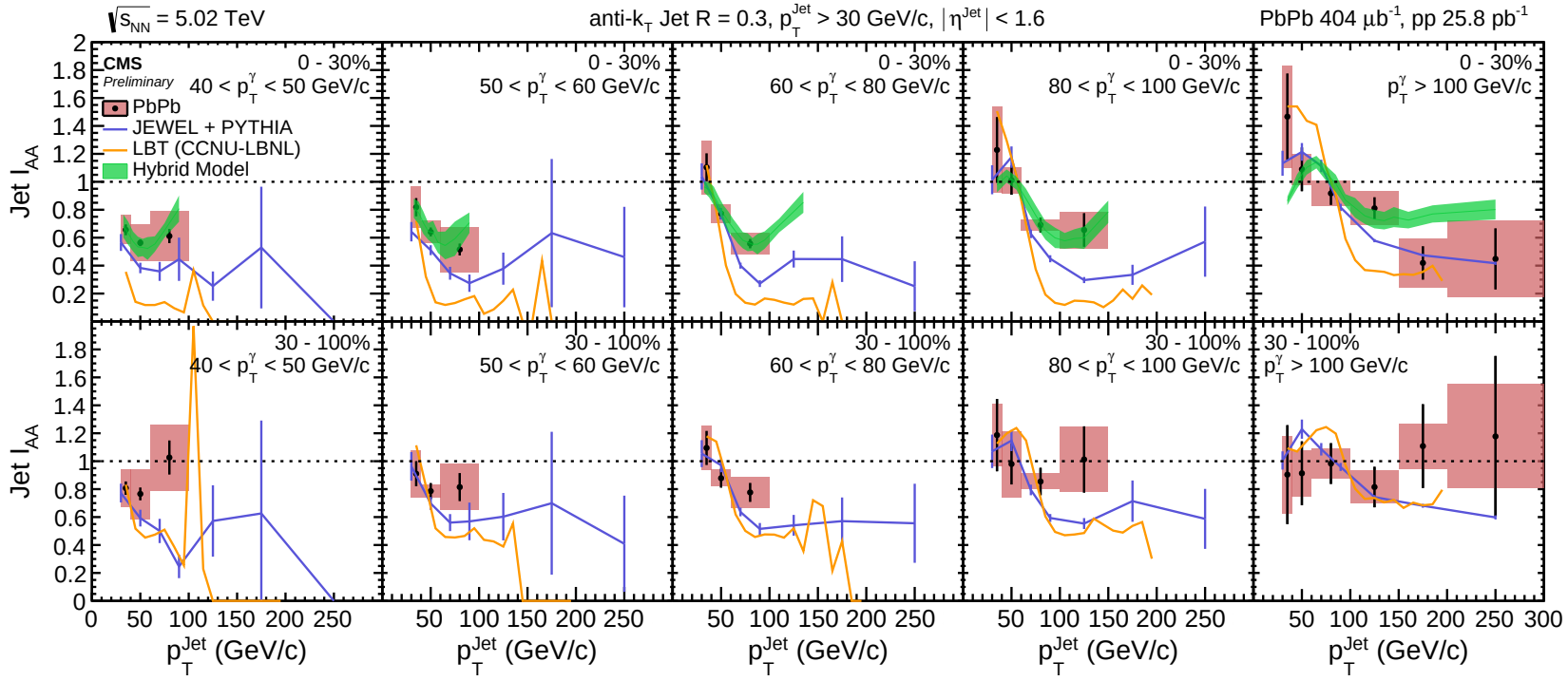

Figure 6-25: Ratio of jet yield in PbPb collisions to smeared pp. The PbPb data is compared to several theoretical predictions. The solid purple line is the prediction of the pQCD jet E-loss model with collisional energy loss, while the dashed purple line is the prediction of the same model without collisional energy loss.

Centrality Dependence

For Figures 6-26 – 6-29, the difference between the JEWEL results and the data is about the same as that for their reference in Section 6.2.1, except for $R_{J\gamma}$ where there is no crossover and instead the predicted $R_{J\gamma}$ is consistently lower than the data. The Hybrid model continues to provide remarkable agreement with the data in the $x_{J\gamma}$ distributions and $\langle x_{J\gamma} \rangle$.

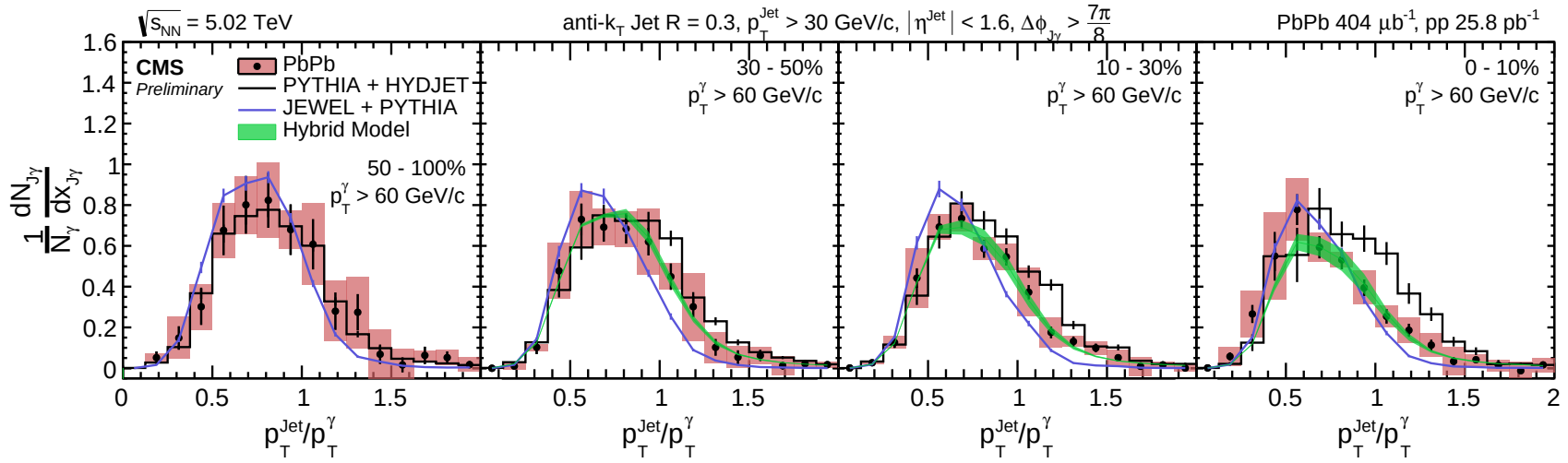

Figure 6-26: Distribution of $x_{J\gamma}$ of photon+jet pairs of PbPb collisions normalized by the number of photon+jet pairs. The PbPb data is compared to several theoretical predictions.

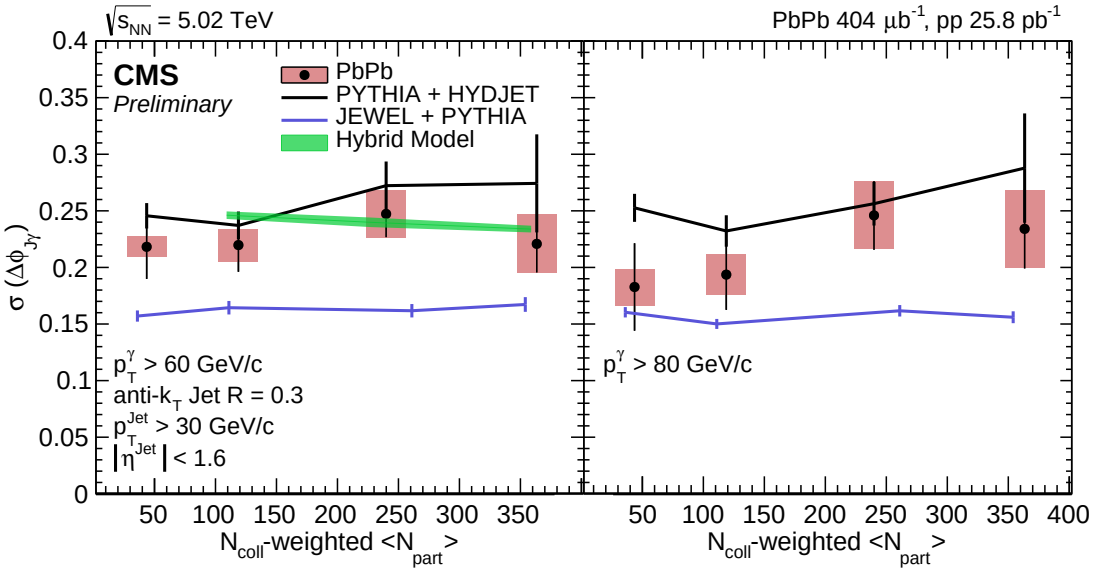

Figure 6-27: Comparison of $\Delta\phi_{J\gamma}$ width in PbPb collisions shown for different $p_{\mathrm{T}}^{\mathrm{Jet}}$ bins. The PbPb data is compared to several theoretical predictions.

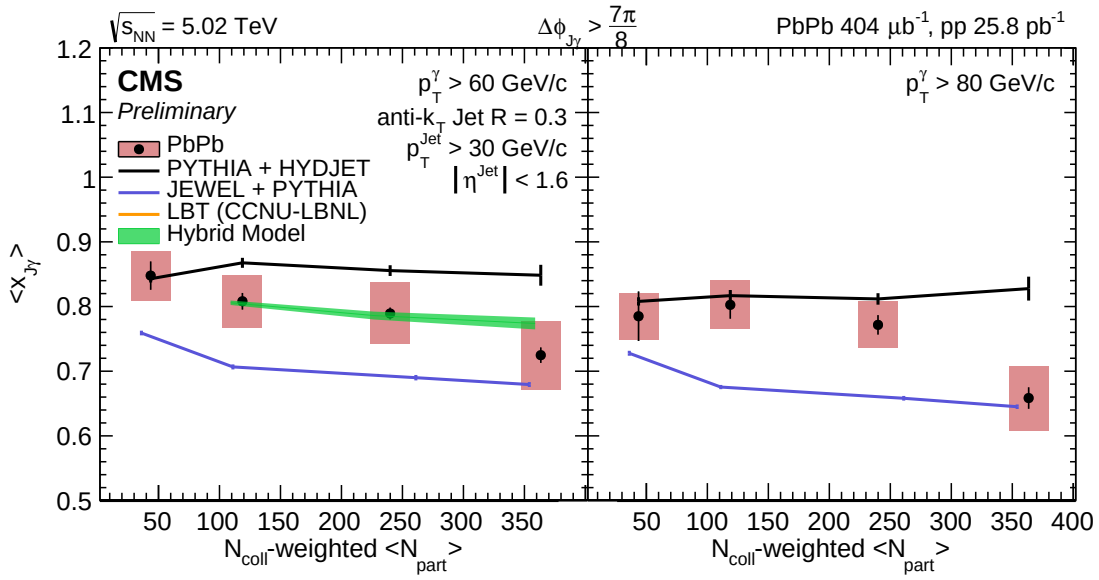

Figure 6-28: Comparison of $\langle x_{J\gamma} \rangle$ in PbPb collisions. The PbPb data is compared to several theoretical predictions.

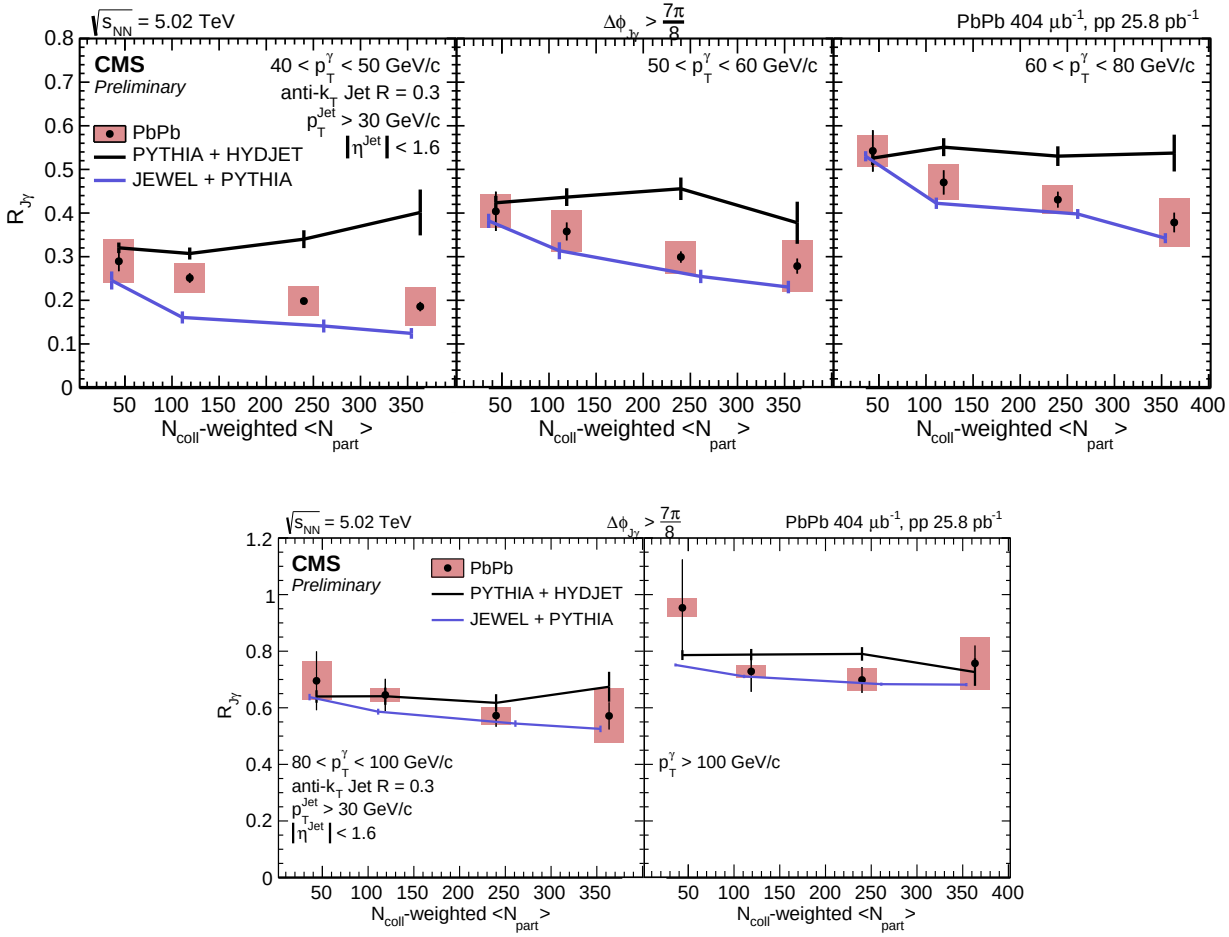

Figure 6-29: Comparison of $R_{J\gamma}$ in PbPb collisions. The PbPb data is compared to several theoretical predictions.

Chapter 7

Conclusions

The results shown in Section 6 are a huge array of differential measurements made to answer a single question: what happens to the parton as it traverses the medium? First, let us review the comparison of the PbPb results with the pp reference to see what the data itself tells us about the interaction of the probe with the medium. Afterward, let us take a close look at the theoretical predictions to see which proposed mechanisms might explain those interactions.

7.1 Listing of Experimental Findings

Figure 6-1 shows that there is no significant deflection of the parton as it passes through the medium. Figures 6-2, 6-3, and 6-4 all show that the parton loses energy, and that energy must go to wide angles, away from the jet cone (or else the jet algorithm would re-sum it back into the jet). Figures 6-7, 6-9, and 6-10 show that the amount of energy lost is greater in central collisions (and that there is perhaps no energy loss in peripheral collisions). Finally, Figure 6-6 shows directly that partons lose energy and are "moved" to lower p_{T}.

Let's take a closer look at exactly how much energy the parton loses. Looking at the left panel of Figure 6-3 and arbitrarily picking the middle point at p_{T}^{γ} of 70 GeV/c, we see that in pp collisions the average associated jet energy is 0.875×70 GeV/c = 61.25 GeV/c. In 0%–30% PbPb collisions, the average associated jet energy for the

same class of photons is 0.79×70 GeV/c = 55.3 GeV/c. This is an average energy loss of almost 6 GeV/c. We know that the lifetime of the medium can only be at maximum a few fermi/c, so this is a differential energy loss of roughly 2 GeV/c per fermi. Ignoring the mass and converting to macroscopic units this is more than 300,000 kg m /s^2, about the same amount of force produced by a single engine on a Boeing 747 aircraft[49]. For reference, the energy loss of a MIP passing through silicon is 4 MeV/cm while this is approximately 1×10^{16} MeV/cm.

7.2 Theoretical Explanations

We included comparisons to 3 different theoretical models in Section 6.2. Because perturbative calculations cannot be used in many of the regimes applicable to Heavy Ion collisions, each model includes different phenomenological adjustments to calculations in order to try to capture the non-perturbative behavior. Based on relative agreement of each model with the PbPb data, the relative importance of each of the phenomenological adjustments can be shown; the models which agree better with data may be including non-perturbative elements that are more important than those in models which do not match the data as well.

7.2.1 JEWEL model

The first model is a fully dynamical perturbative model described in references [40, 41]. In vacuum, the model reduces to PYTHIA 6. In the medium, the model assumes that the interactions of the partons during jet evolution are of sufficiently high scale that they fully resolve the quark or gluon scattering centers in the medium. Energy loss is governed by collisions with these scattering centers and approximated using perturbative $2 \rightarrow 2$ matrix elements (both elastic and inelastic) and parton showers. There are explicitly no strongly-coupled physics replicated in the model.

7.2.2 Linearized Boltzmann Transport model

The second model is a perturbative model that keeps close track of the "recoil" partons that arise out of interactions between the initial hard parton and medium, described in reference [43]. Similarly to JEWEL, partons lose energy to the medium through $2 \to 2$ scattering processes (in this case elastic only). Unlike JEWEL, the LBT model keeps track of the energy deposited into the medium. Energy lost by the initial parton is carried away by thermal partons in the medium, which can later show up as extra soft particles in the jet cone.

7.2.3 Hybrid model

The third model is a Hybrid perturbative/strongly coupled model, described in reference [45], expanded for boson-jet studies in [46] and jet angular structure in [47]. For the jet production and hard splittings, the vacuum-like perturbative DGLAP equations govern the behavior. However, between splittings each parton will lose energy to the medium. There exist holographic systems that are strongly coupled and have gravitational duals, as in Ads/CFT correspondence. The energy loss due to soft interactions with the medium is modeled using this gravitational framework of strings falling into a 5th dimensional black hole. While the strongly coupled theory in this gravitational correspondence is explicitly not QCD, it is believed that certain qualitative features, such as the functional form of the energy loss, should hold in both the strongly-coupled gravitational dual and QCD.

Specifically, the energy loss of partons follows the following equation:

$$\frac{1}{E_{in}}\frac{dE}{dx} = -\frac{4}{\pi}\frac{x^2}{x_{stop}^2}\frac{1}{\sqrt{x_{stop}^2 - x^2}} \tag{7.1}$$

where E_{in} is the initial energy of the parton, x is the distance traveled in the medium, and x_{stop} is the stopping distance of the parton:

$$x_{stop} = \frac{1}{2\kappa_{SC}}\frac{E_{in}^{1/3}}{T^{4/3}} \tag{7.2}$$

x_{stop} is the stopping distance of a parton traveling through an infinite plasma of constant temperature T, parameterized by a single free parameter κ_{SC} which is previously fit to data [45, 46] from a jet R_{AA} measurement. For the measurement presented in this thesis, the model is fully-determined without additional fitting. The model is applied in a space-and-time varying plasma as described by the iEBE-VISHNU Monte-Carlo code package [50].

The theoretical bands around the Hybrid model results come from the experimental uncertainty on the data used to fix κ_{SC}. The value as fitted for κ_{SC} corresponds to a stopping length x_{stop} which is 3 to 4 times longer than that in the strongly-coupled holographic system from which it was inspired.

7.2.4 Conclusions of Theoretical Comparisons

Based on Section 6.2, we see that none of the theoretical models fails completely at describing the data. However, the LBT has issues matching the reference observables which limits our ability to draw conclusions about the efficacy of the LBT model at describing physics in PbPb collisions. The JEWEL model replicates the trends seen in the PbPb data, but also has issues matching the references in some observables. The Hybrid model really shines, matching the reference in most observables (so that we can make strong statements about its efficacy in PbPb collisions) but also matching the actual PbPb observables as well. We take this as a strong indication that strongly-coupled physics is an important facet of the energy loss of hard partons through the medium and perturbative-only approaches may not be able to precisely match the experimental results. Moving forward, we highly recommend that all theory groups spend the effort to guarantee that the reference observables are matched well so that stronger conclusions based on the PbPb collisions can be made.

7.3 Summary

We have used photon+jet events in heavy ion collisions at the LHC recorded by the CMS detector to study the phenomenology of QCD. Using the photon as an unam-

biguous measurement of the initial parton and the reconstructed jet a measurement of the final parton, we have shown that compared to pp collisions the color-charged parton loses a significant amount of energy without being deflected in PbPb collisions. By comparing the amount of energy lost and deflection expected in several theoretical models we show that the energy loss is well-described by the Hybrid framework where energy loss is governed by strongly-coupled, non-perturbative interactions with a medium of strongly-interacting color charges.

It should be possible in the future to look at changes in the substructure of the jets, such as their fragmentation function, as they pass through the medium. Theoretical models such as LBT which track the medium excitations may reproduce experimental results better for those observables. We hope that the theory community continues to collaborate and communicate about reference choices and implementation of necessary functions such as medium excitation tracking so that a more comprehensive study of the importance of different phenomenology can be conducted.

The dominant uncertainties in these results are no longer statistical but systematic in nature, specifically in the energy scale and resolution of the reconstructed jets. We observe recent advances in jet background subtraction, both from theorists and from experimentalists, with much optimism.

The results shown here are an accomplishment many years in the making. They are an early foray into highly differentiable, unambiguous measurements of hard probes for the heavy ion community and herald a movement toward precision physics in that community.

Appendix A

Tables

List of Tables

Appendix B

Figures

List of Figures

Bibliography

[1] Study of Isolated-Photon + Jet Correlations in PbPb and pp Collisions at $\sqrt{s_{NN}} = 5.02$ TeV. Technical Report CMS-PAS-HIN-16-002, CERN, Geneva, 2016.

[2] *CMS Physics: Technical Design Report Volume 1: Detector Performance and Software*. Technical Design Report CMS. CERN, Geneva, 2006. `https://cds.cern.ch/record/922757`.

[3] The CMS Collaboration. Cms physics technical design report, volume ii: Physics performance. *Journal of Physics G: Nuclear and Particle Physics*, 34(6):995, 2007. `http://stacks.iop.org/0954-3899/34/i=6/a=S01`.

[4] Gamma-jet correlations in pbpb and pp collisions at center of mass energy 5.02tev. *CMS Analysis Note*, AN-16-054, 2016.

[5] Kenneth G. Wilson. Confinement of quarks. *Phys. Rev. D*, 10:2445–2459, Oct 1974.

[6] David J. Gross and Frank Wilczek. Ultraviolet behavior of non-abelian gauge theories. *Phys. Rev. Lett.*, 30:1343–1346, Jun 1973.

[7] H. David Politzer. Reliable perturbative results for strong interactions? *Phys. Rev. Lett.*, 30:1346–1349, Jun 1973.

[8] R. P. Feynman. Mathematical formulation of the quantum theory of electromagnetic interaction. *Phys. Rev.*, 80:440–457, Nov 1950.

[9] F. J. Dyson. The radiation theories of tomonaga, schwinger, and feynman. *Phys. Rev.*, 75:486–502, Feb 1949.

[10] Westfälische Wilhelms universität Münster. Lattice calculations at non-zero chemical potential: The qcd phase diagram owe philipsen, 2008.

[11] Marco Panero, Kari Rummukainen, and Andreas Schäfer. Lattice study of the jet quenching parameter. *Phys. Rev. Lett.*, 112:162001, Apr 2014.

[12] E. V. Shuryak. What rhic experiments and theory tell us about properties of quark-gluon plasma ? 2004. Nucl.Phys. A750 (2005) 64-83.

[13] Matteo Cacciari, Gavin P. Salam, and Gregory Soyez. Fastjet user manual. *The European Physical Journal C*, 72(3):1–54, 2012.

[14] STAR Collaboration. Elliptic flow in $au+au$ collisions at $\sqrt{s_{\rm nn}} = 130$GeV. *Phys. Rev. Lett.*, 86:402–407, Jan 2001.

[15] PHOBOS Collaboration. Charged-particle multiplicity near midrapidity in central $au+au$ collisions at $\sqrt{s_{NN}} = 56$ and 130GeV. *Phys. Rev. Lett.*, 85:3100–3104, Oct 2000.

[16] A. H. Mueller and J. Qiu. *Nucl. Phys. B*, 268:427, 1986.

[17] Adare et. al. Photon-hadron jet correlations in $p + p$ and Au + Au collisions at $\sqrt{s_{NN}} = 200$ gev. *Phys. Rev. C*, 80:024908, Aug 2009.

[18] STAR Collaboration. Di-jet imbalance measurements at $\sqrt{s_{NN}} = 200$ gev at star, 2016.

[19] STAR Collaboration. Jet-hadron correlations in $\sqrt{s_{\rm NN}} = 200$ GeV $p + p$ and central Au + Au collisions. *Phys. Rev. Lett.*, 112:122301, Mar 2014.

[20] Grazyna Odyniec. Rhic beam energy scan program—experimental approach to the qcd phase diagram. *Journal of Physics G: Nuclear and Particle Physics*, 37(9):094028, 2010.

[21] Introducing...sphenix! `https://www.bnl.gov/newsroom/news.php?a=26258`. Accessed: 2016-10-31.

[22] ATLAS Collaboration. Observation of a centrality-dependent dijet asymmetry in lead-lead collisions at $\sqrt{s_{\rm NN}} = 2.76$ TeV with the atlas detector at the lhc. *Phys. Rev. Lett.*, 105:252303, Dec 2010.

[23] CMS Collaboration. Observation and studies of jet quenching in pbpb collisions at $\sqrt{s_{NN}} = 2.76$ tev. *Phys. Rev. C*, 84:024906, Aug 2011.

[24] Matteo Cacciari, Gavin P. Salam, and Sebastian Sapeta. On the characterisation of the underlying event. *Journal of High Energy Physics*, 2010(4):65, 2010.

[25] CMS Collaboration. Isolated photon production in 2.76 tev pbpb collisions as a function of transverse momentum and reaction centrality. *CMS Publication Draft*, (CMS-PAS-HIN-11-002), 2011.

[26] CMS Collaboration. Studies of jet quenching using isolated-photon + jet correlations in pbpb and pp collisions at. *Physics Letters B*, 718(3):773 – 794, 2013.

[27] Study of Isolated photon jet correlation in PbPb and pp collisions at 2.76TeV and pPb collisions at 5.02TeV. Technical Report CMS-PAS-HIN-13-006, CERN, Geneva, 2013.

[28] CMS Collaboration. Measurement of inclusive jet production and nuclear modifications in ppb collisions at sqrt(s)=5.02 tev. *The European Physical Journal C*, 76(7):372, 2016.

[29] CMS Collaboration. Nuclear effects on the transverse momentum spectra of charged particles in ppb collisions at sqrt(s)=5.02tev. *The European Physical Journal C*, 75(5):237, 2015.

[30] A Tapper and Darin Acosta. CMS Technical Design Report for the Level-1 Trigger Upgrade. Technical Report CERN-LHCC-2013-011. CMS-TDR-12, Jun 2013. `http://cds.cern.ch/record/1556311`.

[31] Isolated photon–jet momentum imbalance in pbpb collisions at $\sqrt{s_{NN}} = 2.76$ TeV. *CMS Analysis Note*, AN-11-435, 2011.

[32] Matteo Cacciari, Gavin P. Salam, and Gregory Soyez. The Catchment Area of Jets. *JHEP*, 0804:005, 2008.

[33] Olga Kodolova, I. Vardanian, A. Nikitenko, and A. Oulianov. The performance of the jet identification and reconstruction in heavy ions collisions with CMS detector. *Eur. Phys. J.*, C50:117, 2007.

[34] Particle-flow event reconstruction in cms and performance for jets, taus, and met. *CMS PAS*, PFT-09-001, 2009.

[35] CMS Collaboration. Commissioning of the particle-flow reconstruction in minimum-bias and jet events from pp pp collisions at 7 TeV. *CMS Physics Analysis Summary*, http://cdsweb.cern.ch/record/1279341, 2010.

[36] Measurement of the relative jet energy scale in cms with pp collisions at sqrt(s) = 7 tev. *CMS Analysis Note*, AN2010-139, 2010.

[37] CMS Collaboration. Determination of the jet energy scale in CMS with pp collisions at $\sqrt{s} = 7$ TeV. *CMS Physics Analysis Summary*, http://cdsweb.cern.ch/record/1308178, 2010.

[38] Torbjörn Sjöstrand, Stephen Mrenna, and Peter Z. Skands. A brief introduction to PYTHIA 8.1. *Comput. Phys. Commun.*, 178:852, 2008.

[39] Peter Skands, Stefano Carrazza, and Juan Rojo. Tuning PYTHIA 8.1: the Monash 2013 Tune. *Eur. Phys. J. C*, 74(8):3024, 2014.

[40] Korinna Zapp. Jewel 2.0.0: directions for use. *The European Physical Journal C*, 74(2):2762, 2014.

[41] Raghav Kunnawalkam Elayavalli and Korinna Christine Zapp. Simulating v+jet processes in heavy ion collisions with jewel. 2016. arXiv:1608.03099.

[42] Raghav Kunnawalkam Elayavalli. Personal Correspondence, 2016.

[43] Xin-Nian Wang and Yan Zhu. Medium modification of γ jets in high-energy heavy-ion collisions. *Phys. Rev. Lett.*, 111:062301, Aug 2013.

[44] Tan Luo. Personal Correspondence, 2016.

[45] Jorge Casalderrey-Solana, Doga Can Gulhan, José Guilherme Milhano, Daniel Pablos, and Krishna Rajagopal. A hybrid strong/weak coupling approach to jet quenching. *Journal of High Energy Physics*, 2014(10):19, 2014.

[46] Jorge Casalderrey-Solana, Doga Can Gulhan, José Guilherme Milhano, Daniel Pablos, and Krishna Rajagopal. Predictions for boson-jet observables and fragmentation function ratios from a hybrid strong/weak coupling model for jet quenching. *Journal of High Energy Physics*, 2016(3):53, 2016.

[47] Jorge Casalderrey-Solana, Doga Gulhan, Guilherme Milhano, Daniel Pablos, and Krishna Rajagopal. Angular structure of jet quenching within a hybrid strong/weak coupling model, 2016.

[48] Daniel Pablos. Personal Correspondence, 2016.

[49] `http://www.wolframalpha.com/input/?i=2+GeV+\%2F+fm`. Wolfram alpha. Visited 2016-09-28.

[50] Chun Shen, Zhi Qiu, Huichao Song, Jonah Bernhard, Steffen Bass, and Ulrich Heinz. The iebe-vishnu code package for relativistic heavy-ion collisions, 2014.